ABSTRACT

J/Ψ Production in $d+$ Au Collisions at $\sqrt{s_{NN}} = 200$ GeV at the STAR Experiment

Christopher Powell
University of Cape Town
January 2010

The production of J/ψ and other quarkonia is of particular interest in relativistic heavy ion collisions, as their yields are supposed to be suppressed in the presence of the hypothesised hot, dense quark gluon plasma. However, there are other in-medium effects which will also affect the production of J/ψ (e.g., nuclear absorption, shadowing). To understand the suppression and enhancement of heavy quarkonia in A+A collisions, we must first understand how yields are modified by a nuclear medium where no hot matter is present. Light systems such as p+A and d+A are particularly interesting as there are only cold nuclear matter effects present.

We present the analysis of J/ψ production in $d+$ Au at $\sqrt{s_{NN}} = 200$ GeV (run taken in 2008) with the STAR detector. The J/Ψ yield has been studied via the di-electron decay channel, J/Ψ $\rightarrow e^+e^-$, by selecting electrons with $|\eta^e| < 1$ and ${p_T}^e > 1$ GeV/c. The analysis covers the J/Ψ kinematic region of $|y^{\mathrm{J}/\Psi}| < 1$ and ${p_T}^{\mathrm{J}/\Psi} < 5$ GeV/c. For 0%–20% central collisions, we find an average number of binary collisions in $d+$ Au collisions is $\langle N_{\mathrm{coll}} \rangle = 14.6 \pm 1.7$. The yield from central collisions has been compared to the yield in p+p collisions, and the nuclear modification factor has been determined as $R^{\mathrm{J}/\Psi}_{d+\mathrm{Au}} = 1.03 \pm 0.28 \pm 0.36$, which is consistent with unity, indicating that the J/Ψ yield in $d+$ Au collisions scales with the number of binary collisions in this particular centrality bin.

J/Ψ Production in $d+$Au Collisions at $\sqrt{s_{NN}} = 200$ GeV at the STAR Experiment

Thesis presented for the Degree of
Master of Science
in the Department of Physics
Faculty of Science
University of Cape Town

By
Christopher Powell

Supervisor: Prof. J. Cleymans

January 2010

Contents

Chapter 1

Introduction

The aim of heavy ion experiments is to understand the basic constituents of matter that make up our observable universe. Due to the nature of interactions between partons, we require extremely high energies and densities to compress the nuclear matter and free the nuclear constituents.

1.1 QCD

The theory governing strong interactions, Quantum Chromodynamics (QCD) [1], is a non-Abelian gauge theory which is described by the Standard Model [2]. The Standard Model predicts 3 elementary particle types: leptons, quarks and gauge bosons. The gauge bosons mediate the interactions between elementary particles and couple to the intrinsic charge of each interaction. There are four fundamental interactions: gravitational, weak, electromagnetic and strong interactions, listed in increasing strength of the interaction, and only the latter three are described by the Standard Model. Currently, there is no quantum theory for the gravitational interaction, nor has the force mediator of the interaction been discovered.

The lepton family consists of six fermions (spin-half particles) which are divided

into three groups separated by mass. The 1^{st} group is the electron, e^-, and the electron neutrino, ν_e, the second is the muon, μ^-, and the muon neutrino, ν_μ, and the third is the tauon, τ^-, and the tauon neutrino, ν_τ, and for each lepton there exists an anti-lepton. The leptons interact through the weak interaction via the massive Z^0 and $W^{+/-}$ bosons, and through the electromagnetic interaction via the massless photon, γ. These two theories have been combined into the electroweak theory.

Constituent to all nuclear matter are quarks, which are also broken up into 6 different flavours: up, u, down, d, charm, c, strange, s, top, t, and bottom, b. These particles are fermions, but do not have integer charge like the leptons. The positively charged quarks, u, c, and t, have charge $+\frac{2}{3}q$, while the d, s, and b quarks have charge $-\frac{1}{3}q$. These 6 quarks are also split into 3 groups of increasing mass, the first group are the lightest quarks, u and d, the second group are the c and s quarks, and the third group being the heaviest quarks, t and b, and for each quark there exists an anti-quark with opposite sign charge. Information about the members of the lepton, quark and boson families are summarized in Fig. 1.1. The main difference between leptons and quarks is that quarks carry another type of charge called colour charge. As a result, quarks can participate in the strong interaction, which is mediated by the gluon gauge boson, g. Another difference between the strong interaction and the electroweak interaction is that gluons possess colour-charge, and so they can interact with themselves. It is the strong interaction, which is the dominant force on a nuclear scale, which binds the quarks into their observable, colour-neutral states, known as hadrons, and the most abundant in nature being neutrons and protons.

1.1.1 The Strong Interaction and Asymptotic Freedom

The strong interaction describes the interaction of quarks and gluons on the scale of ≈ 1 GeV. The potential describing the strong force between quarks is

$$V(r) = -\frac{4\alpha_s}{3r} + kr, \tag{1.1}$$

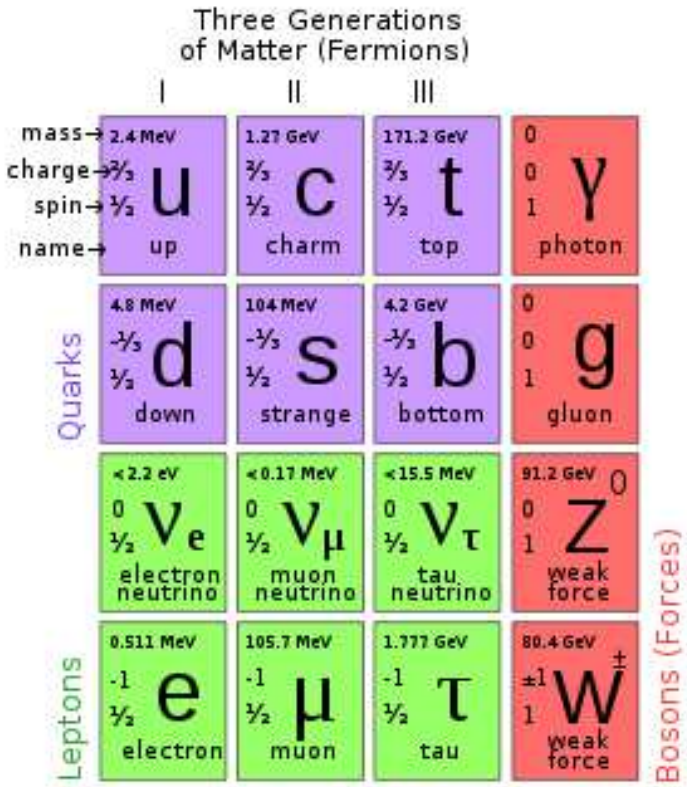

Figure 1.1: Elementary Particles in the Standard Model of Particle Physics.

where α_s is the coupling constant, r is the distance between the quarks, and k is the string constant, $k \approx 850$ MeV fm^{-1} [3]. At small distances, the Coulomb part of the potential dominates, while at large distances, the linear term is dominant. As a result, the binding force between quarks becomes stronger at larger distances. Once the field strength increases above a certain threshold, quark–anti-quark pairs are created. These bind with the quarks being separated, and as a result, free quarks are not observed in isolation.

The QCD coupling constant, α_s, has a momentum transfer dependence, which is

given, to lowest order, as

$$\alpha_s(Q) = \frac{1}{\beta_0 \ln(Q^2/\Lambda^2_{QCD})}, \tag{1.2}$$

where the QCD scale $\Lambda_{QCD} \approx 200$MeV [4], Q is the momentum transfer, and β_0 is a positive-definite coefficient. Because of this dependence on Q^2, α_s is referred to as the running coupling constant. For hard interactions, where momentum transfer is large ($Q^2 >> \Lambda_{QCD}$), $\alpha_s \to \infty$. For such processes, where r is small, the potential in Eq. (1.1) will tend to zero. In this limit, the force between quarks becomes less and less significant and quarks and gluons behave as though they were free, known as Asymptotic Freedom [5]. This allows perturbative methods of QCD (pQCD) [6] to be used in calculating QCD observables. Outside of the perturbative regime, lattice QCD (lQCD) is used to calculate properties of the hadronic matter. This method uses finite space-time lattice points on a grid to numerically compute thermodynamic properties [7, 8].

A consequence of asymptotic freedom is the ability of quarks and gluons to move over distances larger the size of a nucleon (≈ 1 fm), known as deconfinement. In this deconfined state, quarks and gluons are no longer bound inside the nucleus, and are able to propagate freely. It is believed that deconfinement can be achieved at high energy densities [9], where the strong force between bound quarks and gluons is screened due to the presence of other quarks and gluons, known as Debye screening [10]. Deconfinement occurs when the screened radius of the bound quarks and gluons, r_D, becomes smaller than the nucleon radius. A predicted result of deconfinement is the transition from hadronic matter to a phase of free quarks and gluons, known as Quark Gluon Plasma (QGP) [11, 12, 13, 14]. This hypothesized form of matter was postulated to make up the early universe microseconds after the big bang [15]. Details regarding the QCD phase diagram and QGP are discussed below.

1.1.2 QCD Phase Diagram

The QCD phase diagram contains information about the states of nuclear matter and phase transitions between these states. The QCD phase diagram is presented in $T-\mu_B$ space, where T is the temperature and μ_B is the chemical potential of the system, analogous to the pressure. Calculations from lQCD [16, 17] predict that for $\mu_B = 0$, a smooth cross-over from a hadron gas to a QGP with partonic degrees of freedom occurs at a critical temperature of $T_c \approx 170$MeV [18]. A critical point [19] is expected in the QCD phase diagram at non-zero μ_B [20, 21], where the QGP phase transition is 2$^{\text{nd}}$ order [22]. The location of the critical point, determined from extrapolating lQCD calculations to non-zero μ_B, is predicted at $150 < \mu_B < 600$ MeV [20, 22]. For larger values of μ_B, the transition from nuclear matter to QGP is expected to be 1$^{\text{st}}$ order, extending to some finite μ_B at $T = 0$ [22]. This is illustrated in Fig. 1.2. At collision energies of $\sqrt{s_{NN}} = 200$ GeV, the Relativistic Heavy Ion Collider (RHIC) probes the region on the QCD phase diagram with large T and near-zero μ_B [23, 24].

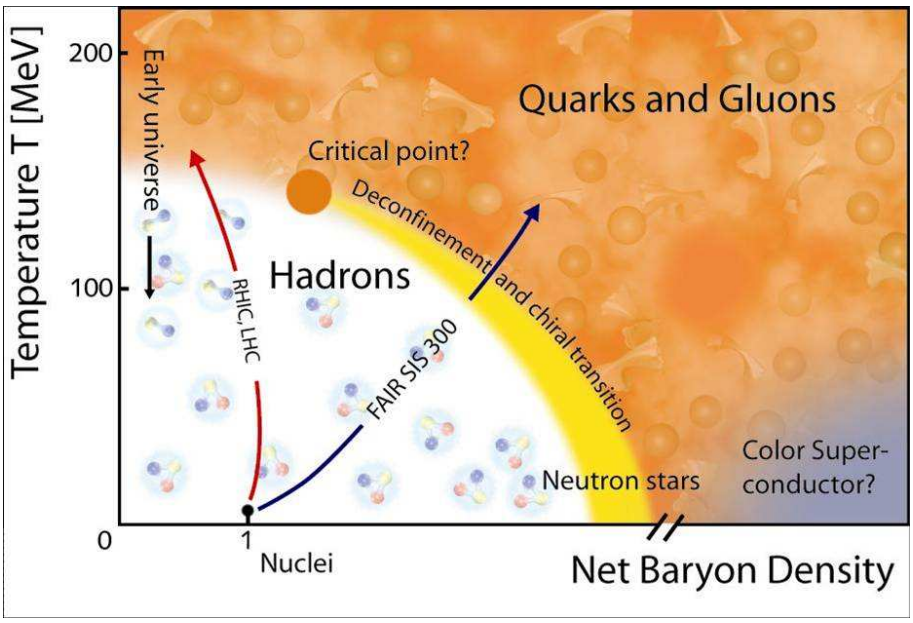

Figure 1.2: The QCD Phase Diagram [25].

1.2 Quark Gluon Plasma Signatures

In order to verify the existence and understand the properties of the QGP, experimentally observable signatures need to be identified. As the high energy density system needed to create QGP expands and cools, the force between quarks and gluons becomes more significant. As a result, quarks and gluons begin to form hadrons through inelastic (low momentum transfer) collisions. This process, known as hadronization, occurs before particles can be experimentally detected in heavy ion collisions. In order to understand the QGP, we must infer its characteristics based on the analysis of hadrons created in the QGP.

The aim of heavy ion collisions is to provide conditions in which the formation of a QGP is possible. It is necessary to understand the evolution of the dense collision system so that final state observables can be used to understand the early stages of the collision. Figure 1.3 depicts the space-time evolution of a heavy ion collision:

(a) The initial hard, partonic interactions in which products from high momentum transfer processes are formed, such as charm quarks and high p_T jets.

(b) The interaction of particles created in the hot collision system. This is when QGP formation may take place, after which temperatures begin to decrease as the system expands and thermalises. Charmonium formation from produced $c\bar{c}$ pairs also occurs in this stage.

(c) The hadronization of particles as the temperature drops below T_c. First, chemical freeze-out is reached at temperatures around 170 MeV [26], after which the ratio of particle species remains constant. Kinetic freeze-out is reached for temperatures around 120 MeV [27], after which inelastic collisions cease.

Since hadronization sets in before particles can be detected, the search for QGP relies on indirect methods of experimentally exploring the early collision system. These

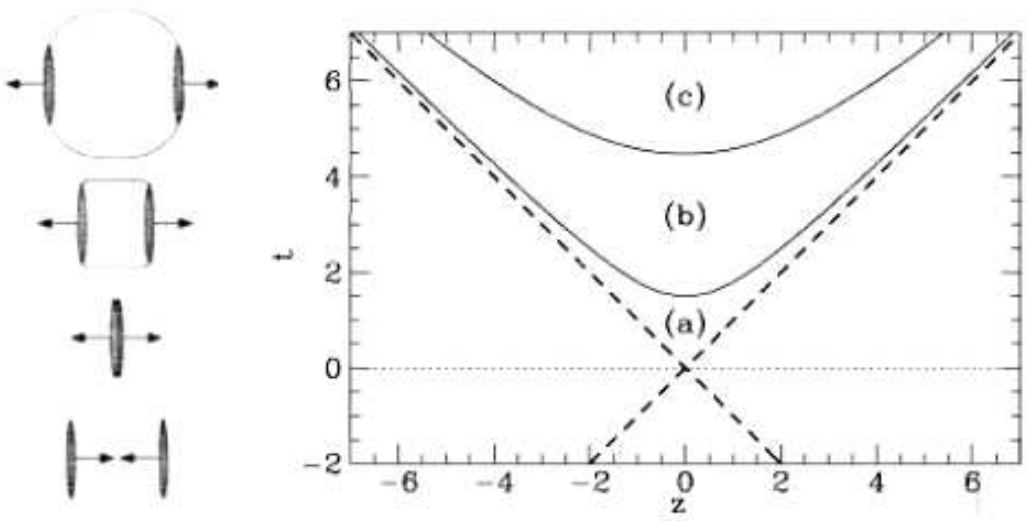

Figure 1.3: The space-time evolution of a relativistic heavy ion collision. The phases are (a) initial collision, (b) thermalized QGP, and (c) hadronization. The beam axis is denoted by z. Figure taken from [39].

techniques rely on identifying signatures of the QGP which we can measure after hadronization through various experimental observables in heavy ion collisions. Such observables are introduced in Section 1.3.

There are various predicted signatures of QGP which provide information about different aspects of the deconfined matter. We discuss several examples below.

The threshold for producing $s\bar{s}$ pairs is significantly lower in a hadron gas scenario than in the presence of a QGP. Since strange quarks are produced mainly by gluon fusion, and gluons are abundant in the plasma, the enhancement of strangeness production provides a signature of QGP formation [28, 29].

Jet quenching is also used as a signature of the formation of QGP. This refers to the phenomena of high momentum partons undergoing energy loss in the dense

medium [30]. Similar to electromagnetic energy loss of charged particles in matter, partons radiate energy as they propogate through the QGP matter. It is expected that the energy loss of partons in the QGP is larger than that in hadronic matter [31], resulting in a high p_T suppression. This suppression has been observed at RHIC for high p_T particles ($p_T > 4$ GeV/c) [32, 33].

Hard probes created in the initial stage of the collision provide information about the early times of the collision system. Heavy quarks are of particular interest as the screening of their potential at high temperatures makes them susceptible to the presence of a hot medium. Charmonium suppression is used as a signature for the existence of QGP, where $c\bar{c}$ pairs are separated due to Debye screening in the medium [10]. The excited states of $c\bar{c}$ (ψ', χ_c) have larger radii and lower binding energy [34], and so dissociate at a lower temperature than J/Ψ, providing an effective thermometer of the collision system. This is also true for bottomonium, however higher energies and densities are required to melt the $b\bar{b}$ states. The di-lepton decay channel of J/Ψ is used to understand J/Ψ production, since leptons are unaffected by the medium. The branching ratio for J/$\Psi \rightarrow e^+e^-(\mu^+\mu^-)$ decay channel is 5.94% (5.93%) [34]. While roughly 60% of J/Ψs are directly produced as a $1S$ charmonium state, the remaining 40% of come from feed down of the excited charmonium states, 30% from χ_c and 10% from ψ' [35].

This analysis will focus on J/Ψ suppression as a signature for the existence of the QGP. Details on this are presented in Chapter 2.

1.3 Heavy Ion Collisions

As heavy ions collide together, the partons in the overlapping region of the colliding nuclei undergo inelastic collisions, transferring kinetic energy into matter and transverse energy. The amount of transverse energy created in the collision is estimated

by the Bjorken energy density, ϵ_{Bj} [36]:

$$\epsilon_{Bj} = \frac{1}{\pi R^2} \frac{1}{\tau_0} \frac{\mathrm{d}E_T}{\mathrm{d}y}, \tag{1.3}$$

where R is the radius of the overlapping nuclei region, τ_0 is the thermalisation time (typically a value of $\tau_0 \sim 1$ fm/c is used), E_T is the transverse energy (experimentally measured using calorimetry, jet quenching, etc.), and y is the rapidity. For head-on Au+Au collisions at $\sqrt{s_{NN}} = 200$ GeV, the Bjorken energy density is estimated to be $\epsilon_{Bj} \approx 4 - 5$ GeV/fm^3 [37], and this value is very sensitive to the parameters chosen for the collision geometry in Eq. (1.3). The rapid expansion of the collision system creates a hot volume often referred to as the fireball, in which QGP may be formed if temperatures are sufficient [36, 38]. The further expansion and cooling of the system leads to hadronization and finally kinetic freeze-out, after which particles no longer interact. Observables in heavy ion collision experiments, such as particle multiplicities and momentum spectra, provide information of the system after kinetic freeze-out. These final-state distributions are related to the early collision system, and are used to understand the evolution of the system.

In this section, experimental observables of heavy ion collisions are presented. The relevant kinematic variables necessary for understanding the properties of the fireball will be introduced. Finally, we will show how these properties can be used to determine the effects of the dense system on particle production.

1.3.1 Particle Multiplicity

The number of particles produced in heavy ion collisions increases with the amount overlap of nuclear matter in the collision, known as centrality. This is defined by the impact parameter b, which describes the distance between the nuclei centres perpendicular to the beam, shown in Fig. 1.4. In red are the nucleons which participate in the collision, N_{part}, and in blue are the spectator nucleons which do not participate in the interaction. A central collision has a small impact parameter, whereas a large impact parameter indicates a peripheral collisions. As N_{part} increases, the number

of elementary nucleon-nucleon collisions, N_{coll}, increases as ${N_{\text{part}}}^{4/3}$[40]. Both the increase in soft processes with N_{part} and of hard processes with N_{coll} contribute to particle production [41, 42].

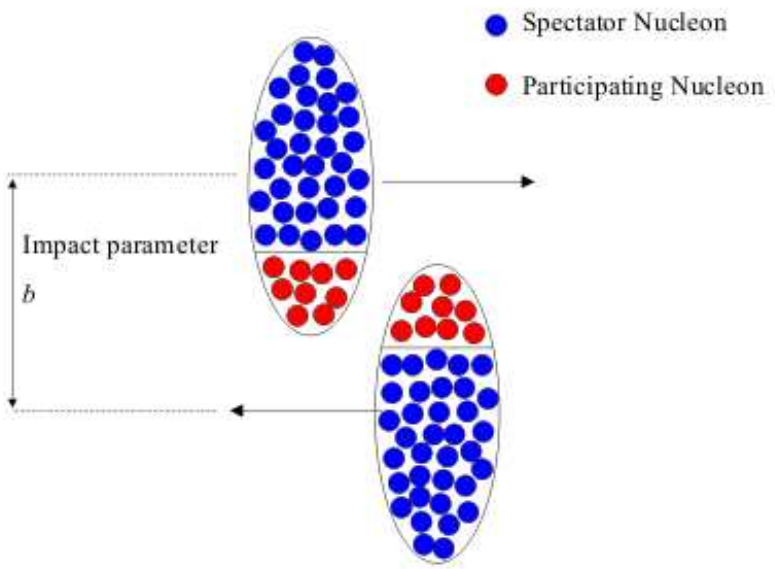

Figure 1.4: A schematic diagram of colliding nuclei, indicating the impact parameter b, and the overlap region of the nuclei in red. Diagram taken from [47].

Since the impact parameter and the number of participant nucleons cannot be measured directly, the observed particle multiplicity is used as an indirect measure of centrality. Glauber calculations [40, 43] are used to map the observed charged particle multiplicity to the collision geometry of the nuclei. This is done by modelling the nucleon-nucleon collisions between the participant nucleons with a given nuclei collision geometry. The distribution of nucleons within a nuclei is described by a Woods-Saxon distribution [44], where nuclei are assumed to be spherical, and protons and neutrons are assumed to have identical distributions. The Woods-Saxon density decreases exponentially in the radial direction, without a discrete edge/boundary to

the density profile. It is important to note that there are different implementations of Glauber calculations, with two general classes: optical and Monte Carlo. While the optical Glauber calculations [45] aim to derive analytic formulae to relate particle multiplicity with collision geometry, the Monte Carlo method [46] simulates collisions of nuclei with a given transverse separation b, a random value obtained from a uniform distribution. Nucleons are randomly distributed within the nuclei according to the Woods-Saxon distribution. The Monte Carlo Glauber method is implemented in this analysis, and nucleons are considered to interact based on their separation and the inelastic nucleon-nucleon cross section, $\sigma_{\text{inel}} = 42$ mb.

The centrality classes are determined by dividing the multiplicity distribution into bins of 0% - 20% central, 20% - 40% central, etc., where for example the most central bin, 0% - 20%, contains the 20% of events with small b and the highest track multiplicities on average. For a given centrality, the Glauber calculations are used to determine the corresponding collision parameters: N_{part}, N_{coll}, and b.

1.3.2 Kinematic Observables

The momentum distributions are separated into components longitudinal and transverse to the beam axis. For a particle with 3–momentum vector $\boldsymbol{p}$, the longitudinal momentum, p_z, and boost-invariant transverse momentum, p_T, are defined as

$$p_z = |\boldsymbol{p}| \cos\theta, \tag{1.4}$$

$$p_T = |\boldsymbol{p}| \sin\theta, \tag{1.5}$$

where θ is the angle between $\boldsymbol{p}$ and the beam axis (dip angle). The transverse mass, m_T, of a particle with mass m is calculated from its transverse momentum, where

$$m_T = \sqrt{{p_T}^2 + m^2}, \tag{1.6}$$

and its energy is given by

$$E = \sqrt{|\boldsymbol{p}|^2 + m^2} \tag{1.7}$$

$$= \sqrt{p_z^2 + m_T^2}. \tag{1.8}$$

This allows us to define the rapidity, y, of a particle as a measure of its longitudinal momentum and energy:

$$E = m_T \cosh y, \tag{1.9}$$

$$p_z = m_T \sinh y, \tag{1.10}$$

from which we obtain

$$y = \frac{1}{2} \ln \left(\frac{E + p_z}{E - p_z} \right). \tag{1.11}$$

The convenience of using the rapidity is that it is Lorentz additive under a Lorentz boost. This allows a direct comparison of both p_T and y distributions between experiments with different collision energies.

When the mass of a particle is not known, the pseudorapidity η is used as a similar measure to the rapidity, where

$$\eta = \frac{1}{2} \ln \left(\frac{|\boldsymbol{p}| + p_z}{|\boldsymbol{p}| - p_z} \right) \tag{1.12}$$

$$= -\ln \left[\tan \left(\frac{\theta}{2} \right) \right]. \tag{1.13}$$

In the high momentum limit where $E \approx p$, the rapidity and pseudorapidity converge. These kinematic observables provide a direct measure of the temperature, pressure and energy density of the matter formed in heavy ion collisions.

Momentum spectra are used to obtain the invariant yield (cross-section),

$$\text{Yield} = \frac{\mathrm{d}^3 N}{\mathrm{d}\Omega}, \tag{1.14}$$

where N is the number of identified particles. The yield is normalized to the volume of phase-space in which particles where identified, $\mathrm{d}\Omega$. The boost invariant volume element in momentum-space co-ordinates is

$$\mathrm{d}\Omega = \frac{\mathrm{d}^3 p}{\mathrm{d}E} \tag{1.15}$$

$$= \frac{\mathrm{d}p_x \mathrm{d}p_y \mathrm{d}p_z}{\mathrm{d}E}. \tag{1.16}$$

To make use of the variables p_T and y, we use the coordinate transformation

$$(p_x, p_y, p_z) \rightarrow (p_T, \phi, y) \tag{1.17}$$

defined by

$$\begin{aligned} p_x &= p_T \cos\phi, & (1.18)\\ p_y &= p_T \sin\phi, & (1.19)\\ p_z &= m_T \sinh y. & (1.20) \end{aligned}$$

The coefficients of the coordinate transformation from x_i to x_i' are obtained from the determinant of the Jacobian matrix $\mathcal{J}$, defined as

$$\mathcal{J}_{ij} = \frac{\partial x_i}{\partial x_j'}. \tag{1.21}$$

For the coordinate transformation defined above, the resulting Jacobian is

$$\begin{aligned} \mathcal{J} &= \left| \begin{pmatrix} \cos\phi & \sin\phi & \frac{p_T \sinh y}{m_T} \\ -p_T \sin\phi & p_T \cos\phi & 0 \\ 0 & 0 & m_T \cosh y \end{pmatrix} \right| & (1.22)\\ &= p_T m_T \cos^2\phi \cosh y + p_T m_T \sin^2\phi \cosh y & (1.23)\\ &= p_T m_T \cosh y. & (1.24) \end{aligned}$$

It follows that

$$\begin{aligned} \frac{d^3p}{E} &= \mathcal{J}\frac{dp_T d\phi dy}{E} & (1.25)\\ &= \frac{p_T m_T \cosh y}{E} dp_T d\phi dy & (1.26)\\ &= p_T dp_T d\phi dy. & (1.27) \end{aligned}$$

Integrating over the azimuthal co-ordinate gives us the two-dimensional corrected yield

$$\text{Yield} = \frac{1}{2\pi p_T}\frac{\mathrm{d}^2N}{\mathrm{d}p_T\mathrm{d}y}. \tag{1.28}$$

If we reconstruct N_{Uncorr} particles in a total of N_{Total} collisions, the corrected yield is given as

$$N_{\mathrm{Corrected}} = \frac{N_{\mathrm{Uncorr}}}{\varepsilon}, \tag{1.29}$$

where the efficiency correction ε is made up of various components:

$$\varepsilon = \varepsilon_{\mathrm{acc}} \times \varepsilon_{\mathrm{rec}} \times \varepsilon_{e\mathrm{ID}}, \tag{1.30}$$

where $\varepsilon_{\mathrm{acc}}$ accounts for the detector accpetance, $\varepsilon_{\mathrm{rec}}$ takes the detector tracking efficiency into account, and $\varepsilon_{e\mathrm{ID}}$ describes the particle identification efficiency. This is described in more detail in Section 6.4. The invariant yield is obtained by normalizing the corrected yield to the phase-space of the experiment

$$\frac{1}{2\pi p_T}\frac{\mathrm{d}^2N}{\mathrm{d}p_T\mathrm{d}y} = \frac{1}{2\pi p_T}\frac{1}{\Delta p_T \Delta y}\frac{N^{\mathrm{Corrected}}}{N_{\mathrm{Total}}}, \tag{1.31}$$

where the factors 2π, Δy, Δp_T and N_{Total} describe the experimental coverage and number of collisions. The p_T-integrated invariant yield $\mathrm{d}N/\mathrm{d}y$ is obtained from Eq. (1.31), where

$$\frac{\mathrm{d}N}{\mathrm{d}y} = \frac{1}{\Delta y}\frac{N_{\mathrm{Corrected}}}{N_{\mathrm{Total}}}. \tag{1.32}$$

To constrain nuclear effects on J/Ψ particle production in heavy ion collisions, the invariant yield is compared to the yield obtained from p+p collisions. If there is no enhancement or suppression in heavy ion collisions due to the presence of nuclear matter, the yield should scale with the number of binary collisions. The nuclear modification factor R_{AA} is defined by

$$R_{\mathrm{AA}} = \frac{\mathrm{d}N/\mathrm{d}y\big|_{\mathrm{A+A}}}{N_{\mathrm{coll}} \cdot \mathrm{d}N/\mathrm{d}y\big|_{\mathrm{p+p}}}, \tag{1.33}$$

where $R_{\mathrm{AA}} = 1$ if there is no suppression or enhancement of the yield.

The following chapter will concentrate on the use of J/Ψ as a probe of the matter created in heavy ion collisions. This is followed by a motivation for investigating J/Ψ

in $d+$Au collisions, after which the experimental layout of the Relativistic Heavy Ion Collider is presented. Chapter 6 explains the analysis methods used in this thesis. Particle spectra and yields are shown in Chapter 7, after which conclusions are presented.

Chapter 2

J/Ψ as a Probe

Heavy ion collisions at relativistic energies may allow us to improve our understanding of QCD matter. Hard probes (e.g., J/Ψ) are created in the early stages of the collision, and are exposed to the evolution of the collision system. As a result, they can be used to provide information about the medium created in the high energy collision.

A brief motivation behind using charmonium as a probe of the QGP is given in Section 1.2. While colour screening is expected to suppress J/Ψ yields, experimental results have indicated that this is not the only mechanism affecting J/Ψ formation in heavy ion collisions.

In order to understand the medium formed in heavy ion collisions, it is essential to separate the different factors affecting J/Ψ yields. This chapter will describe the effects on J/Ψ production from the high energy density system created in heavy ion collisions.

2.1 Deconfinement, Recombination

In a state of partonic deconfinement, the mean free path of quarks and gluons is larger than the size of a nucleon. This is expected to occur due to the screening of the strong potential between quarks in the hot and dense matter created in heavy ion

collisions, as described in Section 1.1.1.

Originally, the suppression of J/Ψ as a signature of QGP formation was suggested by T. Matsui and H. Satz in the 1980's. They describe the effect of a hot, dense medium on J/Ψ formation [10], and calculate that above $T/T_c = 1.2$, colour screening in the QGP prevents charmonium formation. This led to the conclusion that an observation of J/Ψ suppression in heavy ion collisions would provide an unambiguous signature of QGP formation.

While J/Ψ suppression has been observed in heavy ion collisions (presented in Section 2.2), results from various experiments indicate that colour screening is not the only effect of the medium on J/Ψ production. This is discussed below, where results on J/Ψ suppression in heavy ion collisions from the CERN Super Proton Synchrotron (SPS) and RHIC are presented.

2.2 SPS Results

At the CERN-SPS, the NA38 [48], NA50 [49], and NA60 [50], experiments have carried out studies on J/Ψ production in various collision systems. To understand how the hot medium effects J/Ψ production, yields from p+A [51] collisions have been used as a baseline for J/Ψ production in the presence of cold nuclear effects (discussed in Chapter 3). Using this baseline, the suppression of J/Ψ production due to the hot medium has been calculated at NA50 for data from Pb+Pb collision at a beam energy of 158 GeV/nucleon on a fixed Pb target, and NA60 for data from In+In collisions at the same energy. The beam energy of 158 GeV/nucleon corresponds to a centre-of-mass collision energy of $\sqrt{s_{NN}} = 17.3$ GeV. The ratio of the measured yield to the expected yield based on p+A collisions is shown in Fig. 2.1 for In+In (circles), and Pb+Pb (triangles). A suppression of J/Ψ production is clearly observed, increasing towards more central events.

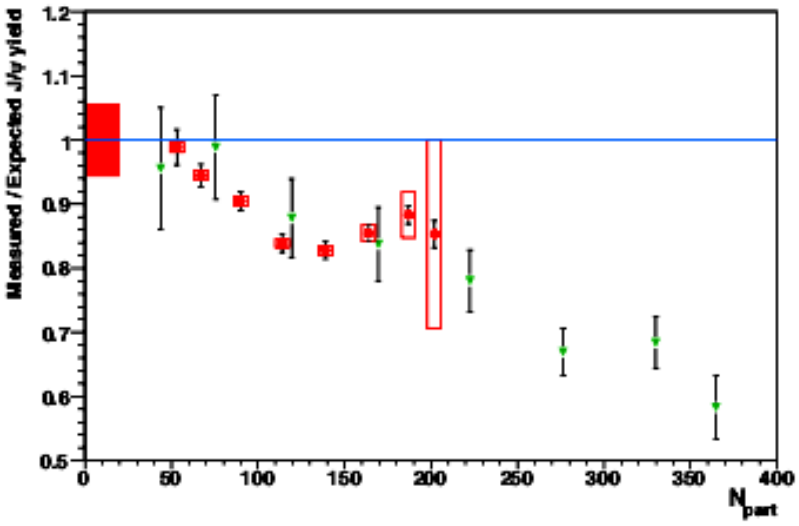

Figure 2.1: The suppression patterns measured in In-In collisions (NA60, circles) and Pb-Pb collisions (NA50, triangles) at $\sqrt{s_{NN}} = 17.3$ GeV at SPS, normalized to expected yields from p+A collisions. The 6% normalization uncertainty is indicated by the box on the left. Figure take from [50].

While many have interpreted this as hard evidence for QGP formation, the observed suppression at SPS has also be explained in terms of final state interactions of $c\bar{c}$ pairs, as described by the Comovers Interaction Model (CIM) [52].

2.3 RHIC Results

The RHIC experiment has collided together various beam species, focusing predominantly on p+p, d + Au, Au+Au, and Cu+Cu collisions, at $\sqrt{s_{NN}} = 200$ GeV. Due to the increase in centre-of-mass collision energy at RHIC compared to SPS (≈ 10 times higher), larger suppression of J/Ψ production at RHIC was expected.

The nuclear modification factor, defined in Eq. (1.33), has been calculated from Au+Au and p+p collisions at $\sqrt{s_{NN}} = 200$ GeV at PHENIX, shown in Fig. 2.2

(squares). Also shown are nuclear modification factors from S+U collisions at 200 GeV (NA38, circles), In+In collisions at 158 GeV (NA60, downward triangles), and Pb+Pb collisions at 158 GeV (NA50, upward triangles). Both experiments observe a suppression, with $R_{AA} < 1$ and decreasing as N_{coll} increases. The data from SPS collisions at energies of $\sqrt{s_{NN}} = 17.3$ GeV, and RHIC collisions at energies of $\sqrt{s_{NN}} = 200$ GeV, have similar amounts of suppression at midrapidity, which cannot be explained based solely on suppression due to colour screening in the hot medium.

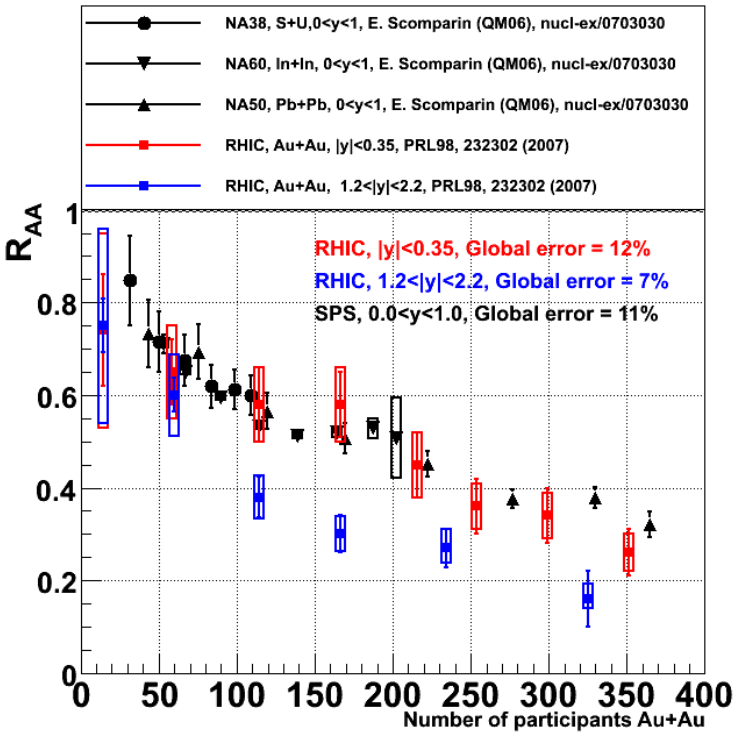

Figure 2.2: The nuclear modification factor for J/Ψ production in S+U collisions at 200 GeV (NA38, circles), In+In collisions at 158 GeV (NA60, downward triangles), Pb+Pb collisions at 158 GeV (NA50, upward triangles), and Au+Au collisions at $\sqrt{s_{NN}} = 200$ GeV (PHENIX, squares). Yields are normalised to yields in p+p collisions.

The J/Ψ suppression for forward rapidity and midrapidity in Au+Au collisions at PHENIX are shown in the top panel of Fig. 2.3, full and open circles, respectively. A stronger suppression, indicated by a smaller R_{AA}, is observed at forward rapidity, which is illustrated in the bottom panel of Fig. 2.3, where the ratio of R_{AA} for forward rapidity to R_{AA} for midrapidity is less than unity. This is also in contrast to expectations based on colour screening alone.

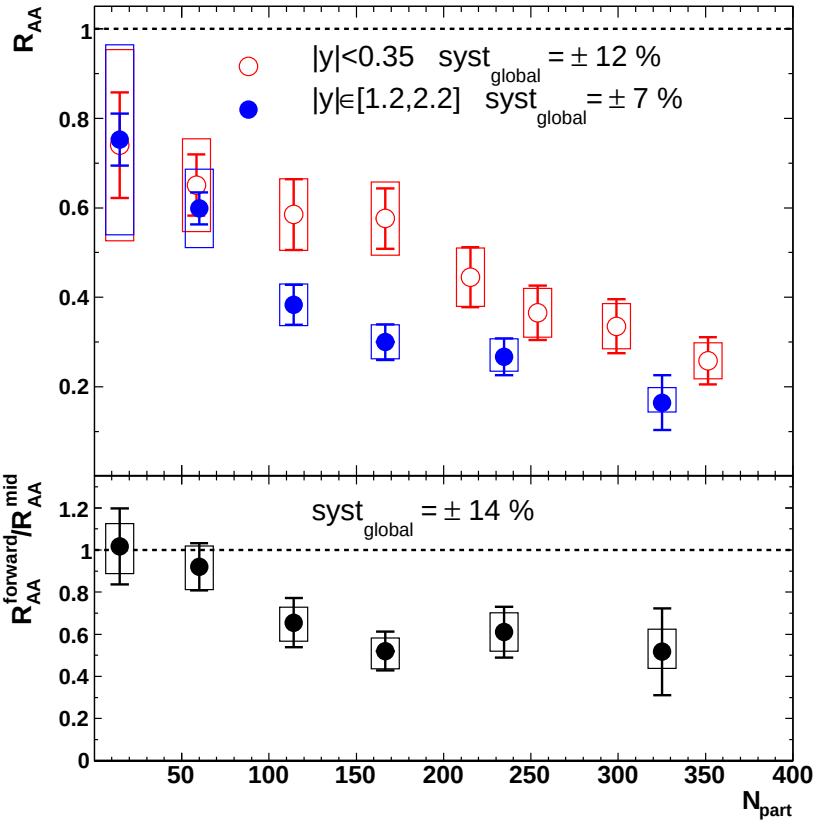

Figure 2.3: The nuclear modification factor for J/Ψ production at RHIC. More suppression is observed at forward rapidity. Figure taken from [58].

Due to the significantly higher density of $c\bar{c}$ pairs produced at RHIC energies compared to SPS, regeneration models [53, 54, 55] were proposed to account for the comparable amounts of suppression observed at these different collision energies.

Such models describe an enhancement of J/Ψ production at higher energies and temperatures due to the coalescence of charm quarks into bounds states of J/Ψ in the later stages of the collision system (recombination), which suggest similar amounts of suppression at SPS and RHIC energies. Recombination also explains the larger suppression observed at forward rapidity, as the charm quark density is much smaller than at midrapidity.

This thesis will focus on constraining cold nuclear matter effects on J/Ψ production in $d+$Au collisions. Further detail on cold nuclear effects is given in Chapter 3.

Chapter 3

Cold Nuclear Effects

While much of the focus of heavy ion collisions has been on probing the Quark Gluon Plasma, it is essential that QCD matter be studied under different temperatures and energy densities in order to fully understand the nuclear properties. Accelerator experiments have collided a wide range of nuclei at various collision energies in an attempt to disentangle the nuclear effects due to the presence of a QGP from effects due to nuclear matter which is not excited. Such effects are described below.

The formation of QGP is expected to occur in high energy heavy ion collisions (Au+Au, Pb+Pb, etc.). As presented in Chapter 2, significant suppression has been observed at the CERN-SPS by the NA50 [49, 59] in Pb+Pb collisions, and NA60 [50] in In+In collisions, both at collision energies of $\sqrt{s_{NN}} = 17.3$ GeV, and at RHIC by the PHENIX experiment in Au+Au [58] and Cu+Cu [60] at $\sqrt{s_{NN}} = 200$ GeV.

The comparable amounts of suppression at midrapidity between SPS and RHIC came as a surprise, as the factor of $200/17.3 \approx 12$ increase in collision energy at RHIC compared to SPS is expected to increase the effect of suppression due to colour screening. A larger suppression observed at forward rapidity in Au+Au collisions at $\sqrt{s_{NN}} = 200$ GeV at PHENIX also suggest effects beyond colour screening.

There are many nuclear effects which may contribute to a modification of J/Ψ

production in A+A collisions relative to scaled p+p collisions, other than J/Ψ suppression due to the presence of a QGP. Since QGP formation requires high energy densities, it is known as a hot nuclear matter effect. There are also modifications to J/Ψ production in heavy ion collisions due to the presence of non-excited nuclear matter. Such modifications are known as cold nuclear matter effects [57, 61, 62]. Lighter systems, such as p+A and d+A collisions, do not reach the energy densities required for QGP formation, and provide a means to quantify the cold nuclear matter effects. A quantitative understanding of the cold nuclear matter effects is essential when investigating hot nuclear matter effects and trying to understand the QGP.

The presence of cold nuclear matter can modify J/Ψ production at different stages of the collision system. Initial-state effects occur before the formation of $c\bar{c}$ pairs, while final-state effects are those which affect the already created $c\bar{c}$ pairs. At midrapidity, the dominant contributions are the modification of the nuclear Parton Distribution Function (nPDF) in the initial state, and the nuclear absorption of $c\bar{c}$ pairs in the final state. A brief description of these effects is given below.

3.1 Modification of the nuclear Parton Distribution Function

There is a modification of J/Ψ production in collision systems involving heavy nuclei (e.g. Au, Cu, Pb). The nucleons inside a bound nuclei do not behave as free nucleons, and as a result, p+A, d+A, and A+A collisions cannot be treated as a superposition of nucleon-nucleon collisions.

The distribution of quarks and gluons within a nucleon are described by the Parton Distribution Functions (PDFs). These PDFs are modified in a nucleus as compared to that in a proton due to the presence of other nucleons. The modification of the

nuclear Parton Distribution Function, known as shadowing, is defined by the ratio

$$R_i(x, Q^2, A) = f_i^A(x, Q^2)/A \cdot f_i^p(x, Q^2), \tag{3.1}$$

where the Bjorken variable, x, is the fraction of the nucleon momentum carried by parton i, Q^2 is the square of the momentum transfer, A is the nucleus size, and f_i^A and f_i^p are the parton distributions in a nucleus and proton, respectively. If the ratio $R_i(x, Q^2, A)$ is unity, there is no modification of the nPDF, and collisions of nuclei can be treated as a superposition of nucleon-nucleon collisions.

The modification of parton densities is measured by probing quark distributions in deep inelastic scatterings of e+A and e+p collisions [64, 66], which have been used to constrain the free PDFs. Drell-Yan measurements, which involve the annihilation of quark anti-quark pairs, also provide information on the anti-quark densities. Since gluons do not carry electromagnetic charge, there is no no way to directly measure the gluon distributions, resulting in a large uncertainty in the gluon densities. Since J/Ψs are produced primarily via gluon fusion, their production is sensitive to the modification of the gluon nPDF.

The ratio given in Eq. (3.1) for gluons, with $Q^2 = m^2_{\mathrm{J}/\Psi}$, is shown in Fig. 3.1 versus Bjorken x [65]. For low x ($x < 0.02$), the gluon density inside the nucleus is lower than the scaled gluon density in a free proton, and the ratio of nuclear parton density to the nucleon parton density, R_g^{Au}, is less than unity. The decrease in the number of gluons results in a decrease in J/Ψ formation, causing a shadowing effect. This is in contrast to the intermediate range $0.02 < x < 0.1$, in which an increased gluon PDF in the nucleus will enhance J/Ψ production. This known as an anti-shadowing effect.

As the collision energies increase, it is possible to probe smaller values of x when producing J/Ψs. The shaded boxes in Fig. 3.1 indicate the Bjorken x probed in different experiments, from top to bottom: NMC, SPS, FNAL, HERA-B, and RHIC. While anti-shadowing is expected at SPS energies, a suppression of J/Ψ production due to shadowing is expected at RHIC. The strength of the shadowing at RHIC is not

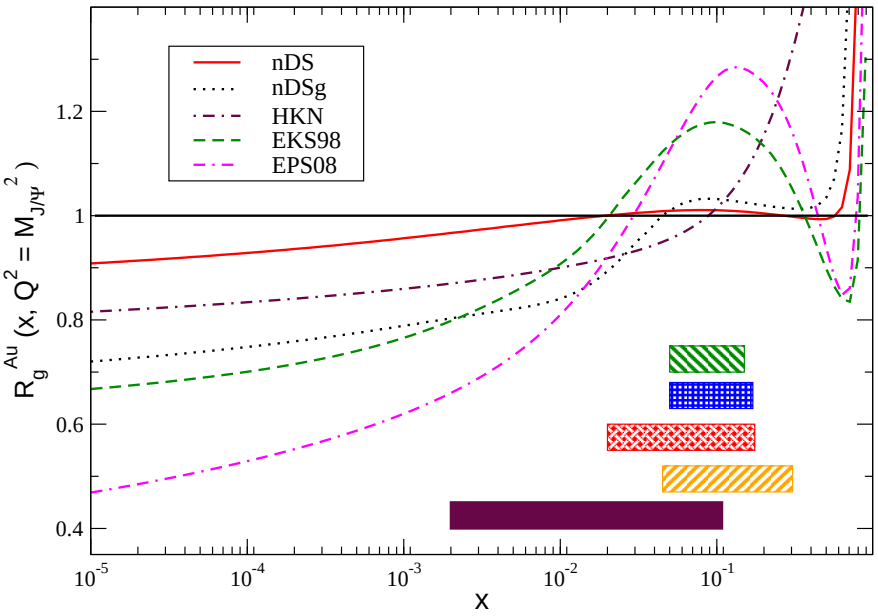

Figure 3.1: The modification to the gluon parton distribution function in a gold nucleus relative to that in a proton, versus Bjorken x using various parametrization. The bands indicate the range of x probed in NMC, SPS, FNAL, HERA-B and RHIC experiments (top to bottom). Figure taken from [65].

well constrained, indicated by the $\approx 20\%$ variation between different models shown in Fig. 3.1. A precise measurement of the charm cross section at RHIC will improve the constraints on the modification to the gluon PDF.

3.2 Nuclear Absorption

The $c\bar{c}$ pairs created in heavy ion experiments are produced in the initial hard scattering of the partons from the beam and target (fixed target experiment) or from the colliding beams (collider experiment). The charm quarks produced in this early stage of the collision are subject to subsequent collisions within the nucleus. The nuclear

absorption of J/Ψ occurs when these interactions break up the $c\bar{c}$ pair,

$$\mathrm{J}/\Psi + N \rightarrow \text{open charm.} \tag{3.2}$$

The magnitude of this effect depends on the nuclear absorption cross section for charmonium, $\sigma_{\mathrm{J}/\Psi N}$.

It is still unclear how the nuclear absorption should depend on collision energy, i.e., whether $\sigma_{\mathrm{J}/\Psi N}$ increases due to the more energetic collisions of the $c\bar{c}$ pairs with other partons at higher energies, or if the increased flattening of the nuclei at higher energies means that there are less collisions between the $c\bar{c}$ pairs and other partons, decreasing the nuclear absorption [65]. Values of the J/$\Psi - N$ cross section have been extracted from various data sets using the EPS08 [67] parametrization, shown in Fig. 3.2. The absorption cross section ranges from $\sigma_{\mathrm{J}/\Psi N} \approx 2 - 10$ mb, and there are very few measurements at low x.

Since theory does not provide strong constraints on cold nuclear matter effects in J/Ψ production, quantifying these effects relies on experiment. The RHIC experiment provides large collision energies which enable measurements at low x, where these effects are not well understood. Collisions of $d+$Au provide an environment where cold nuclear matter effects can be quantified. In this analysis, the production of J/Ψ in $d+$Au collisions has been studied to understand the cold nuclear effects on J/Ψ production. These results have been compared to data from p+p collisions (see Chapter 7) to determine the modification of J/Ψ production due to cold nuclear effects.

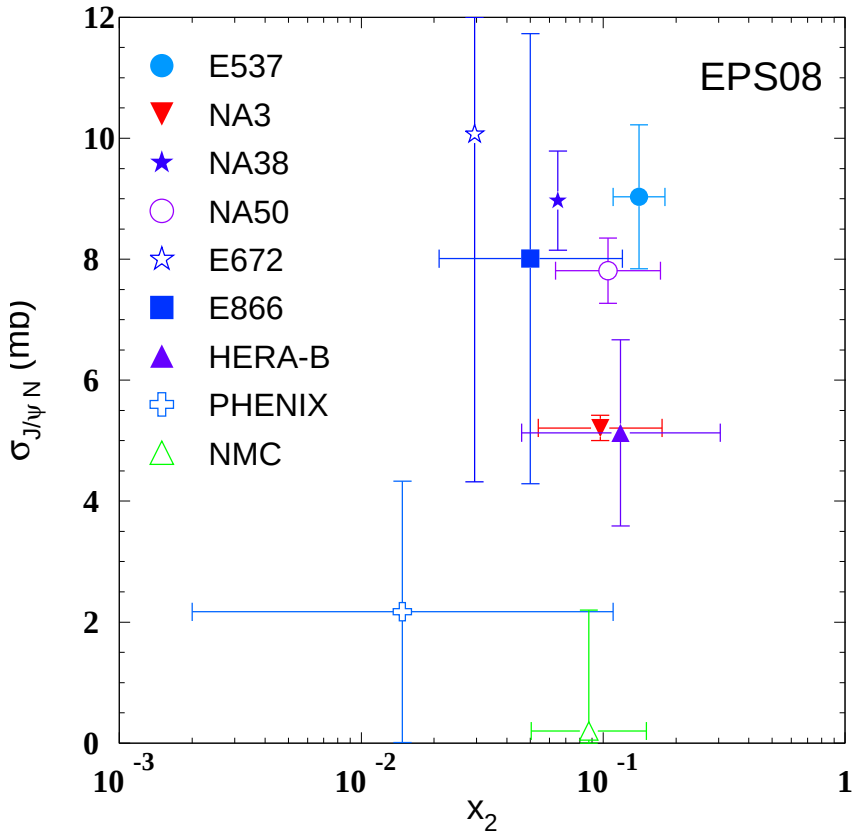

Figure 3.2: The J/Ψ − N cross section from various data sets, using the EPS08 parameterisation for the nPDFs. Figure taken from [65].

Chapter 4

Experimental Setup

The Relativistic Heavy Ion Collider (RHIC), located at BNL in Upton, New York, USA, has housed four experiments since its construction in 2000, namely the Solenoidal Tracker at RHIC (STAR), the Pioneering High Energy Nuclear Experiment (PHENIX), the Broad Range Hadron Magnetic Spectrometers Experiment (BRAHMS), and PHOBOS. Currently, only STAR and PHENIX are in operation. This analysis presents data taken by the STAR detector.

4.1 The RHIC Accelerator Complex

The Relativistic Heavy Ion Collider is a circular particle accelerator with a circumference of 3.8 km. The STAR experiment, which is located at the 6 o'clock position in the ring, and PHENIX, located at the 8 o'clock position, are the larger of the four experiments. RHIC is the first collider in the world capable of accelerating ions to relativistic speeds, opening a new energy regime compared to the previous fixed target experiments, such as SPS and AGS.

A diagram of the RHIC complex is shown in Fig. 4.1. It consists of various facilities that are used to accelerate charged nuclei. Gold (Au) and copper (Cu) atoms are partially stripped of their electrons entering and exiting the Tandem Van de Graaff Accelerator, where they are accelerated to 1 MeV/c. They are then sent through the

Tandem-to-Booster Line to the Booster Synchrotron, accelerated and further stripped of electrons, before being injected into the Alternating Gradient Synchrotron (AGS). Protons are injected directly into AGS from the 200-MeV Linac. The heavy ions are stripped of their remaining electrons, and the protons or ions are bunched together and accelerated to the RHIC injection energy of 10.8 GeV/A and transferred to RHIC via the AGS-to-RHIC Beam Transfer Line.

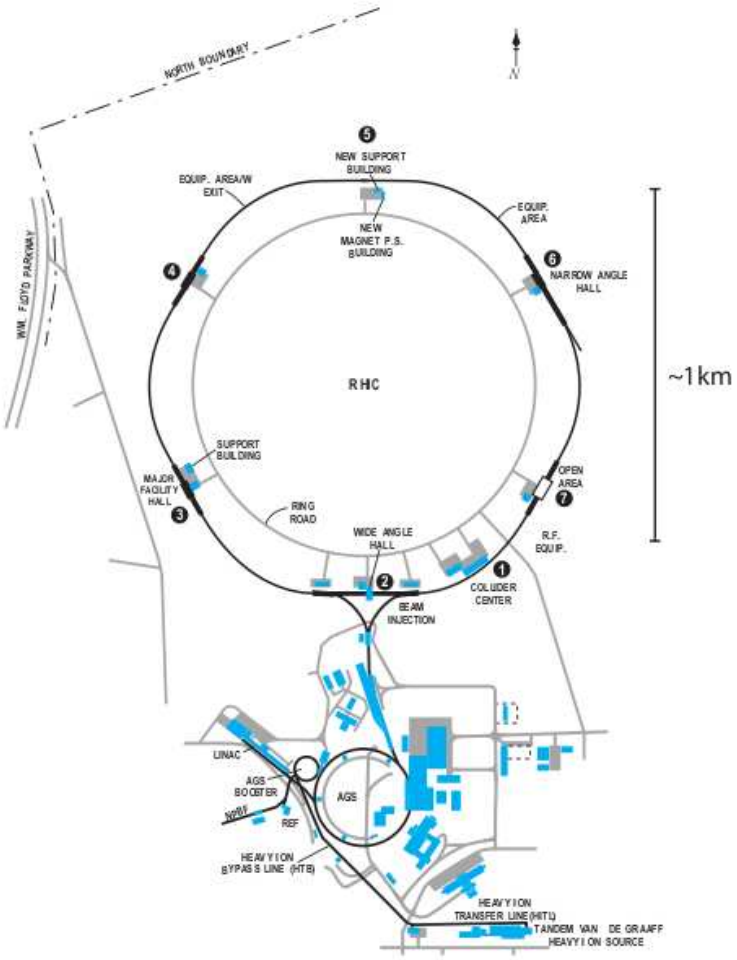

Figure 4.1: The RHIC facility

The RHIC facility contains two intersecting storage rings, in which the counter-rotating beams are steered and accelerated by superconducting magnets. There are six possible collision points on the hexagonal ring. The ions are accelerated at collision energies up to $\sqrt{s_{NN}} = 200$ GeV, and protons up to $\sqrt{s_{NN}} = 500$ GeV.

4.2 STAR Experiment

A layout of the STAR detector is shown in Fig. 4.2. The large solenoidal magnet has an outer radius of 7.32 m and a length of 6.85 m. The magnet creates a near-uniform magnetic field in the longitudinal plane (parallel to the beam), which curves the trajectories of charged particles. The maximum field strength that the STAR magnet can achieve is 0.5 T. It is operated at full field, full reverse field, and half field strength. The STAR coordinate system is Cartesian, with the origin at the centre of the TPC, the z direction pointing to the West along the beam, y pointing upwards, right-handed.

The sub-system central to the tracking and particle identification in STAR is the Time Projection Chamber (TPC). This large acceptance detector is surrounded by the Barrel Electromagnetic Calorimeter (BEMC). The Time of Flight (ToF) detector, located between the TPC and BEMC, was only partially installed in 2008. When completed in 2010, the ToF will greatly improve particle identification capability of STAR, in conjunction with the TPC. The Forward Time Projection Chambers (FTPC) are located to the East and to the West of the TPC, and provide tracking and identification abilities similar to the TPC in the forward and backward rapidity regions. The Vertex Position Detector (VPD) and Zero Degree Calorimeter (ZDC), shown in Fig. 4.3 and discussed in the next chapter, are used for triggering and are located along the beam line outside of the magnetic field. The Beam Beam Counters (BBCs) are also located on either side of the interaction region, and are used in this analysis in conjunction with the ZDC to monitor beam rates. The BBC is made up of hexagonal scintillator tiles: 2 outer rings of larger tiles, and 2 inner rings of smaller tiles, as shown in Fig. 4.4.

This analysis primarily uses the TPC and BEMC detectors, which are discussed below. Details of the other STAR sub-systems can be found in [74].

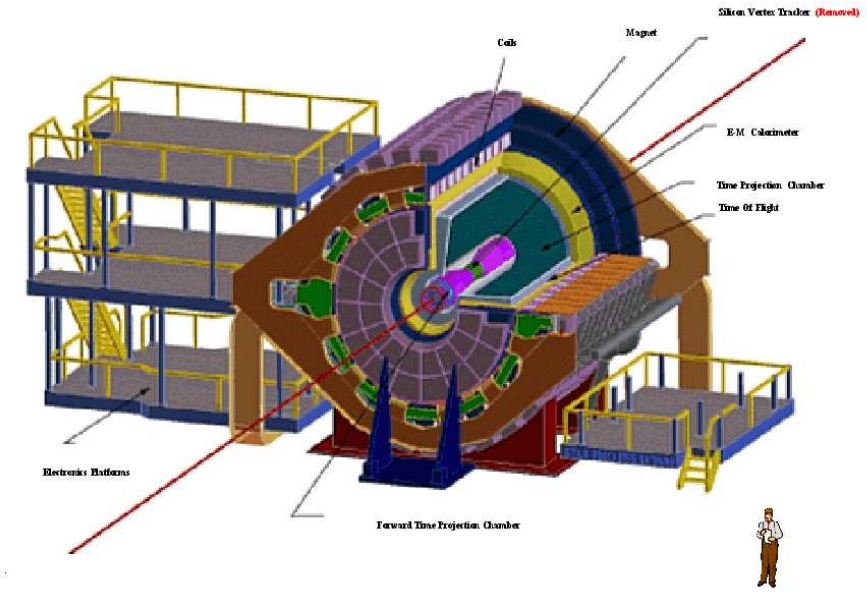

Figure 4.2: The STAR detector

4.2.1 Time Projection Chamber

The TPC, shown in Fig. 4.5, is a 4.2 m long cylindrical gas chamber, which spans the full azimuthal angle, $0 \leq \phi \leq 2\pi$, and has pseudorapidity coverage of $-1.8 \leq \eta \leq 1.8$. The TPC is located inside the STAR magnet, and has an inner radius of 50 cm and an outer radius of 200 cm.

The TPC volume is filled with P10 gas, which is a mixture of 90% Argon and 10% Methane, kept at atmospheric pressure. The central membrane, which separates the East and West halves of the TPC, is held at a voltage of -28 kV. The endcaps

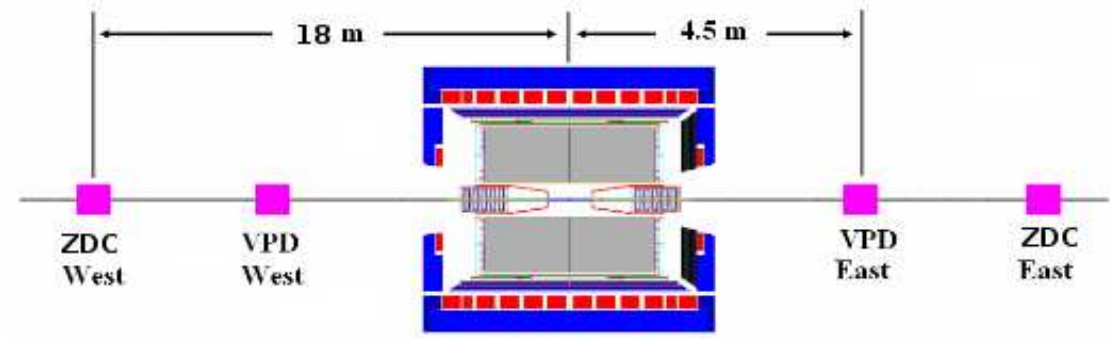

Figure 4.3: A cross-view of STAR detector with the VPD and ZDC detectors shown on both sides of the TPC.

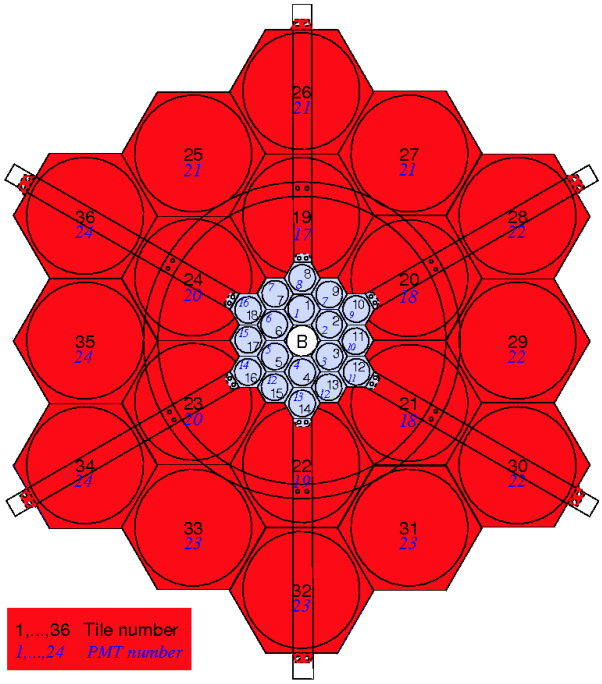

Figure 4.4: A front view of the BBC at STAR.

of the TPC are instrumented with multi-wire proportional chambers (MWPC), each consisting of 12 readout sectors. The endcaps are grounded, and a uniform electric

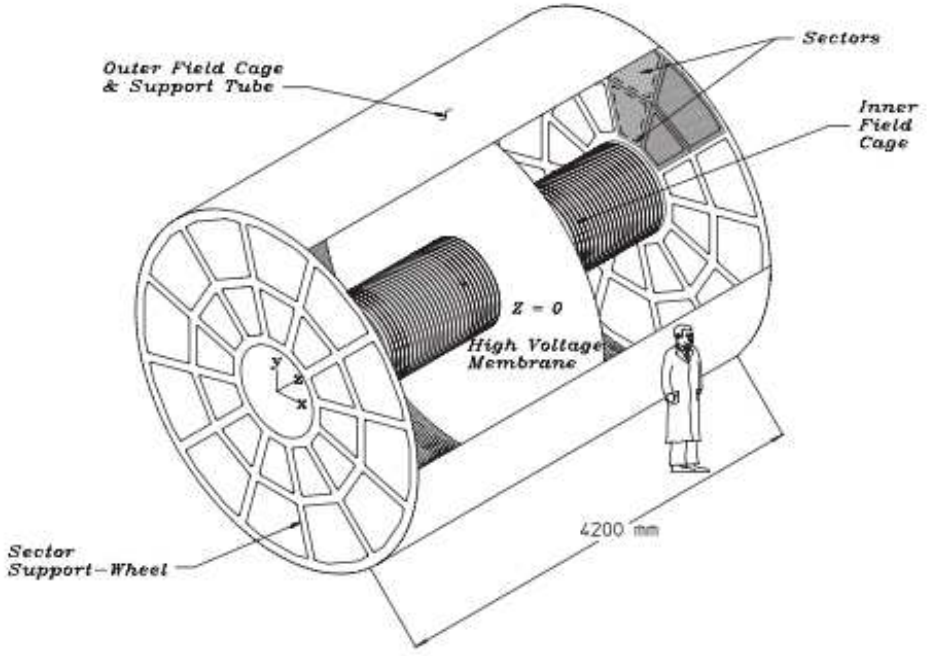

Figure 4.5: The Time Projection Chamber.

field of $E_Z \approx 135$ V/cm is maintained between the chambers and the membrane. Copper strip resistors, which are located on the surface of the field cage of the TPC, form a uniform field across the gas volume. As charged particles traverse the TPC, they ionise atoms in the gas. The ionisation electrons drift at a constant speed of 5.45 cm/μs to the endcaps, with a maximum drift time of 40 μs. By measuring the total charge of these electrons in the endcaps, the energy loss per unit length, $\mathrm{d}E/\mathrm{d}x$, can also be determined, as described in the next section.

Each endcap sector contains 45 pad rows, divided into inner and outer sub-sectors. The inner sectors have a higher pad density to accommodate the higher track densities, and pad dimensions are chosen to optimise the x and y position resolution of drift electrons. The z position is determined from the arrival time of the signal

relative to the collision time, taken as $t = 0$. The tracking resolution of the TPC at the vertex is $100 - 150$ μm. The recorded spatial distributions of charge are used to reconstruct particle trajectories, as described in the next section.

The uniform magnetic field applied across the TPC causes charged particles to bend in the plane transverse to the beam line. By measuring the curvature and trajectory of the tracks, the charge and momentum of particles can be determined. This information, combined with the expected $\mathrm{d}E/\mathrm{d}x$ values (see Fig. 4.8) for particular particle species allows for accurate particle identification.

4.2.2 Barrel Electromagnetic Calorimeter

The Barrel Electromagnetic calorimeter covers full azimuth of $0 \leq \phi \leq 2\pi$ and, pseudorapidity of $-1 \leq \eta \leq 1$. This fast detector (read-out time ≈ 10 ns) contains 4800 individual calorimeter towers, with dimensions $\Delta\eta = 0.05$ and $\Delta\phi = 0.05$ rad. At midrapidity, this is equivalent to a tower size of 10 cm $\times$ 10 cm. Figure 4.6 shows an event display, where the illuminated regions indicate energy deposited in the BEMC towers by passing particles.

Each tower has a sandwich geometry, consisting of 20 and 21 alternating layers of 5 mm thick lead absorber and scintillator plates, respectively, which achieve an energy resolution of $\approx 14\%/\sqrt{E}$. The light created by particles striking the scintillating plates is transported by wavelet shifting (WLS) optical fibers to photomultipliers outside of the STAR magnetic field.

The Barrel Shower Maximum Detector (BSMD) is located at a depth of approximately 5 radiation lengths in the calorimeter modules, as shown in Fig. 4.7. Particles that collide with the lead absorber plates radiate energy. The shower shape created from this radiation is well understood and is very different for hadrons and electrons/photons. Hadrons either pass through the lead as a minimum ionizing particle

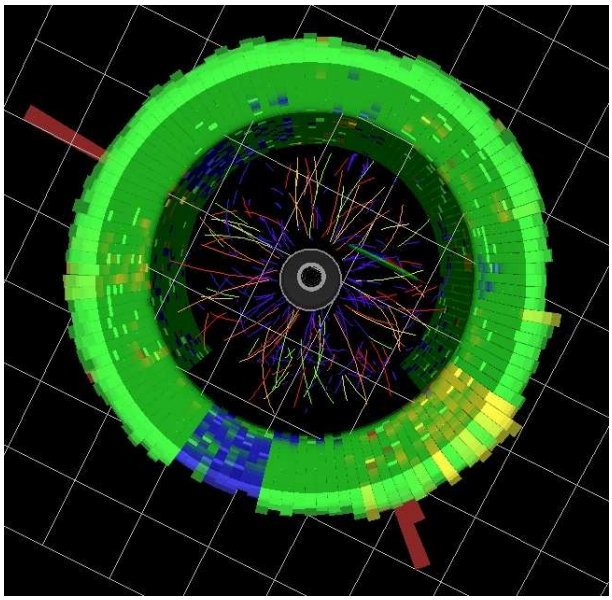

Figure 4.6: STAR event display, showing the BEMC tower energy depositions.

(MIP) or create an irregular shower shape after a hadronic interaction with the material. On the contrary, electrons have a well constrained conical shower shape. This distinction provides an additional tool for electron-hadron discrimination.

In this analysis, only the BTOW in the BEMC was used to provide information on the energy of particles reconstructed by the TPC.

4.2.3 Event Reconstruction

Ionisation Energy Loss

The energy lost by particles traversing the gas volume is directly related to the number of drift electrons they free. Each pad in the endcaps reconstructs the energy deposited into it as a $\mathrm{d}E/\mathrm{d}x$ hit, and there can be up to 45 $\mathrm{d}E/\mathrm{d}x$ hits for each track. The energy deposition $\mathrm{d}E/\mathrm{d}x$ has a Landau distribution, with long tails at higher values. To reduce fluctuations, a truncated mean is calculated from the lower

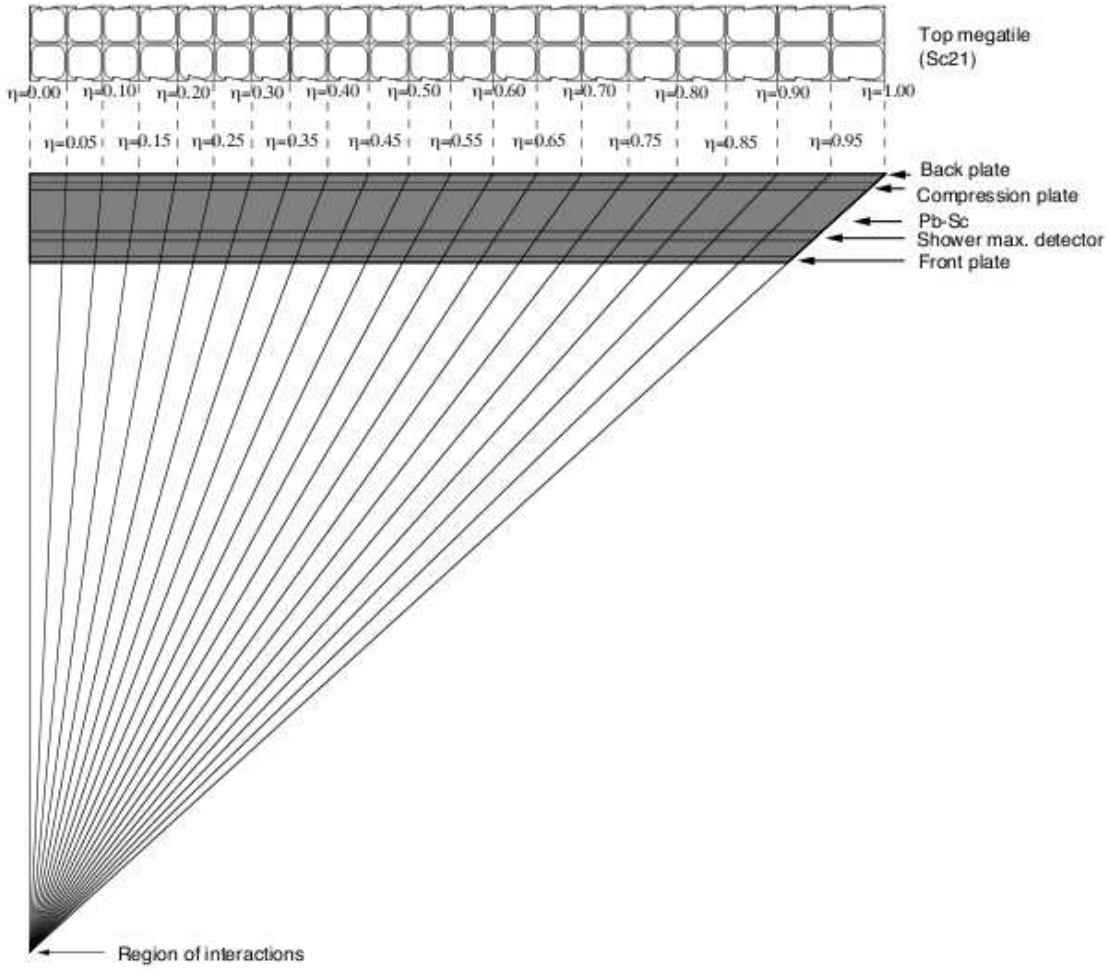

Figure 4.7: A side view of a module in the BEMC.

70% of $\mathrm{d}E/\mathrm{d}x$ measures, and the upper 30% of values are discarded.

Figure 4.8 shows the energy loss of electrons, kaons, protons, pions, and deuterons in the momentum range $0.1 < p < 6$ GeV/c (particles below 0.1 GeV/c do not reach the TPC, and the statistics is insufficient above 6 GeV/c). The electron energy loss is mostly constant with momentum, while the hadrons have an initial fall-off and a relativistic rise at higher energies. The Bethe-Bloch parametrization of particle

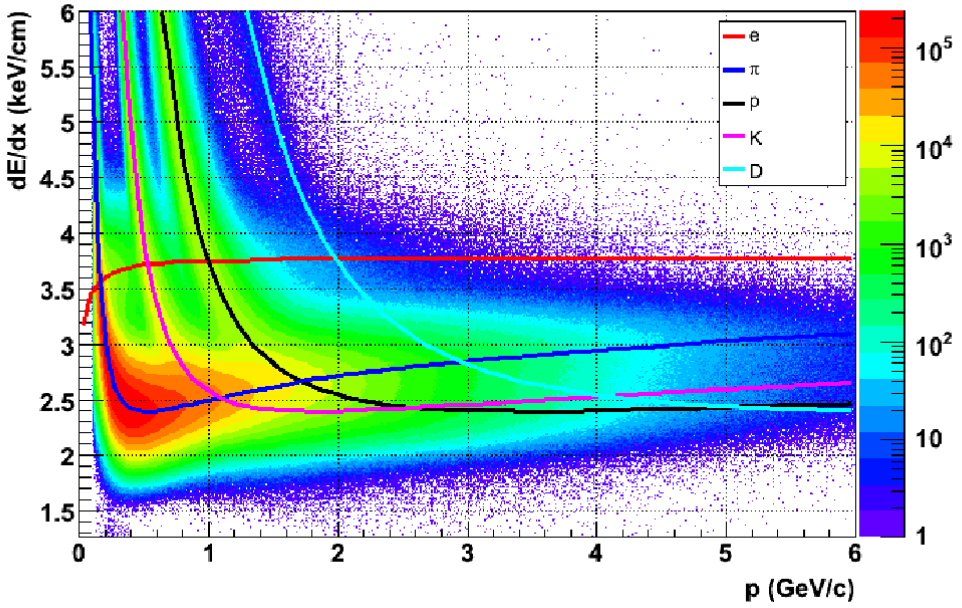

Figure 4.8: $\mathrm{d}E/\mathrm{d}x$ versus momentum of particles created in $d+\mathrm{Au}$ collisions passing through the TPC.

$\mathrm{d}E/\mathrm{d}x$, shown in solid bands in Fig. 4.8, represents the mean energy loss for various particles.

Track Reconstruction

When a particle traverses the TPC volume, it deposits energy in the form of ionization electrons. The charge deposited in the gas is known as a hit, and each track can have up to 45 hits. In order to determine the spatial coordinates and ionization energy of the reconstructed hits, the cluster finder algorithm looks for hit clusters in 2 dimension (time and padrow), and then single and multiple hits are searched for in each cluster. The ability to resolve nearby clusters is crucial for the $\mathrm{d}E/\mathrm{d}x$ reconstruction and for resolving close tracks. More detail on this can be found in [39].

The track reconstruction process uses the reconstructed spatial hits to map a 3-dimensional trajectory of the charged particles. Before hits are used, their reconstructed positions need to be corrected for several distortion effects [76]: (1) space charge, where ions, accumulated in the gas, distort the $\boldsymbol{E}$ and $\boldsymbol{B}$ fields, (2) field alignment, where the slight misalignment of the $\boldsymbol{E}$ and $\boldsymbol{B}$ fields creates a cross component $\boldsymbol{E} \times \boldsymbol{B}$, and (3) grid leak, where electrons leak back into the gas from the endcaps, distorting the $\boldsymbol{E}$ field. These effects are understood and corrected for during data production.

Once hits are corrected, the tracking algorithm uses hits in the outer sectors of the endcaps as track seeds. From these seeds, extrapolations are done to associate other hits with the track, taking into account multiple scattering and Coulomb effects. These hits are grouped to form track segments, which are extrapolated and joined to form complete tracks. After this, outlying hits are removed from the fits and the fitting process is repeated. The direction of track curvature determines the charge of the particle, and the magnitude of curvature determines the transverse momentum of the particle:

$$p_T = 0.3\, q\, B\, R \text{ GeV}/c, \tag{4.1}$$

where q is the charge in the units of $+e$, B is the magnetic field strength in Tesla, and R is the radius of curvature in metres. The 3–D particle momentum is calculated from the p_T, azimuthal, and dip angles of the trajectory.

Vertex Finding

Tracks reconstructed by the track finding algorithm, known as global tracks, are used to determine the position of the collision vertex. Global tracks are projected onto the beam axis, and a vertex is found at a position that at least five tracks point to, within a ± 2.5 cm window along z. This point is determined by the Minuit fitting algorithm, which locates the (x, y, z) position, from which the distance of closest approach (DCA) to all the tracks is within 5 cm. Due to the high collision rates at RHIC in 2008, there can be as many as 20 reconstructed vertices per event. This

effect, known as pile-up, is discussed in Chapter 5.

Tracks within 3 cm of the vertex position, known as primary tracks, are considered to belong to the collision. Their helices are refitted with the constraint that they pass through the vertex.

Information from other detectors is combined with the reconstructed event, and these events, which contain all track geometry and kinematics, are used in analysis.

Chapter 5

Trigger, DAQ and Data Quality

With the increased precision in beam focusing and steering, the instantaneous luminosity delivered by RHIC has increased dramatically since the first collisions in 2000 (Fig. 5.1 shows projected luminosities beyond 2009). Since the TPC read-out time is longer than the time between bunch crossings, care has to be taken to trigger on the collision of interest and to identify and remove tracks from other collisions. Distortions due to the space charge that accumulates in the large volume of the TPC, magnetic field imperfections, and sector mis-alignments have a large impact on tracking quality and resolution. Some of these effects have increased substantially with the higher luminosities. Extensive calibrations and analysis was done to understand and correct for these effects, both online and offline [77].

A major difference in the STAR detector configuration between Run 8 (taken in 2008) and previous runs was the removal of tracking devices that surrounded the beam pipe, which has reduced the background by a factor of 10.

5.1 Triggering

Since the bunch crossing rates are much higher than the maximal TPC readout rates, it is not possible to read out all STAR detectors every event. Multiple trigger criteria

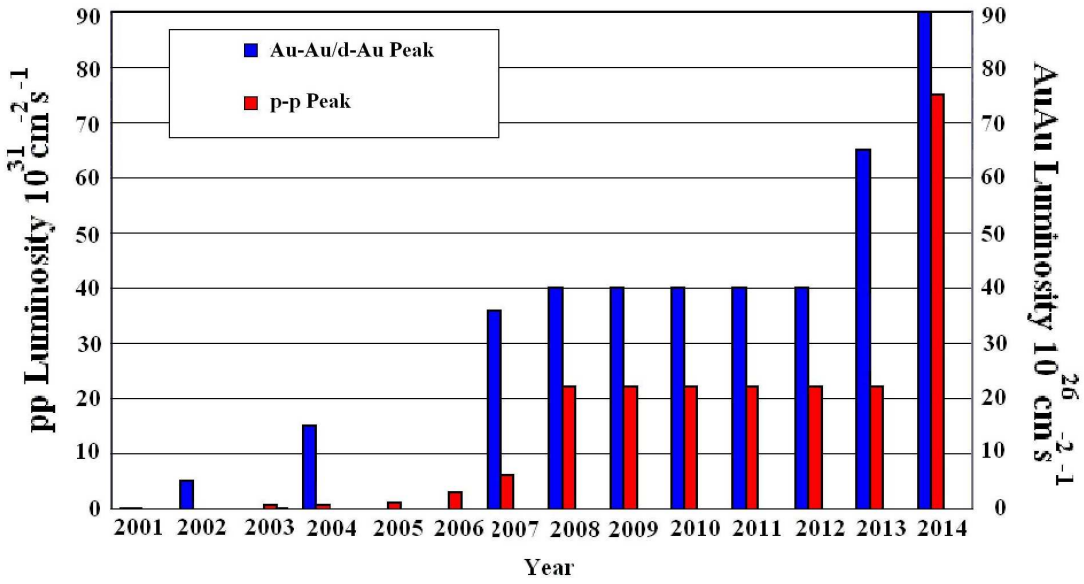

Figure 5.1: Recorded and projected instantaneous luminosities delivered to STAR. Figure taken from [78].

were developed to identify collisions of interest for specific physics measurements. We present data acquired using a minimum bias (MB) trigger on events recorded with the TPC.

The MB trigger has a low threshold on accepted collisions that occur within the TPC. The detectors used in the minimum bias trigger in Run 8 $d+$Au collisions are the Vertex Position Detector (VPD) and the East Zero Degree Calorimeter (ZDC-E). The VPD, shown in Fig. 4.3, is located on both sides of the interaction region close to the beam line. It determines the vertex position by measuring the time difference between the signals detected at its East and West positions. In this analysis, the VPD was not used to determine the vertex position because of it's low efficiency in low multiplicity collisions or in the presence of event pile-up. For the MB trigger, the VPDs require the online vertex position to fall within ± 30 cm of the nominal interaction point $(0, 0, 0)$. The two Zero Degree Calorimeters, also shown in Fig. 4.3,

are located at both sides of the interaction region at $\theta = 0^{\circ}$ and cover an angle of 2.5 mrad around the beam axis. When the deuteron and gold ions collide after the d+Au collision, fragments of the gold nucleus continue along the beam direction. Charged particles bend away from the ZDCs by the RHIC magnetic dipoles, while neutrons from the broken up Au nucleus are detected by the ZDC-E. The minimum-bias trigger requires that the ZDC-E detects at least one neutron in an event.

5.2 Data Acquisition and Production

During the run, all detectors send the raw information from triggered events over optical fibers to the Data Acquisition System (DAQ).

To understand the amount of background in the subsystems, pedestal runs of the detectors are taken in the absence of beam. Lasers are also used in the TPC to calculate the drift velocity in the gas and to determine spatial distortions [80], since the laser beams are unaffected by the magnetic field.

The RHIC experiments use the RHIC Computing Facility (RCF) at BNL to store data taken during the run. The Lawrence Berkeley National Laboratory (LBNL) computing facility also uses the Parallel Distributed Systems Facility (PDSF) linux farm at the National Energy Research Scientific Computing Center (NERSC) for additional STAR data storage. After the run is finished, final calibration constants are applied and corrections are made for distortions due to experimental imperfections. The data is then streamed into Micro Digital Storage Tapes (μDSTs), which contain all necessary information for physics analyses.

5.3 Data Quality

Although much work is done both online and offline to ensure the data quality, the final dataset available to the user must still undergo scrutiny to achieve a high level of precision and quality in the analysis. A general quality analysis of reconstructed

vertices and tracks is presented in Chapter 6. Below we discuss several quality issues specific to the $d+$Au collisions in 2008.

5.3.1 Corrupt Scaler Rates

The scaler rates refer to the beam rates recorded by the ZDCs and BBCs. Some of these are used to understand and correct for the distortion effects in the TPC due to space charge, as the magnitude of this effect depends on the collision rates recorded by the scalers. During Run 8, there were moments when the rates from the BBC and the ZDC were temporarily stuck at values of precisely 2 or 3 times higher than the correct values. Such hardware failure, while only happening approximately once in 1000 events, can have a significant impact on physics analysis. Because the distortion correction affects tracking in the TPC, incorrectly applying this correction can shift all reconstructed tracks systematically in one direction. For high momentum tracks, a small shift in the position of one hit can significantly affect the reconstructed momentum of the particle. Although statistically negligible for many studies, this cannot be ignored for physics involving rare probes, and so a method to exclude these corrupt events was developed.

Identifying and removing events with stuck scaler rates during data production is simple and has been implemented for subsequent runs. However, since this problem was discovered post-production for the $d+$Au run, a solution needed to be developed and implemented on an analysis level. Large fluctuations of the delivered beam rates and the decrease of instantaneous luminosity over time within a beam fill made the events with stuck scaler rates hard to identify directly. To correct for the in-fill decrease of beam rates, scaler data were normalized using ratios of the rates observed in different scaler boards. From these ratios, a large part of the in-fill systematics was removed and clear instances of the scaler rates stuck at integer multiple values were identified and removed, decreasing statistics by only $\approx 1\%$. An illustration of this is shown in Fig. 5.2, where the ratio of the ZDC coincidence rate and BBC coincidence

rate is plotted versus the beam fill number. While most events have a ratio of approximately 0.3, instances where this value is a factor of 2 higher or lower are observed (see the band around 0.15 and 0.6 where the mean values have halved and doubled, respectively). The value of ~ 0.3 is then used as a baseline for the ratio of these scaler boards. Since the space charge corrections do not rely on the BBC coincidence rate, only events where this ratio is above 0.42 (corresponding to stuck values of the ZDC coincidence rate) are rejected. The cut-off value of 0.42 was chosen to exclude any entries that have ZDC scaler entries which are double the values in the central band, while not removing any values which belong to the central band around 0.3. This approach is repeated for all scalers which affect the space charge correction.

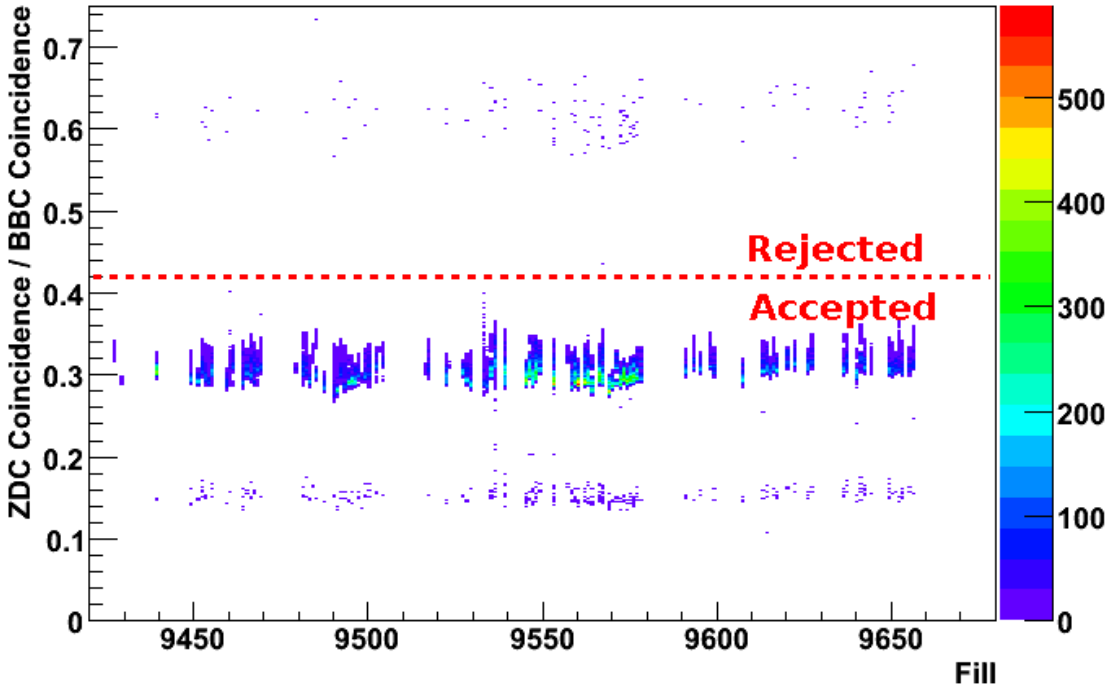

Figure 5.2: Scaler rates used in the space charge calibration. Outliers are instances of the scaler hardware failures (above dotted line), and are removed from analysis.

For some scaler channels, where this approach did not completely remove fill-to-fill fluctuations (and no clear structure where the doubling of scaler rates could be identified), a slightly more complicated approach was taken. By using a Principle Component Analysis (PCA) [79], a decomposition of those rates into combinations of others was possible. By approximating a scaler rate seen in one channel based on combinations of other channels, the effect of stuck scaler rates was removed. The actual scaler rate was divided by the approximation, yielding a ratio approximately equal to unity. Outliers represented corrupt events and were removed as described a bove.

5.3.2 Pile-up

Due to high bunch crossing rates, it is easy to mistake vertices from past or future collisions with those from the triggered collision. The incorrect association of tracks to the triggered collision vertex, known as pile-up, has become a significant effect with collision rates in 2008 reaching as high as 300 kHz. Since many aspects of the analysis depend strongly on having the correct vertex position, it is vital that pile-up is understood, identified and removed.

The vertex finding algorithm implemented for Run 8 d+Au collisions (MinuitVF), found 10 vertices per minimum bias event in average. A statistical approach was taken in deciding which vertex within the event is the most probable, and tracks were associated with the vertex using a likelihood method, as explained in Chapter 4. Much work has been done to identify and remove pile-up in $d+$Au collisions [78], as presented in Chapter 6.

Chapter 6

Analysis

Minimum bias data from d+Au collisions at $\sqrt{s_{NN}} = 200$ GeV taken with the STAR detector at RHIC in 2008 were used in this analysis. A total of 40×10^6 minimum bias events were recorded at rates as high as 300 kHz.

In this chapter, first the vertex quality is discussed, and then the quality of the tracks associated with each event vertex is assessed. After that, an explaination of how J/Ψs were reconstructed and how background was removed is given. This selection process was optimised to reduce background while preserving statistics. Finally, the study of efficiency of the J/Ψ reconstruction process is presented.

6.1 Event Selection

6.1.1 Event Quality

The deuteron and gold nuclei collisions at $\sqrt{s_{NN}} = 200$ GeV result in a high energy system, in which the J/Ψ production cross section is large enough that large numbers of them are recorded by STAR in several months of running. These particles all originate from a common position where the collision took place, known as the vertex position. The beams are well focused in the transverse plane, but the collision diamond is extended in the z direction.

The number of reconstructed vertices per minimum bias $d+$Au collision is shown in Fig. 6.1, and the average number of vertices per event increases with increasing luminosity, as shown in Fig. 6.2. For each event, the vertices are ranked to determine the one that most probably triggered the detector readout. Only the vertex with the highest rank in each event, known as the primary vertex, was used in this analysis. Additionally, only the primary tracks associated to the primary vertex are used in this analysis. The vertex reconstruction and track association procedure is explained in detail in Chapter 4.

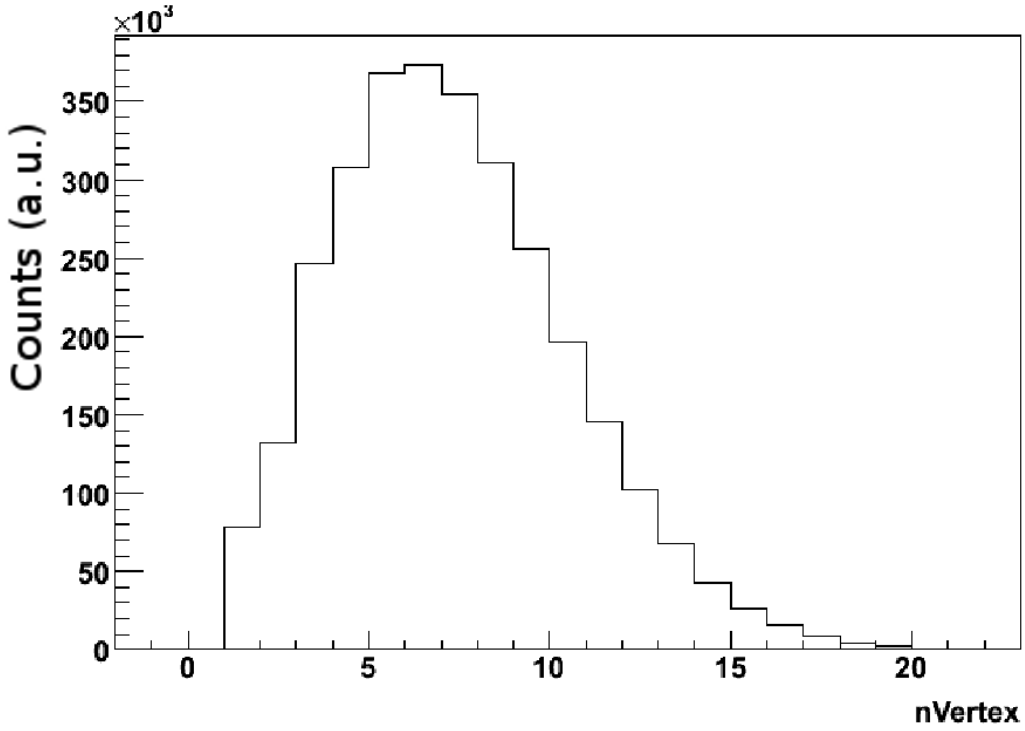

Figure 6.1: The number of reconstructed vertices in minimum-bias events in $d+$Au collisions at STAR.

In this analysis, the minimum bias trigger had to be satisfied by the particles

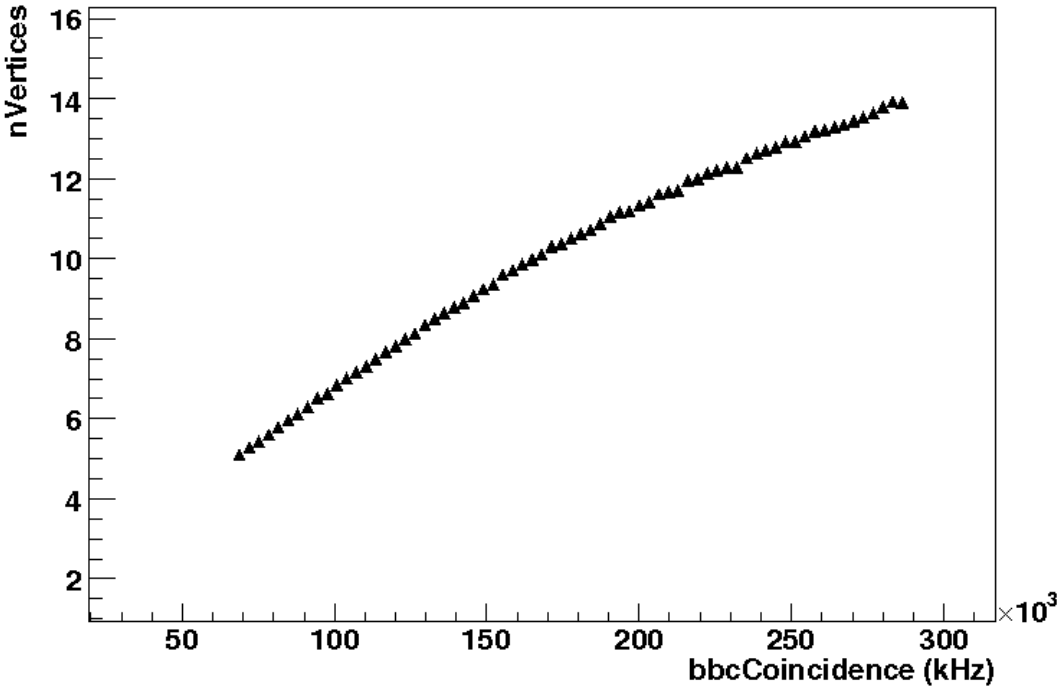

Figure 6.2: The average number of reconstructed vertices versus luminosity in minimum-bias events in $d+$Au collisions at STAR.

produced at chosen vertex. The vertex position along the beam axis, V_Z, is defined with the origin at the centre of the TPC. The minimum bias trigger places an online requirement on the time difference between the two VPD signals that corresponds to the window of $|V_Z| \leq 30$ cm. However, this detector was not used offline to reconstruct the final vertex position of the collision. Because of this, the offline vertex position can shift outside of ± 30 cm window. There is, however, a strong correlation between the vertex position determined from the VPD, and the reconstructed vertex position determined by MinuitVF. A distribution of the primary vertex position from Run 8 minimum bias events is shown in Fig. 6.3. The beams were focused to collide at the centre of the STAR detector, with the distribution peaking around $V_Z \approx 0$ and following a Gaussian shape within $|V_Z| \leq 30$, indicated by the Gaussian fit shown in

Fig. 6.3.

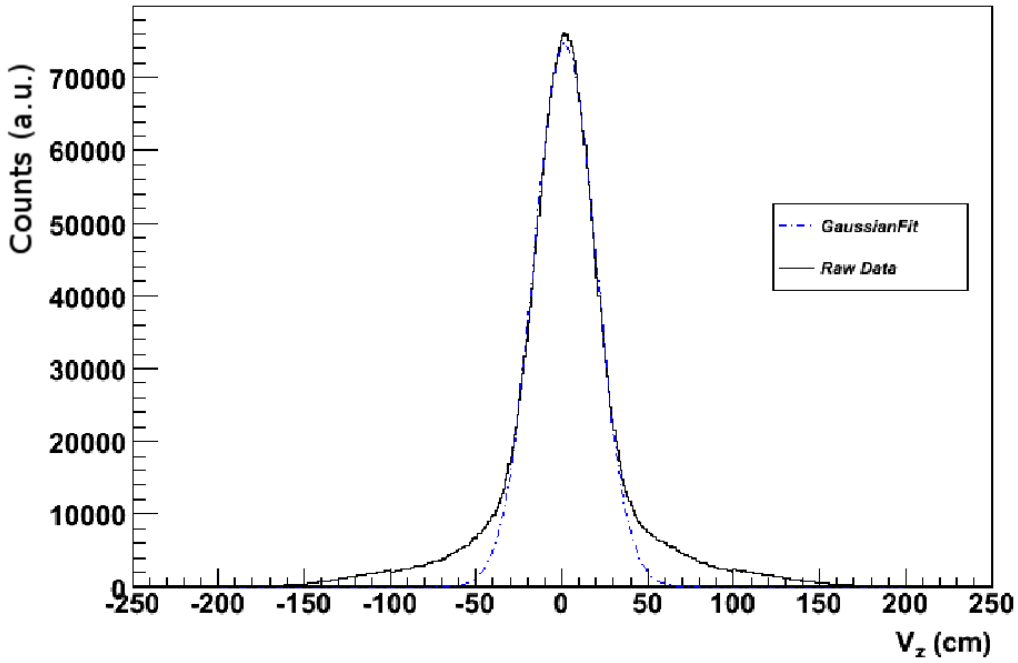

Figure 6.3: The Vertex Z distribution for minimum-bias events in $d+$Au collisions at STAR.

Minimum bias collisions were also required to have at least one neutron from the Au nucleus registered in the ZDC-E. For Run 8, simulations show that this is equivalent to requiring ZDC-E ADC value to be above 5 counts. A distribution of the ZDC-E signal for minimum bias events is shown in Fig. 6.4.

It was important to exclude vertices that satisfied the minimum bias trigger but were poorly reconstructed. The vertices were required to be reconstructed close to the centre of the TPC, because tracks with large $|V_Z|$ or large $|\eta|$ have a shorter length in the TPC and hence a lower reconstruction quality. These short tracks have fewer

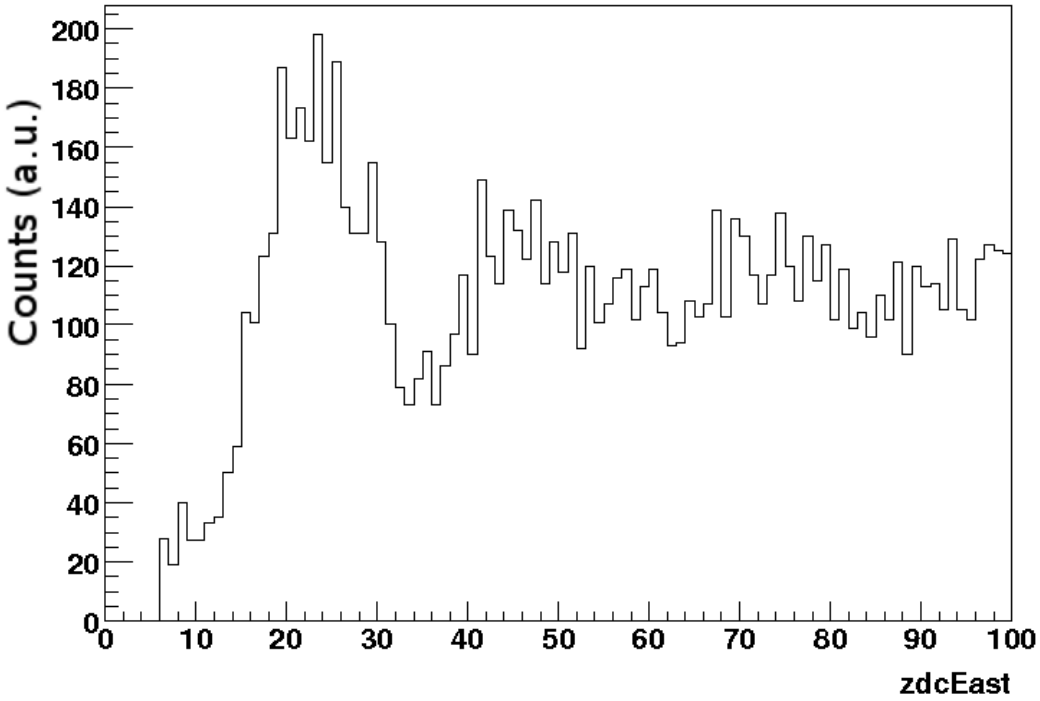

Figure 6.4: The East ZDC ADC distribution for minimum-bias collisions.

hit points in the TPC and have a lower reconstruction efficiency. A pseudorapidity distribution of tracks originated at various vertex positions is shown in Fig. 6.5, where the fall-off of statistics outside of $|\eta| > 1$ is due to the decrease of the TPC acceptance. A loss of particles is also observed close to $\eta = 0$ for tracks with large $|V_Z|$. The acceptance losses are also seen in the distribution of average multiplicity as a function of V_Z, as shown in Fig. 6.6. For vertices close to $V_Z \approx 0$, the mean multiplicity increases with increasing V_Z due to the asymmetry of the colliding d+Au system — more particles are produced in the direction of the Au nucleus, at $\eta < 0$, than in the direction of the deuteron. As a result, there are more short tracks, which pass through only a fraction of the TPC volume, with large $-|V_Z|$ than with large $+|V_Z|$. For large enough $|V_Z|$, the reconstruction efficiency drops off dramatically. To avoid these effects, a vertex position was required to fall within $|V_Z| < 40$ cm,

reducing the number of analysed minimum bias events to 34×10^6.

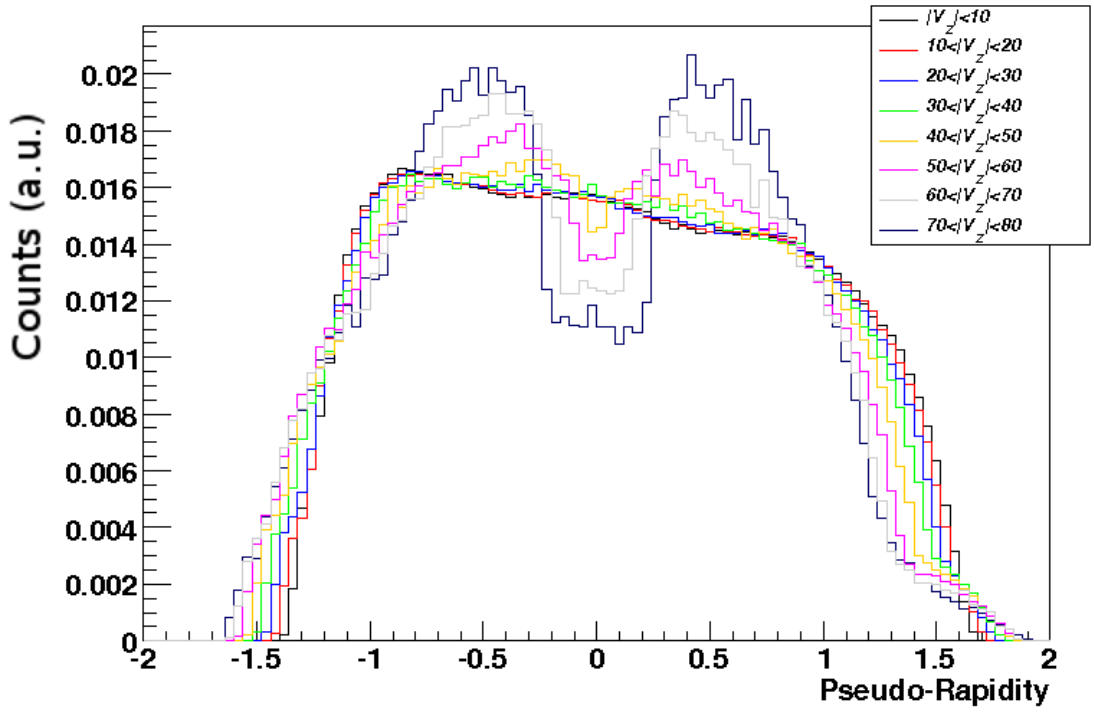

Figure 6.5: The pseudorapidity distribution for tracks with various vertex position. The TPC acceptance accounts for losses outside of $|\eta| > 1$. Within $|\eta| < 1$, losses in acceptance are seen around $\eta \approx 0$ for $|V_Z| > 40$ cm.

6.1.2 Vertex Pile-Up Removal

Since the effect of pile-up increases at higher luminosities, it is important to ensure that the charged particle multiplicity be stable with respect to the beam coincidence rate. The BEMC, which has much faster readout rates than the TPC, was used to remove pile-up vertices.

For each vertex reconstructed in the TPC in an event, the associated primary

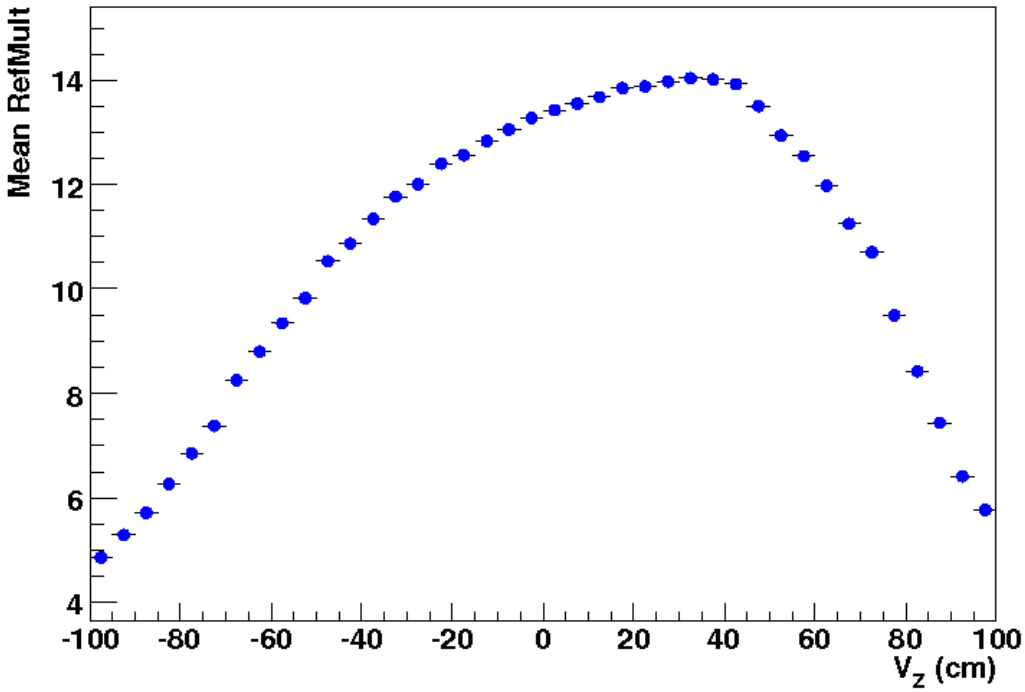

Figure 6.6: The mean multiplicity of events versus vertex position. Outside of $|V_Z| = 40$, the TPC reconstruction efficiency drops off significantly.

tracks[1] were projected to the BEMC. The number of tracks matched to the BEMC, N_{BEMC}, is the number of these tracks that project to a tower in the BEMC that was fired in the event. The mean number of such matches per event is stable across the range of coincidence rate, as shown in Fig. 6.7. In the absence of the track-tower matches, $N_{\mathrm{BEMC}} = 0$ (left panel of Fig. 6.8), there is no correlation between the reconstructed vertex position and VPD vertex position, meaning that these vertices are highly contaminated with pile-up. Requiring at least one match, $N_{\mathrm{BEMC}} > 0$ (right panel of Fig. 6.8), reduces the statistics by 4% but reveals a strong correlation between the distribution of the VPD time difference and the reconstructed vertex

[1]Tracks with DCA $<$ 3cm to the vertex and $|\eta| < 0.5$.

position [2]. A stronger requirement of $N_{\mathrm{BEMC}} > 1$ (right panel of Fig. 6.9) reduces statistics by an additional 3% without improving pile-up removal.

The cuts placed event-wise on the primary vertex are summarized in Table 6.1, and a distribution of the charged track multiplicity of the events passing the event selection criteria are shown in Fig. 6.10.

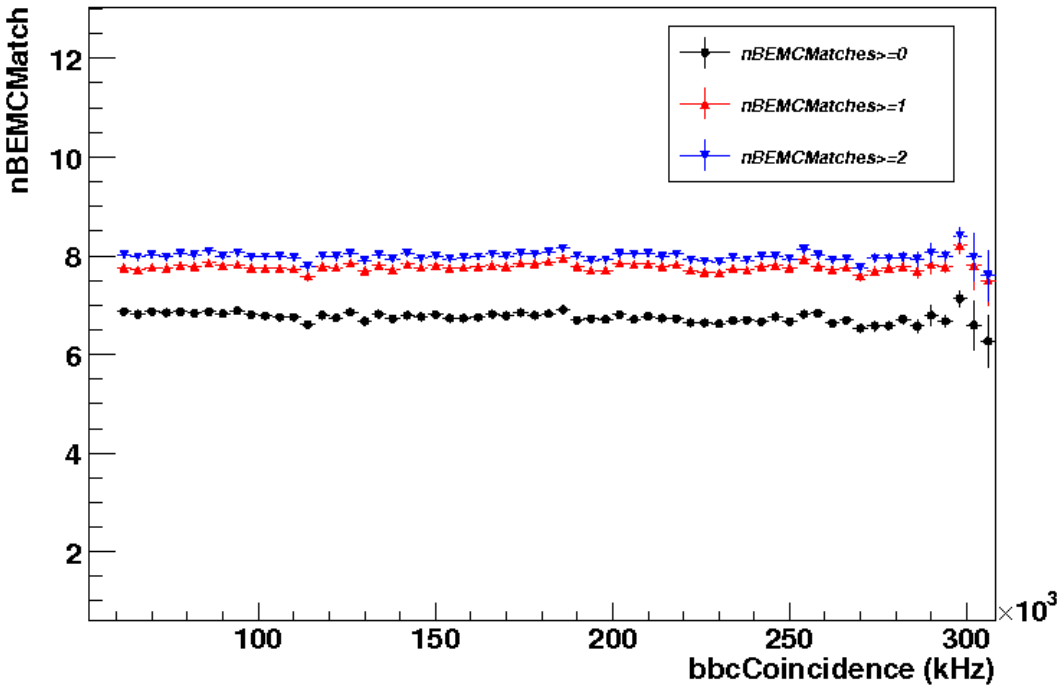

Figure 6.7: The mean number of tracks matched to the BEMC versus beam luminosity. In black, no requirement is placed on N_{BEMC}. In red, we require $N_{\mathrm{BEMC}} \geq 1$, which has a higher mean value due to the improved rejection of pile-up vertices. This does not improve when requiring $N_{\mathrm{BEMC}} \geq 2$, shown in blue.

With these cuts in place, the majority of pile-up events and events with low reconstruction quality were removed. A similar exercises was performed to remove

[2]The VPD position is determined from the time difference in the signal received from the East ($V_Z < 0$) detector to the West ($V_Z > 0$) detector. Because of this, a negative correlation is observed.

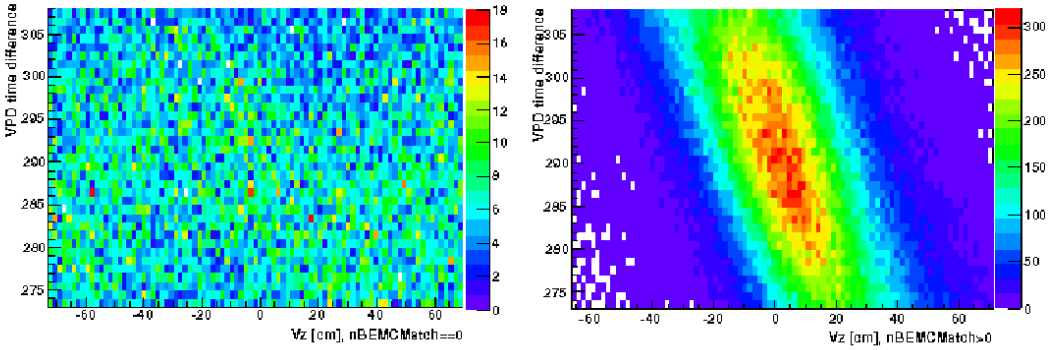

Figure 6.8: The time difference in the VPD is plotted against the reconstructed primary vertex position along the beam axis. On the left, vertices with no tracks matched to the BEMC are shown. On the right, vertices are required to have at least one track match to the BEMC. Clearly vertices with $N_{\mathrm{BEMC}} = 0$ (left) are largely uncorrelated with the collision triggering the event.

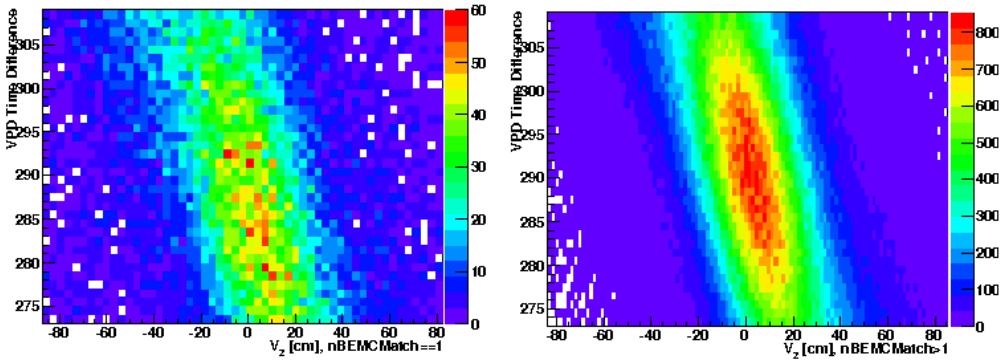

Figure 6.9: The time difference in the VPD is plotted against the reconstructed primary vertex position along the beam axis. On the left, vertices are required to have at least two tracks matched to the BEMC. On the right, vertices with one track matched to the BEMC are shown. Vertices with $N_{\mathrm{BEMC}} = 1$ are correlated with the VPD, and requiring $N_{\mathrm{BEMC}} > 1$ is not necessary.

poorly reconstructed tracks from the analysis.

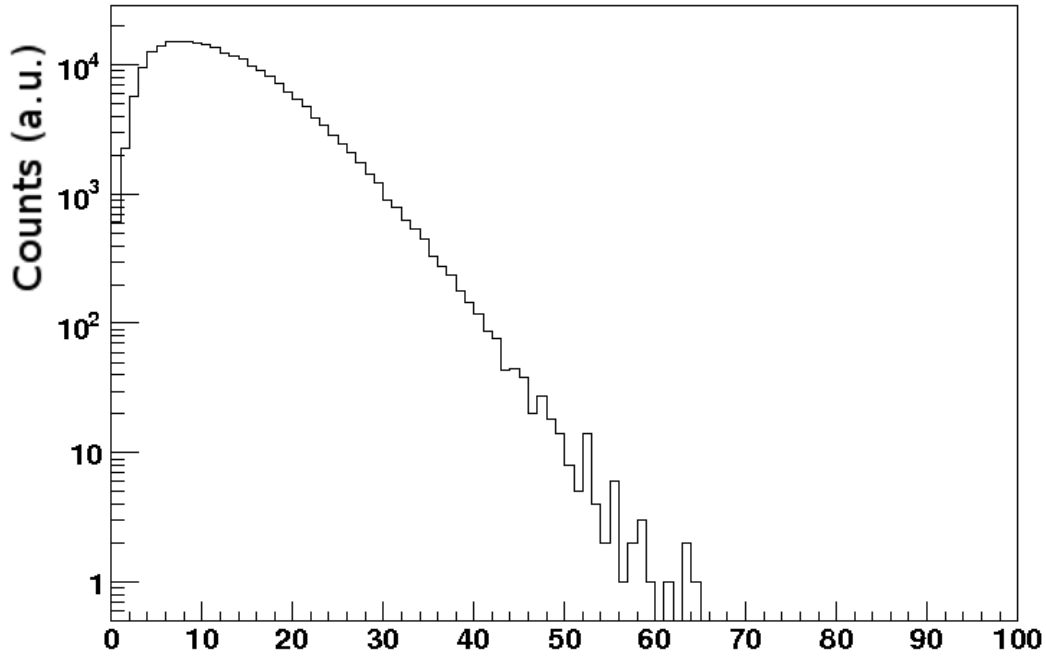

Figure 6.10: A charged track multiplicity distribution for selected events in run8 $d+$Au.

Table 6.1: Event Quality Cuts

$\lvert V_Z \rvert$	$<$	40 cm
N_{BEMC}	$>$	0

6.2 Track Selection

Because J/Ψ is a heavy particle, with a short lifetime of $\tau = 7.2 \times 10^{-21}$ s and a decay length of $c\tau = 2.2 \times 10^{-12}$ m, which is much smaller than the TPC tracking resolution at the vertex, J/Ψs are assumed to decay at the vertex position. Therefore, only tracks that project back to the primary vertex, known as primary tracks, were used in this analysis. This section presents cuts that remove poorly reconstructed

tracks.

The helix fitted to the reconstructed points in the TPC was used to obtain track information (e.g. momentum, rapidity, etc.). For primary tracks, this helix was forced to run through the vertex position and refitted, as described in Chapter 4.

6.2.1 Track Quality

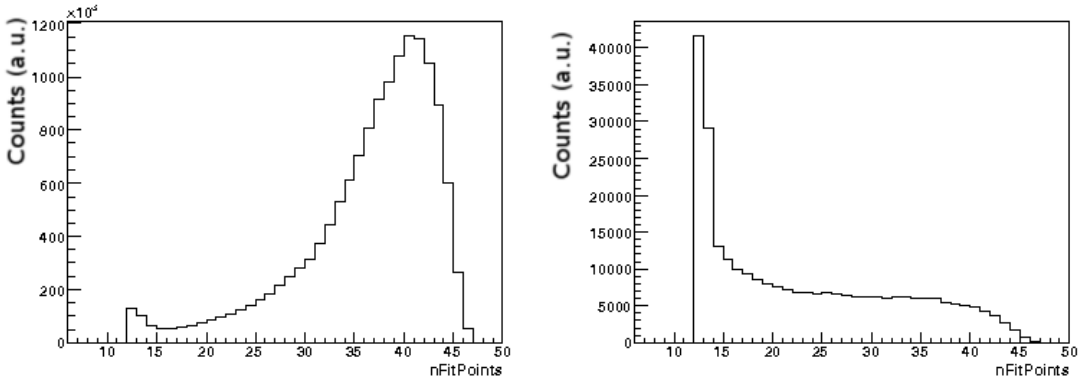

Figure 6.11: Left: The number of fit points used in track reconstruction for tracks passing event cuts and $|\eta| < 1$. Right: The number of fit points for tracks with of $|V_Z| > 40$ and $|\eta| > 1$.

As was explained in section 6.1.1, due to edge effects of the TPC and a large acceptance window in V_Z, there are substantial losses in the track reconstruction efficiency at $|\eta| > 1$. To obtain a stable performance of the TPC, the tracks were required to have a pseudorapidity $|\eta| < 1$ (see the right panel of Fig. 6.5).

The track reconstruction quality depends on the number of hits points in the TPC, nHits, that were used to reconstruct the particle trajectory. The maximum possible number of hits in the TPC sectors is 45, and a distribution of the number of hit points for tracks with with $|\eta| < 1$ within $|V_Z| < 40$cm is shown on the left panel of Fig. 6.11. The right panel of Fig. 6.11 shows the number of hit points for tracks

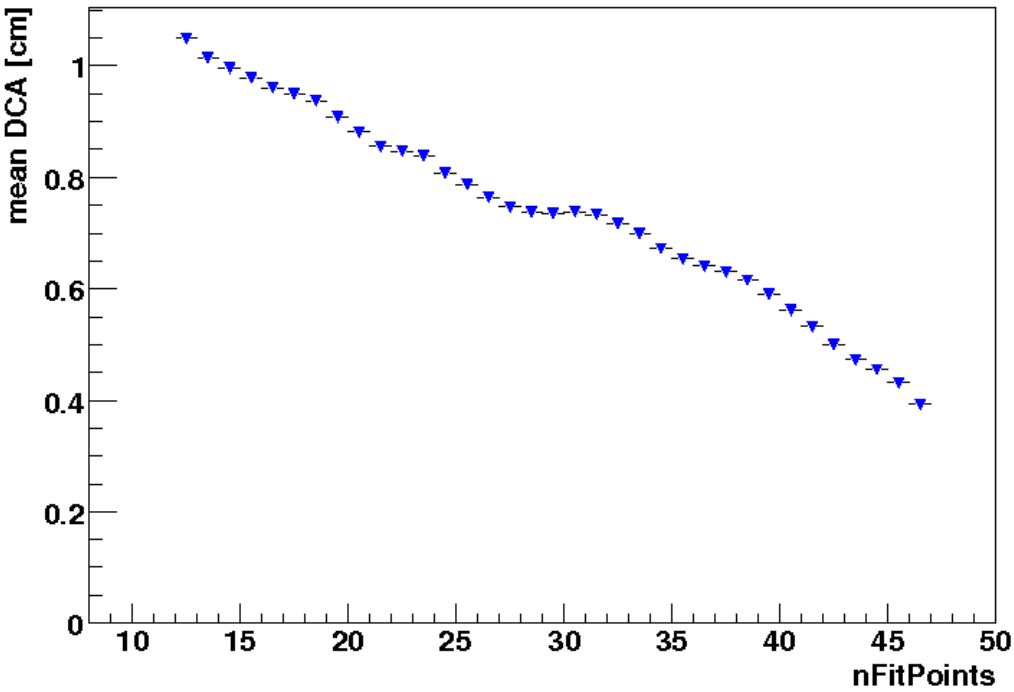

Figure 6.12: The mean DCA to the vertex position of tracks with different numbers of fit points in the TPC. Tracks with a low number of fit points have a poor reconstruction quality, and hence a wider DCA distribution.

with $|V_Z| > 40$cm and $|\eta| > 1$, and it is seen that these tracks have fewer hits in the TPC. Figure 6.12 shows the lower quality of tracks with small nHits, seen as a wider distribution of DCA to the vertex position.

The TPC tracking efficiency drops across the sector boundaries, and particles that cross the sector boundaries may be reconstructed as two separate tracks, known as split tracks. This can cause double counting and distort $\mathrm{d}E/\mathrm{d}x$ measurements. These short tracks, which intrinsically have a low nHits, have a large uncertainty in the fitting and extrapolation to the vertex. Since the maximum possible number of hits depends on the geometry of the TPC relative to the trajectory of the particle,

the ratio of actual hit points used to the maximum possible number of hits for each track was required to be greater than 0.52. This removed short and split tracks. in addition, a number of hit points was required to be greater than 20, which removed tracks that passed through dead regions of the TPC.

Each reconstructed track was assigned a flag of the form $flag = \pm zxyy$, where x, y, and z are single digits. A negative value indicated a bad Minuit fit, and these tracks were excluded from the analysis. The value of x refers to the detector used to reconstruct the track, and requiring $|\eta| < 1$ ensured that the detector was the TPC. The digits yy provided information on the track fitting, and z was zero for all tracks except Post-Crossing Tracks (PCTs), which had a value of $z = 1$. PCTs are discussed in the section below.

With a magnetic field strength of $B = 0.5$ T, only particles with $p_T > 100$ MeV can reach the TPC. A p_T distribution for tracks that passed the selection criteria is shown in Fig. 6.13. For low-p_T tracks, a bump in the pseudorapidity distribution at $\eta \approx 0$ was observed, as seen in Fig. 6.14, where the pseudorapidity distribution for multiple p_T bins is shown. The bump close to $\eta = 0$ for low-p_T tracks is not currently understood, but did not affect this analysis because tracks were required to have $p_T > 150$ MeV/c.

6.2.2 Track Pile-Up Removal

Pile-up vertices have been removed by requiring at least one track from the reconstructed primary vertex is matched to the BEMC, as described in the previous section. There were, however, a significant number of tracks from pile-up vertices (pile-up tracks) that were incorrectly assigned to the primary vertex. The average time between minimum bias collisions decreases at higher luminosities, worsening the ability of the TPC to distinguish between tracks from nearby pile-up vertices and tracks from the triggered collision. This is illustrated in Fig. 6.15, which shows the multiplicity of recorded events versus beam luminosity. The mean multiplicity of tracks that pass the

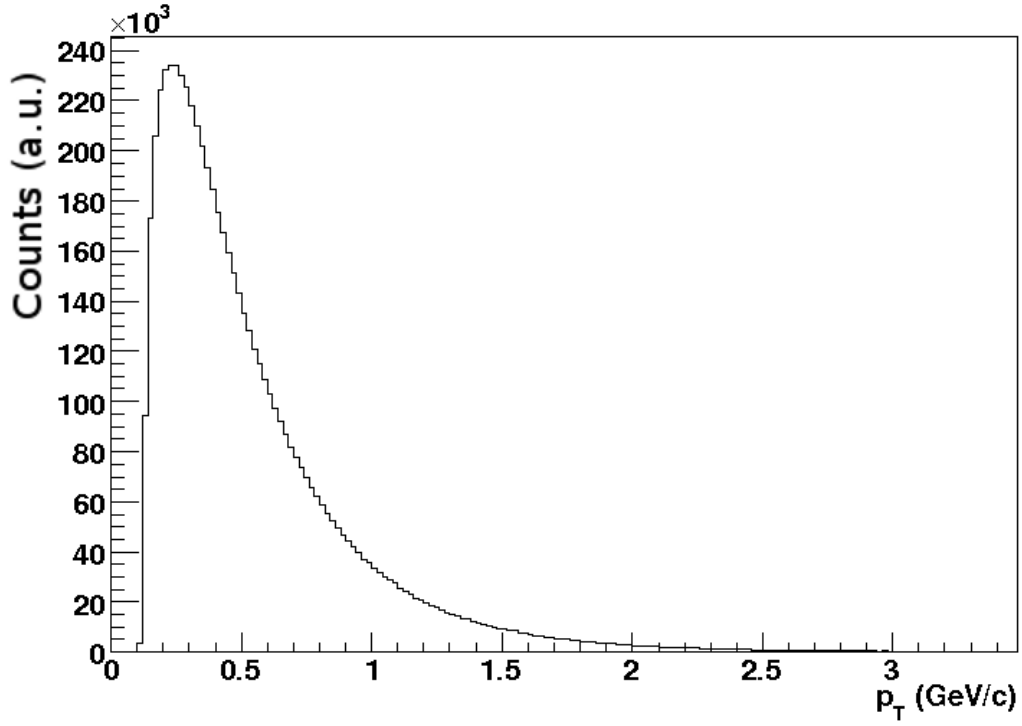

Figure 6.13: The p_T distribution of tracks that pass the event selection criteria within $|\eta| < 1$.

vertex and track cuts in Table 6.1 (blue) steadily increases with increasing luminosity, indicating a significant pile-up contribution to the reconstructed primary vertices.

One class of pile-up tracks, known as Post-Crossing Tracks (PCTs), were easy to identify and remove. These tracks crossed the central membrane of the TPC after the event was triggered, and so clearly belong to another vertex. While there is no ability to store information on Pre-Crossing Tracks due to the architecture of the vertex reconstruction algorithm (these are removed in production), Post-Crossing Tracks have been included in the vertex reconstruction and tracks association procedure. In order to identify and remove these tracks, they have been flagged during production with $flag > 1000$. These tracks accounted for $\approx 2\%$ of all tracks, and have been removed.

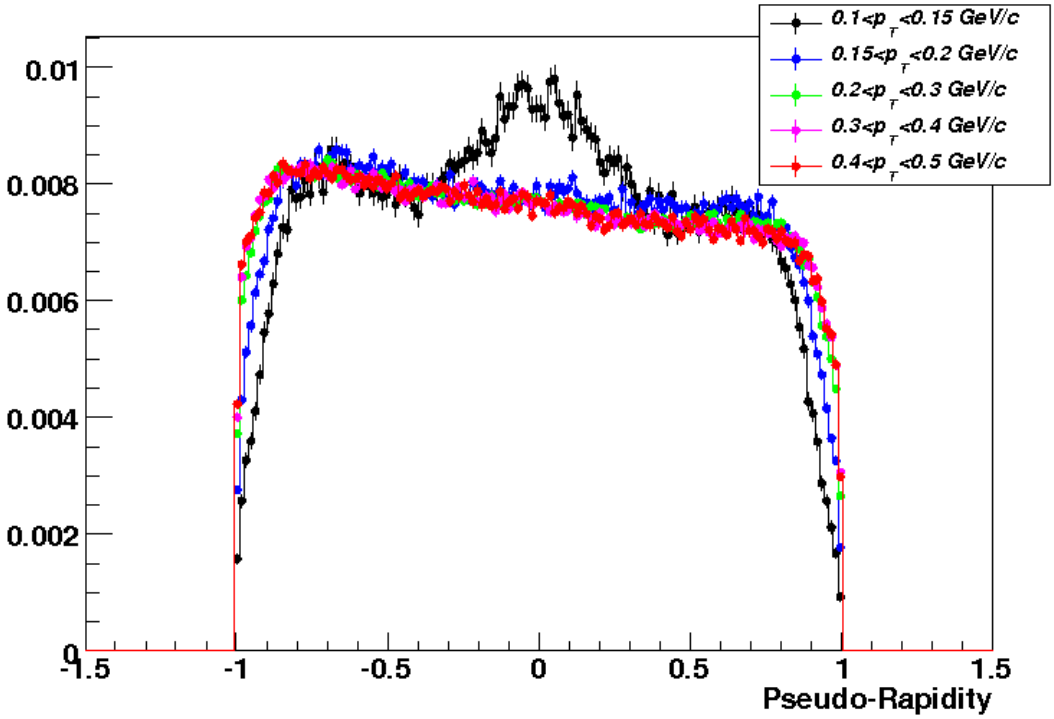

Figure 6.14: The pseudorapidity distribution versus p_T of tracks. There is a bump around $\eta \approx 0$ which is removed with a cut of $p_T > 150$ MeV/c.

The resulting multiplicity versus luminosity is also shown in Fig. 6.15 (green). The slope has decreased but is still not constant with luminosity, indicating that not all of the pile-up has been removed.

Primary tracks were reconstructed with the constraint that they pass through the reconstructed vertex position. Since pile-up tracks do not belong to the reconstructed vertex, the χ^2 of the fit to their hit points was larger than that of tracks belonging to the collision. The maximum allowed χ^2 of tracks has been varied to achieve a stable mean multiplicity. Figure 6.15 shows the mean multiplicity versus luminosity for tracks with $\chi^2 < 6$ (red). This cut alone results in a constant multiplicity per event across a wide range of luminosities, while decreasing the multiplicity by $\approx 27\%$.

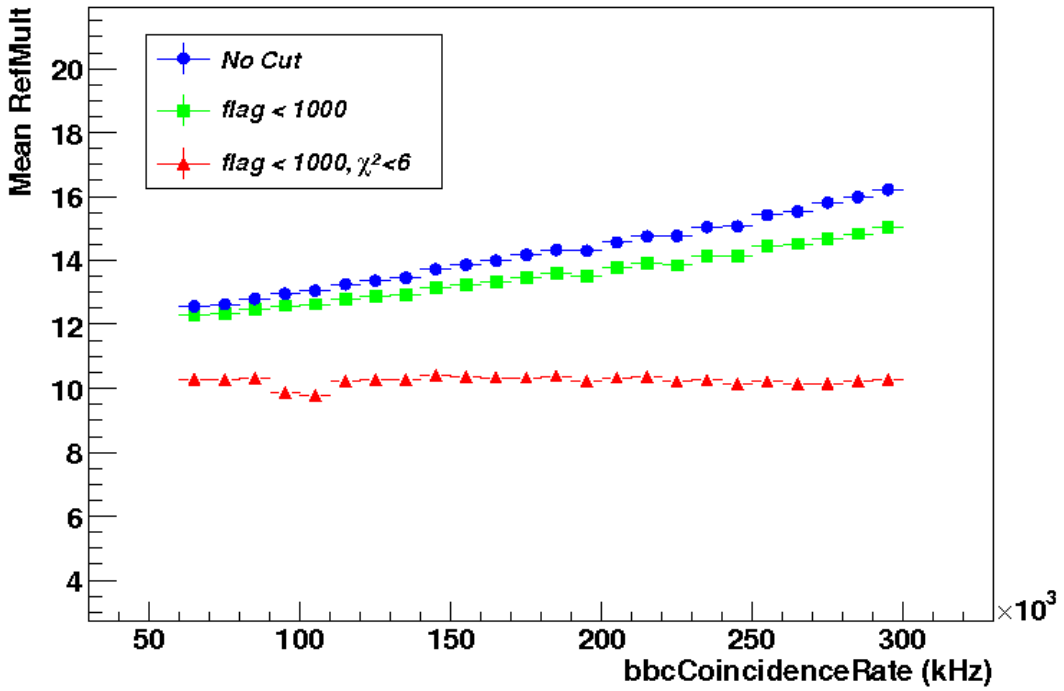

Figure 6.15: The mean multiplicity of events versus beam luminosity. In blue, pile-up causes an increase of the mean multiplicity as luminosity increases. In green, Post-Crossing tracks are removed, decreasing the pile-up effect. By requiring that the tracks have a $\chi^2 < 6$, the pile-up effect is eliminated, shown in red.

The combination of all these cuts effectively removes pile-up and ensures a high track quality.

All track cuts presented above are listed below in Table 6.2.

6.2.3 Centrality Determination

The centrality of a collision is defined as the degree of overlap of the colliding nuclei, as discussed in Chapter 1. To avoid correlations in the measured multiplicity distribution, which may bias the centrality selection, the centrality classes for events

Table 6.2: Track Quality Cuts

$\|\eta\|$	$<$	1
nHits	$>$	20
nHits/nPoss	$>$	0.52
DCA	$<$	3 cm
p_T	$>$	0.15 GeV/c
$flag$	$>$	0
$flag$	$<$	1000
χ^2	$<$	6

were defined in the multiplicity observed in the East Forward TPC (FTPC-E), which covered a pseudorapidity range of $-3.8 < \eta < -2.8$ and full azimuth. Only the East FTPC was used due to the asymmetry of the collision system.

A multiplicity distribution simulated using the d + Au collision geometry and Glauber calculations, shown in Fig. 6.16 (red), was fitted to the measured FTPC-E multiplicity distribution (black). While the two distributions agreed for multiplicities larger than 15, there were large discrepancies for lower multiplicity events due to the inefficiency of the VPD in peripheral collisions. The vertical lines in Fig. 6.16 indicate the cuts for 0%–20% and 20%–40% central collisions, and the corresponding mean values of $N_{\rm part}$ were obtained for each centrality class using the Glauber calculations. Since the simulation and data only agreed for 0%–20% central collisions, only results from the most central collisions are presented in this analysis. A total of 11×10^6 of 0%–20% central events have been recorded by STAR and used in this analysis.

For 0%–20% central d + Au collisions, the mean number of participants was $\langle N_{\rm part} \rangle = 15.2 \pm 1.9$ and the mean number of binary collisions was $\langle N_{\rm coll} \rangle = 14.6 \pm 1.7$, where the uncertainty is dominated by systematics due to assumptions of the collision geometry and Glauber calculations. This corresponds to a multiplicity in the FTPC-E above ≈ 11. Due to instabilities in the FTPC-E multiplicity, the minimal multiplicity used to select central events was varied between 10 and 12 across the

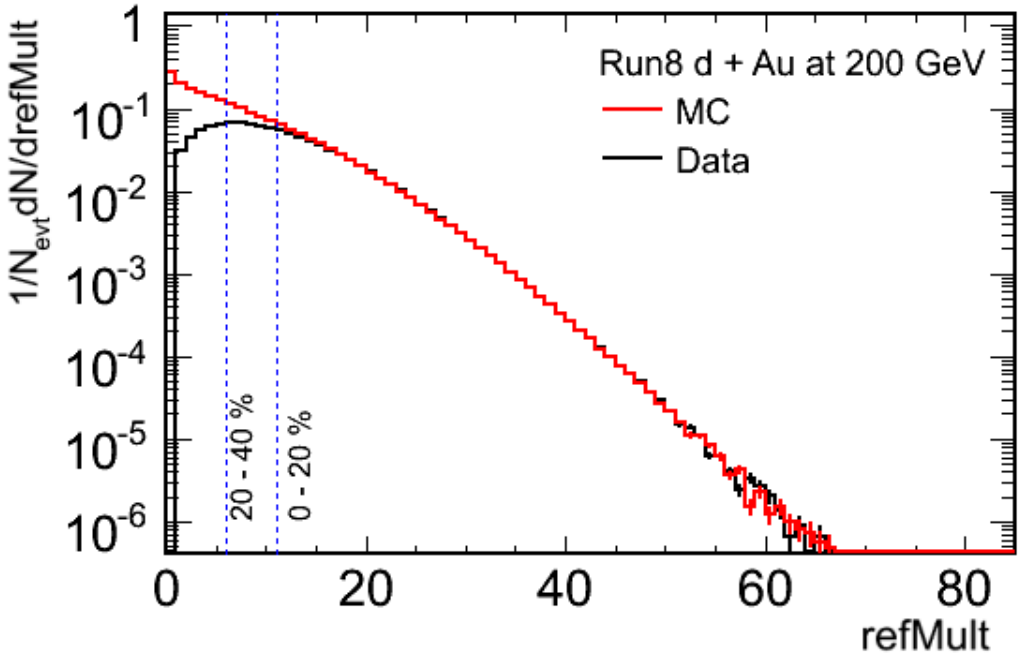

Figure 6.16: Black: The multiplicity distribution in the East FTPC. Red: The simulated multiplicity distribution using Monte Carlo Glauber calculations.

time period of the run.

6.3 Electron Identification

After a high level of event and track quality have been achieved, cuts were placed on kinematic variables of tracks, in order to identify electrons with the highest purity (low background) and lowest rejection rate possible. Careful optimisation of the electron identification (eID) cuts was necessary to satisfy these two opposing requirements.

The detectors used for electron identification were the TPC and the BEMC. From the reconstructed particle kinematics in the TPC, the track $\mathrm{d}E/\mathrm{d}x$ and momentum

were used to identify electrons with a high efficiency. The energy deposited in the BEMC further improved the ability to discriminate between electrons and hadrons.

6.3.1 J/Ψ Reconstruction and Background Estimation

This section presents the method for identifying electrons, combining electron pairs into possible J/Ψ candidates, estimating the amount of background, and quantifying the quality of the J/Ψ signal. The invariant yield and the nuclear modification factor are also introduced.

The amount of energy lost by particles while traversing the P10 gas in the TPC volume is calculated using the Bethe-Bloch equation, as illustrated in Fig. 4.8. It is useful to transform the measured $\mathrm{d}E/\mathrm{d}x$ of particles into a likelihood probability that tracks were produced by electrons, by weighting them with the energy loss predicted by the Bethe-Bloch equation. This likelihood, $n\sigma_e$, is calculated as

$$n\sigma_e = \log\left(\frac{\mathrm{d}E/\mathrm{d}x|_{\mathrm{measured}}}{\mathrm{d}E/\mathrm{d}x|_{\mathrm{Bethe-Bloch}}}\right)/\sigma, \tag{6.1}$$

where σ is the error associated with the $\mathrm{d}E/\mathrm{d}x$ measurement. With exact calibration, electrons have a Gaussian distribution in $n\sigma_e$ space with zero mean and a unit standard deviation. Electron identification in the TPC relies on accepting tracks that have a $\mathrm{d}E/\mathrm{d}x$ value close to that predicted for electrons, while being distinct from the expected proton, pion, and kaon $\mathrm{d}E/\mathrm{d}x$ values. A distribution of $n\sigma_e$ for several momentum bins is shown in Fig. 6.17, and a multiple Gaussian fit to the data was performed to determine the hadronic contributions. A fit of the deuteron contribution, which can be seen in the lower momentum bins for $n\sigma_e > 3$, was not performed as this would introduce further uncertainty in the fitting process.

The set of TPC cuts, shown in Table 6.3, was used for initial electron identification. The cut of $p_T > 1$ GeV/c was motivated by the large hadron contamination due to the $\mathrm{d}E/\mathrm{d}x$ band crossing for pions, kaons, and protons with electrons, see Fig. 4.8. Requiring $|n\sigma_e| < 3.0$ rejected less than 0.1% of electrons, while requiring $|n\sigma| > 2.5$

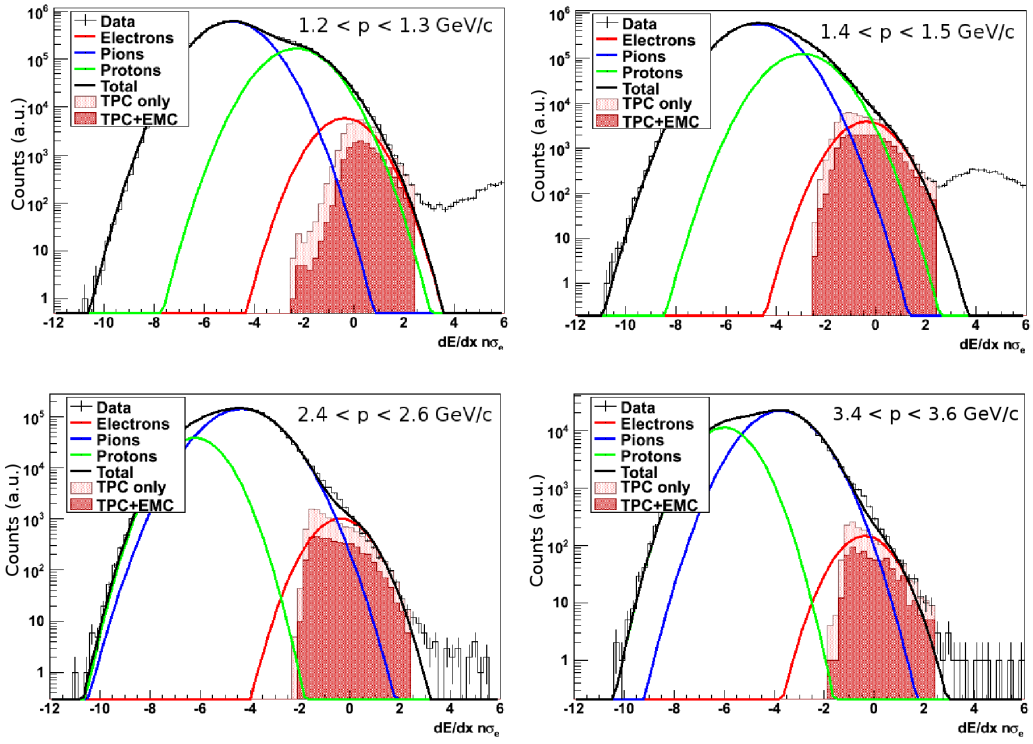

Figure 6.17: $n\sigma_e$ for particles passing vertex and track cuts, projected into several momentum bins. The shaded region indicates tracks accepted as electrons.

for p, K, and π, rejected $\approx 96\%$ of possible hadron contamination. These cuts were modified to optimise the electron acceptance vs hadron rejection.

Table 6.3: TPC Electron Identification Cuts

p_T	$>$	1.0 GeV/c
$\lvert n\sigma_e \rvert$	$<$	3.0
$\lvert n\sigma_p \rvert$	$\geq$	2.5
$\lvert n\sigma_\pi \rvert$	$\geq$	2.5
$\lvert n\sigma_K \rvert$	$\geq$	2.5

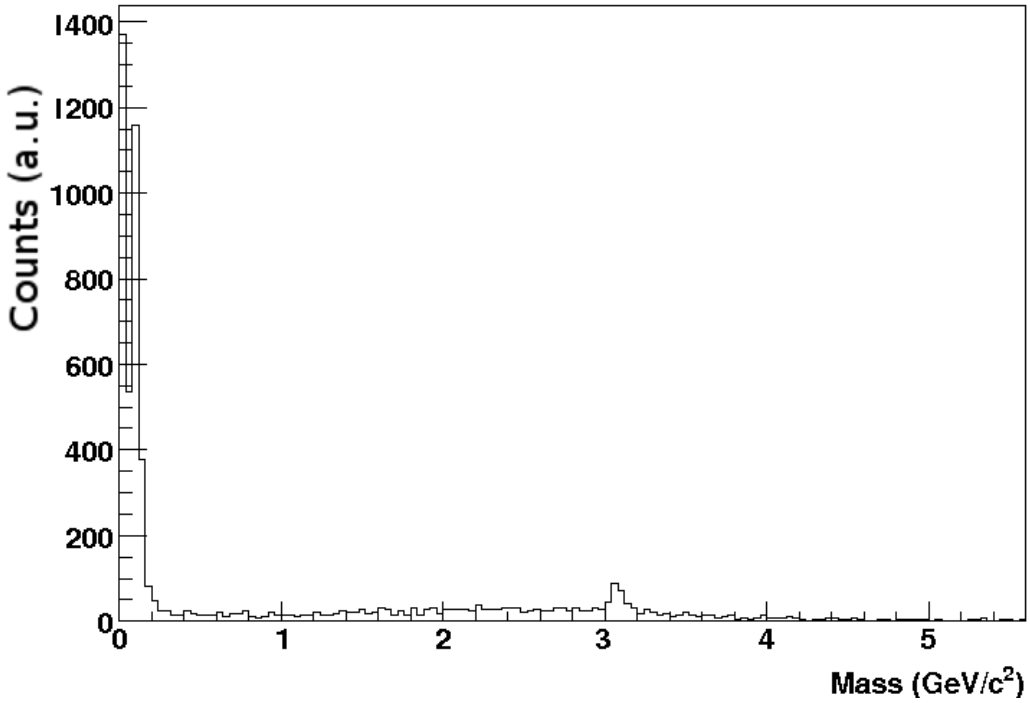

Figure 6.18: The invariant mass spectrum for e^+e^- pairs. The peak around $m = 0$ is due to photonic conversions.

After electrons have been identified, J/Ψ candidates were formed as all possible electron pairs in an event. For a J/Ψ with energy E and momentum $\vec{p}$, decaying into daughter electrons with energies E_1 and E_2 and momenta $\vec{p}_1$ and $\vec{p}_2$, the energy and momentum conservation laws give

$$\vec{p} = \vec{p}_1 + \vec{p}_2, \tag{6.2}$$

$$E = E_1 + E_2, \tag{6.3}$$

where the energy of a particle with momentum $\vec{p}$ and mass m is given as

$$E = \sqrt{|\vec{p}|^2 + m^2}. \tag{6.4}$$

Since the electrons were required to have $p_T > 1$ GeV/c, they were highly relativistic ($m/|\vec{p}| < 0.5 \times 10^{-3}$). In this kinematic regime, electrons can be considered massless.

Using the approximation $E \approx p$, the conservation laws can be used to obtain an expression for the invariant mass of the parent J/Ψ,

$$m = 2\,|\vec{p}_1|\,|\vec{p}_2|\,(1 - \cos\theta)\,, \tag{6.5}$$

where θ is the opening angle between the daughter electrons. Since it is not possible to know *a priori* which e^+e^- pairs came from a J/Ψ decay, all possible e^+e^- pairs event-wise were considered. There is a large number of pairs with low masses in the dielectron mass spectrum due to photon conversions, as shown in Fig. 6.18. To remove this contribution, the reconstructed e^+e^- mass was required to be above 200 MeV. Figure 6.19 shows the invariant mass spectrum for opposite-sign electron pairs (black) that passed the cuts listed in Tables 6.1, 6.2, and 6.3, and the peak around the true mass of the J/Ψ is visible even before background subtraction.

Taking all possible combinations of electrons and positrons as J/Ψ candidates introduced a combinatorial background in the invariant mass distribution. This background was estimated and removed using a like-sign background subtraction technique. Using this method, the number of background J/Ψ candidates was estimated by looking at the invariant mass distributions of all possible e^+e^+ and e^-e^- pairs. The the signal, S, and background, B, were calculated as

$$B = N^{++} + N^{--}, \tag{6.6}$$

$$S = N^{+-} - B, \tag{6.7}$$

where N_{+-}, N_{++}, and N_{--} are the numbers of e^+e^-, e^+e^+, and e^-e^- pairs, respectively. The background was calculated as an arithmetic mean of the numbers of like-sign pairs, which is equivalent to using the geometric mean, but reduces fluctuations in the background caused by low statistics. The background calculated from electrons identified using the cuts listed in Table 6.3 is shown in Fig. 6.19 (red). The background subtracted e^+e^- invariant mass spectrum is shown in Fig. 6.20, and a J/Ψ signal is evident at $m \approx 3$ GeV/c^2. There are large fluctuations in the low mass region left after the background subtraction. A Gaussian is fitted to the signal, and

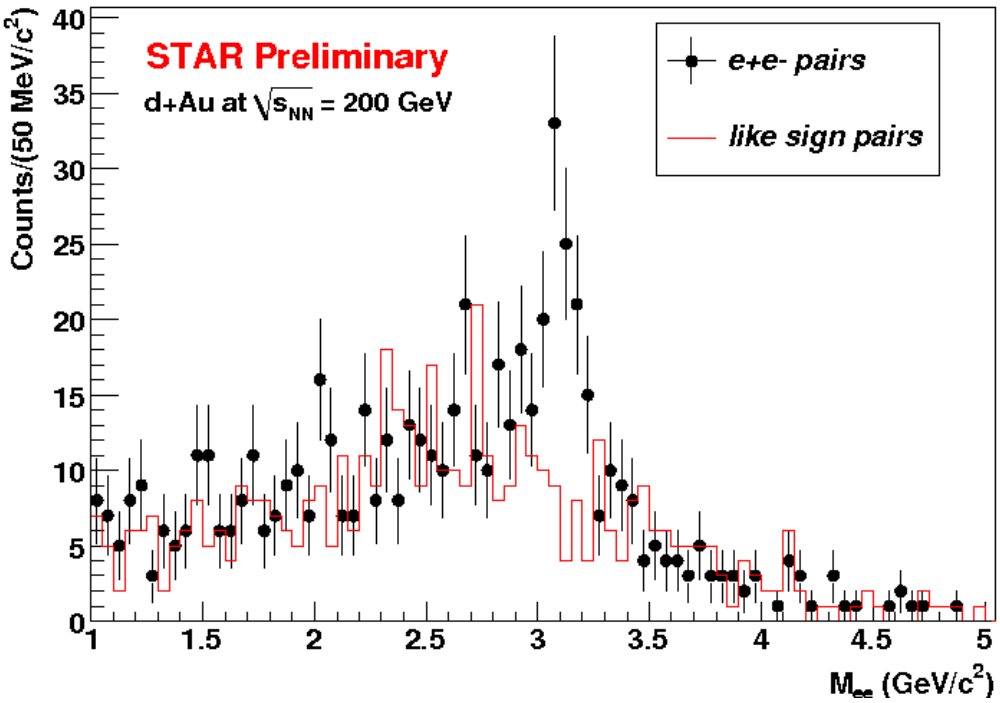

Figure 6.19: The invariant mass spectrum for e^+e^- pairs (black), and like-sign background (red).

while the J/Ψ peak is not expected to have a Gaussian shape (bremsstrahlung causes a tail in the peak towards lower masses), this provides an approximate mean and width of the J/Ψ peak. The fitted mean, $m = 3.085 \pm 0.012$ GeV/c^2, was found to be consistent with the PDG value $m_{\mathrm{J}/\Psi} = 3.096$ GeV/c^2 [34]. The J/Ψ yield was calculated by summing the background subtracted distribution within 3 standard deviations from the mean, $2.9 \leq m \leq 3.3$ GeV/c^2.

The quality of the J/Ψ signal depends on the number of counts and the amount of background in the mass window of the J/Ψ, and can be characterised by the signal to background ratio, S/B, and the significance, Sig, of the J/Ψ signal,

$$Sig = S/\delta S, \tag{6.8}$$

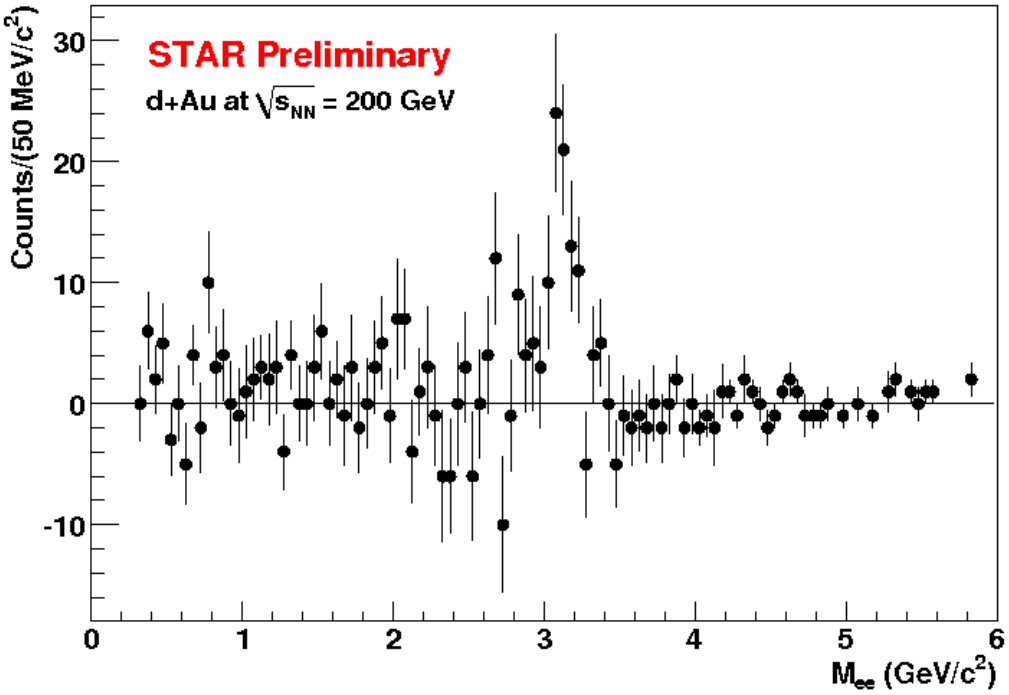

Figure 6.20: The invariant mass spectrum for e^+e^- pairs after like-sign background subtraction.

where the variance in the signal δS is calculated using a Taylor expansion

$$
\begin{aligned}
|\delta S\,(N_i)|^2 &= \sum_i \left|\frac{\partial S}{\partial N_i}\delta N_i\right|^2 + \mathcal{O}\left(\delta N^2\right)^2 && (6.9)\\
&= \sum_i |\delta N_i|^2 && (6.10)\\
&= \sum_i N_i && (6.11)\\
&= N_{+-} + N_{++} + N_{--} && (6.12)\\
&= S + 2B. && (6.13)
\end{aligned}
$$

The signal and background were counted in the mass range $2.8 \leq m \leq 3.2$ GeV/c^2. The electron identification cuts rely on maximizing these quantities.

After the background was subtracted from the e^+e^- invariant mass spectrum, the uncorrected raw yield, $N_{\mathrm{J}/\Psi}^{\mathrm{Uncorr}}$ was calculated by counting the number of reconstructed e^+e^- pairs in the J/Ψ mass region. From this, the yield was corrected and the invariant yield was determined using Eq. (1.31). The J/Ψ mass spectrum and yield are presented in Chapter 7.

6.3.2 Electron Identification Cuts

As mentioned previously, the loss in statistics when removing pile-up vertices with the cut $N_{\mathrm{BEMC}} > 0$ was $\approx 4\%$, which is not significant. Similarly, removing PCTs with the cut flag < 1000 reduced statistics by only 2%. However, removing pile-up tracks with the cut $\chi^2 < 6$ decreased statistics by $\approx 27\%$. While the cut on χ^2 did yield a stable multiplicity with respect to luminosity, it was a brute-force approach to remove pile-up and may have unnecessarily limited statistics for studies involving rare particles. This cut decreased the number of reconstructed J/Ψs by a factor of 2, which is significant given the limited statistics available. Because of the small J/Ψ production cross section, it is unlikely that electrons associated to the decay of a J/Ψ will be affected by pile-up. Also, due to the fast readout rates of the BEMC, this detector was not affected by pile-up. Because of this, requiring that all electrons are matched to a fired tower in the BEMC should have already removed any pile-up from this analysis.

Electrons have been identified using the quality cuts in Table 6.2 (without pile-up removal cuts) and the eID cuts on p_T and $\mathrm{d}E/\mathrm{d}x$ listed in Table 6.3. The average number of electrons is stable with respect to luminosity, see left panel of Fig. 6.21. The electrons have also been required to be matched to a fired tower in the BEMC, and the average multiplicity for these electrons, shown in the right panel of Fig. 6.21, is also stable with respect to luminosity. This indicates that electrons used in this analysis are absent of pile-up effects.

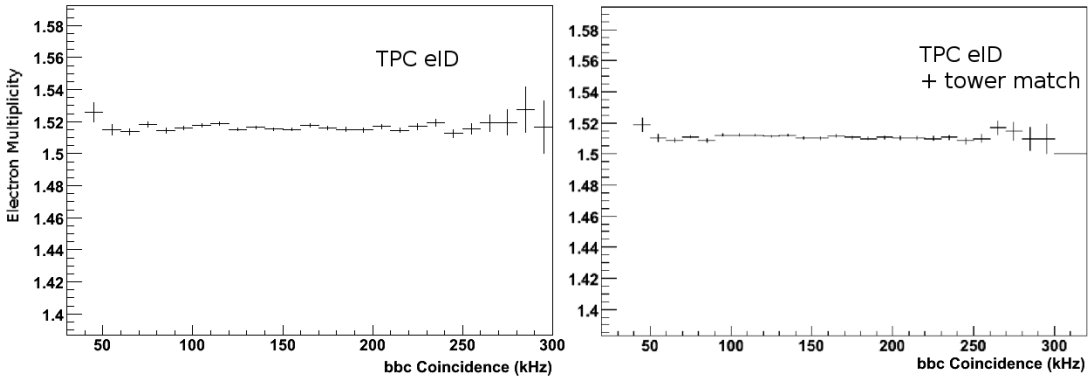

Figure 6.21: The average multiplicity for electrons. Electrons identified with the TPC (left), and matched to the BEMC (right) versus luminosity.

Due to the small cross section for the J/Ψ production, it was necessary to preserve as much statistics as possible. Therefore, the cuts on pile-up have been removed, as they unnecessarily reduced the statistics in this analysis without improving data quality. The final event and track quality cuts used in the rest of the analysis are listed in Table 6.4.

Table 6.4: Final Event and Track Quality Cuts

$\|V_Z\|$	$<$	40 cm
$\|\eta\|$	$<$	1
nHits	$>$	20
nHits/nPoss	$>$	0.52
DCA	$<$	3 cm
p_T	$>$	0.15 GeV/c
$flag$	$>$	0

The cut on p_T, along with cuts on the dE/dx and energy of particles, was modified to improve the purity of the identified electrons. This is described below.

TPC

Lighter hadrons, such as deuterons, protons, kaons, and pions, are created in higher abundance than electrons, as seen in Fig. 4.8. For $p_T < 1$ GeV/c, the expected dE/dx bands of pions, kaons, and protons overlap with that of electrons. This causes a large amount of contamination in the electron spectra in this region, even with very stringent electron identification requirements. Since the efficient removal of background was crucial to achieve a high level of certainty in our results, the minimum p_T required for electron candidates, ${p_T}^{\min}$, has been studied to optimize the significance and signal to background ratio for e^+e^- pairs in the J/Ψ mass region.

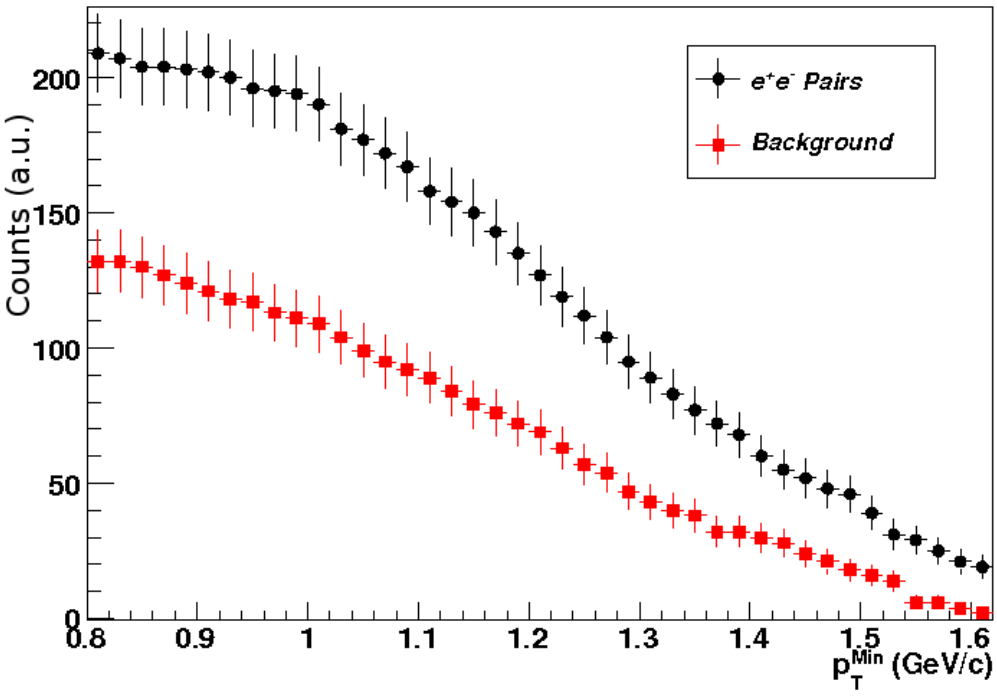

Figure 6.22: The number of event-wise same- and oppositely-charged electron pairs with $2.9 < m < 3.2$ GeV/c^2 versus the minimal p_T of each particle.

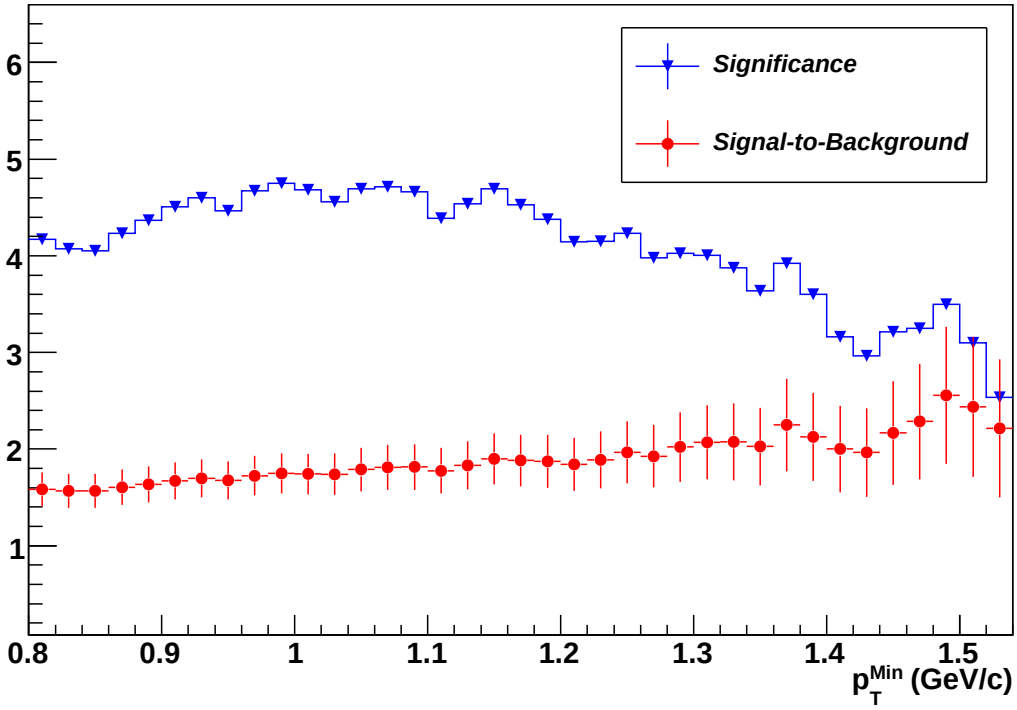

Figure 6.23: The significance (in blue) and the signal to backgroud ratio (in red) of the J/Ψ signal versus the minimum p_T of the electron daughters. The signal to background ratio slowly increases with ${p_T}^{Min}$ while the significance peaks around 1 GeV/c.

To optimise the value of ${p_T}^{\min}$, the set of TPC dE/dx electron identification cuts defined previously was used, with a range of values for ${p_T}^{\min} > 0.8$ GeV/c. The numbers of like- and unlike-sign electron pairs per event with $2.9 < m < 3.2$ GeV/c^2 versus the minimal p_T of both electron daughters are shown in Fig. 6.22. While the number of pairs decreases with increasing values of ${p_T}^{\min}$ (as expected due to the loss of statistics), the fall-off rate is much higher above ${p_T}^{\min} > 1.1$ GeV/c. The significance and the signal to background ratio of the J/Ψ signal versus the minimal p_T of the electron daughters are shown in Fig. 6.23, blue and red, respectively. The

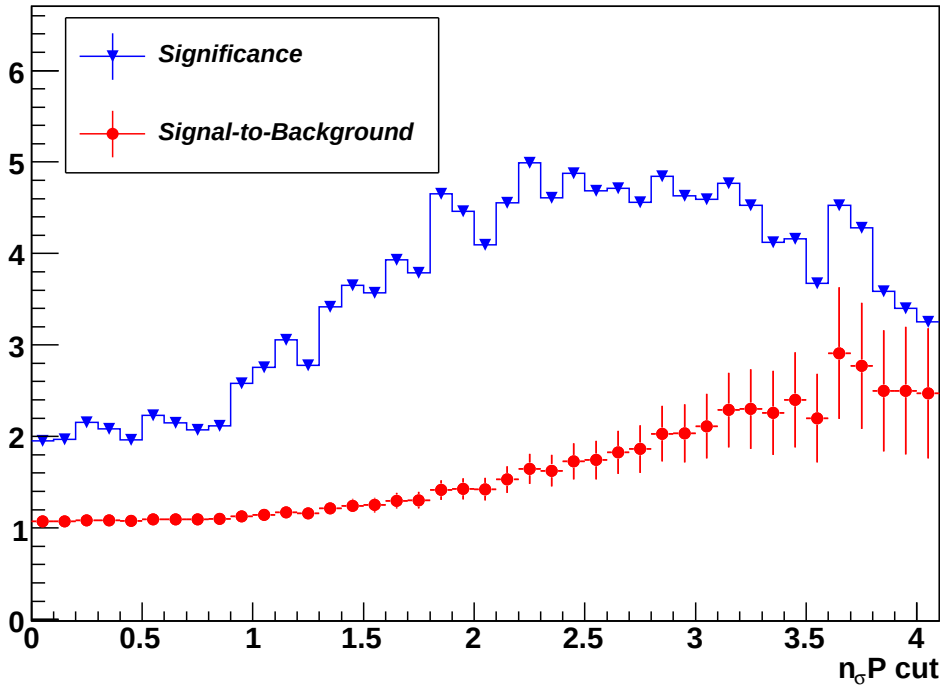

Figure 6.24: The significance (in blue) and the signal to backgroud ratio (in red) of the J/Ψ signal versus the veto cut on $|n\sigma_p|$ of the electron daughters. The signal to background ratio slowly increases with larger values of $|n\sigma_p|$, while the significance peaks around $|n\sigma_p| = 2.2$.

signal to background ratio gradually increases with increasing ${p_T}^{\min}$, while the significance peaks at ${p_T}^{\min} \approx 1$ GeV/c. The increasing signal to background ratio reflects the improved rejection of background with higher values of ${p_T}^{\min}$. However, given the drop in the significance at higher ${p_T}^{\min}$ due to the loss of statistics, a value of ${p_T}^{\min} = 1$ GeV/c was chosen.

The dominant sources of contamination for $p_T > 1$ GeV/c were pions and protons, as can be seen in Fig. 4.8, and cuts on $n\sigma_p$ and $n\sigma_\pi$ were used to exclude these hadronic contributions. The cuts $|n\sigma_\pi| > 2.5$, $|n\sigma_e| < 3$, and $p_T > 1$ GeV/c were

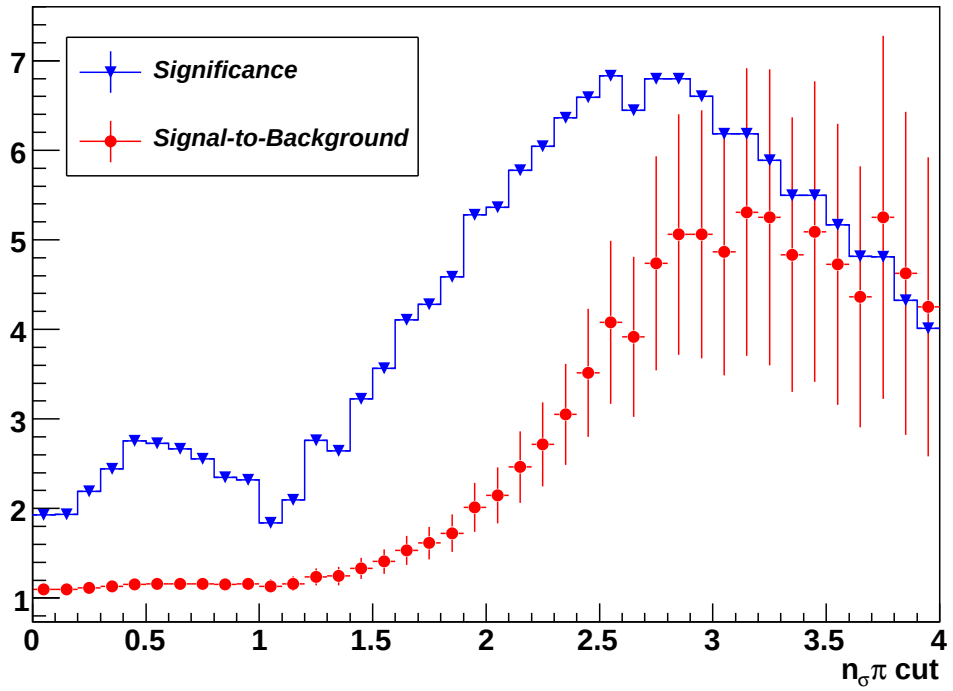

Figure 6.25: The significance (in blue) and the signal to backgroud ratio (in red) of the J/Ψ signal versus the veto cut on $|n\sigma_\pi|$ of the electron daughters. The signal to background ratio slowly increases with larger values of $|n\sigma_\pi|$, while the significance peaks around $|n\sigma_\pi| = 2.5$.

placed, and Sig and S/B were calculated while varying the cut on $n\sigma_p$, shown in Fig. 6.24. While the removal of background improved with increasing values of $n\sigma_p$, the significance peaked at $|n\sigma_p| \approx 2.2$.

Using the value $|n\sigma_p| > 2.2$, the same exercise was performed with $n\sigma_\pi$, and the results are shown in Fig. 6.25. A similar trend was observed, and the significance peaked at $|n\sigma_\pi| \approx 2.5$. With the requirement on the p_T of the tracks, and with the cuts on $n\sigma_p$ and $n\sigma_\pi$, the kaon contamination was also removed.

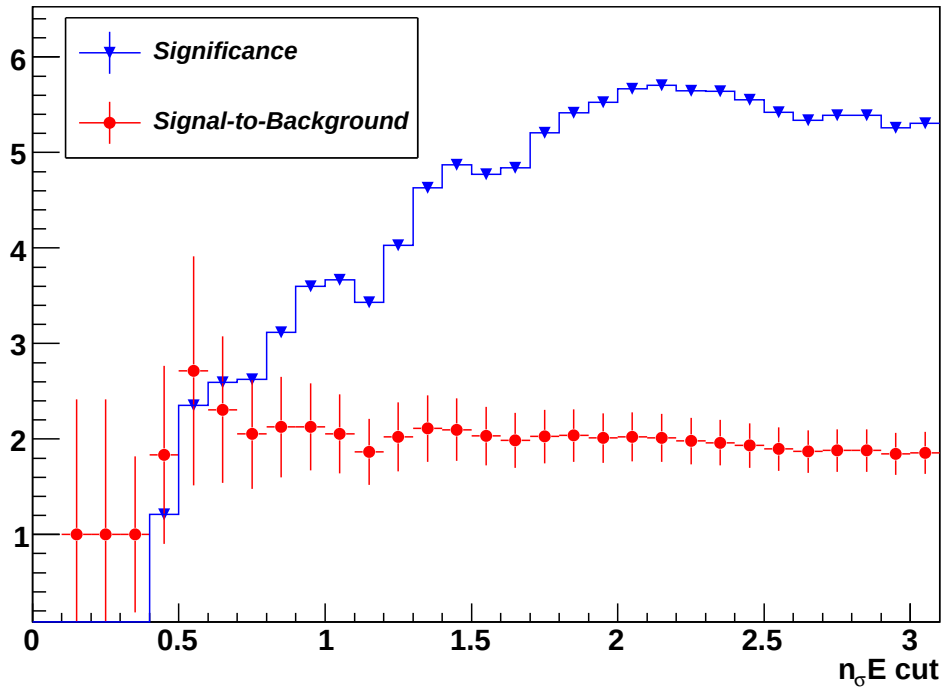

Figure 6.26: The significance (in blue) and the signal to backgroud ratio (in red) of the J/Ψ signal versus the acceptance cut on $|n\sigma_e|$ of the electron daughters. The signal to background ratio slowly decreases with larger values of $|n\sigma_e|$, while the significance peaks around $|n\sigma_e| = 2.1$.

The cut on $n\sigma_e$ has been optimised with the fixed veto cuts on protons and pions as mentioned above, and the results are shown in Fig. 6.26. While a wider cut increased statistics, it also introduced more background. The significance peaked at $|n\sigma_e| \approx 2.1$, and this value was used as an electron acceptance cut.

This entire process was repeated to make sure that we have a global optimisation without biasing the electron-pair population towards a phase-space which has un-physical enhancement in the J/Ψ signal. The TPC electron identification cuts developed in this section are summarized in Table 6.5, and a $\mathrm{d}E/\mathrm{d}x$ distribution of

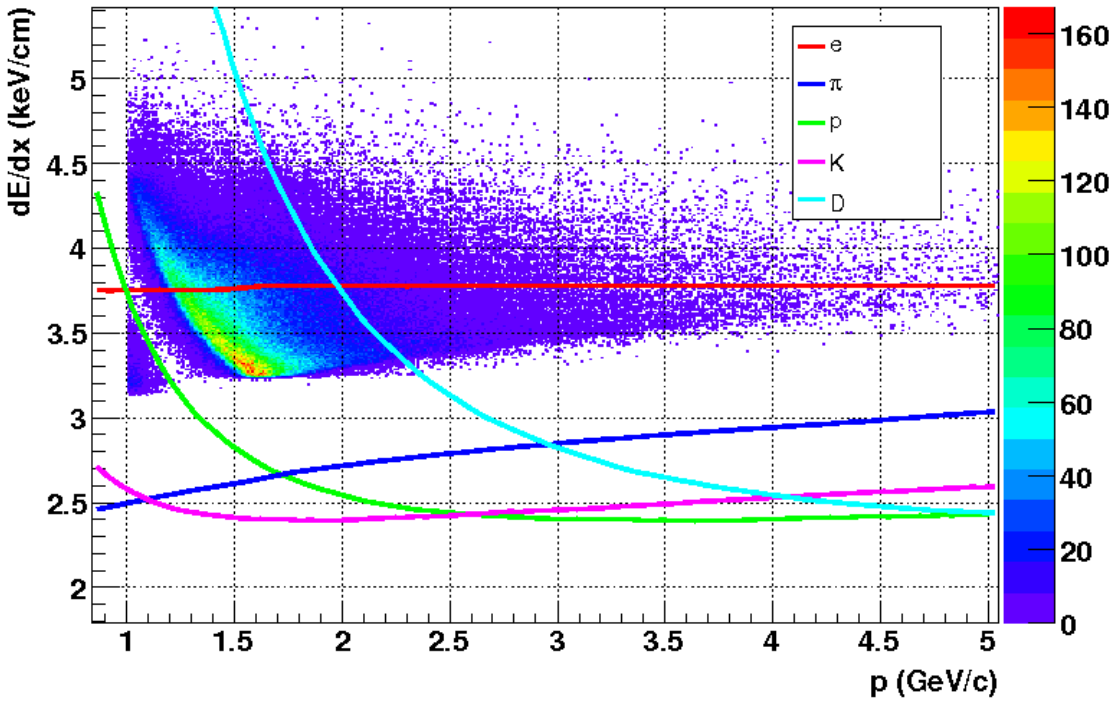

Figure 6.27: The $\mathrm{d}E/\mathrm{d}x$ versus momentum of tracks passing the electron selection criteria.

tracks accepted as electrons is shown in Fig. 6.27.

Table 6.5: TPC Electron Identification Cuts

p_T	$>$	1.0 GeV/c
$\lvert n\sigma_e \rvert$	$<$	2.1
$\lvert n\sigma_p \rvert$	$\geq$	2.2
$\lvert n\sigma_\pi \rvert$	$\geq$	2.5

BEMC

The trajectories of particles identified as electrons by the TPC were projected to the inner radius of the BEMC, located at a radius of 225.4 cm. From their position on the BEMC surface, the tower that the track could have fired was determined. Calibrations of the BEMC were applied during reconstruction, and pedestal values were subtracted from the tower energies to account for noise detected by the electronics. An energy distribution of electrons is shown on the left panel of Fig. 6.28, and the peak around zero corresponds to the noise in the electronics. This is shown in more detail on the right panel of Fig. 6.28, where a Gaussian is fitted to the noise peak. Electron candidates were required to deposit energies above 100 MeV within a tower, to remove noise contributions. The tower occupancy for electrons with $E > 100$ MeV is shown in η–ϕ coordinates in Fig. 6.29, and it is seen that the population is higher in the gold direction, at $\eta < 1$.

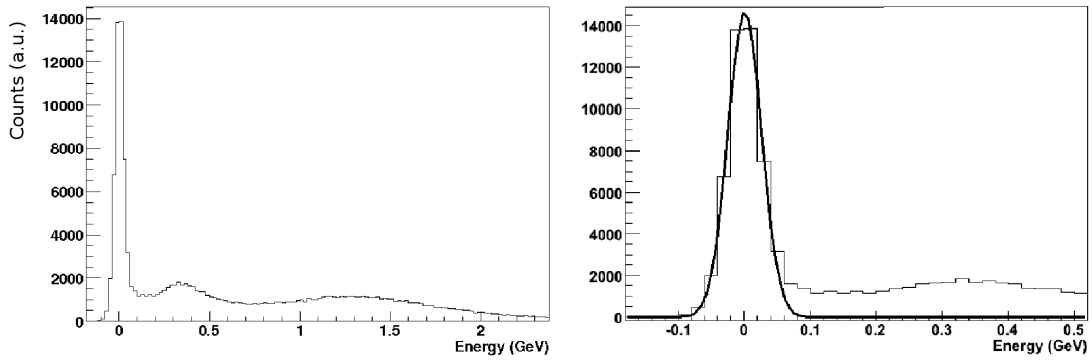

Figure 6.28: Energy distribution of electrons projected to the BEMC (left). The noise peak (right) was removed with a cut of $E > 100$ MeV.

Electrons colliding with the material in the BEMC have $\approx 95\%$ of their showers contained within a cone with a radius of 3.2 cm (Moliere radius). At midrapidity, the tower size in the BEMC is 10 cm $\times$ 10 cm, therefore, only $\approx 15\%$ of electrons deposit

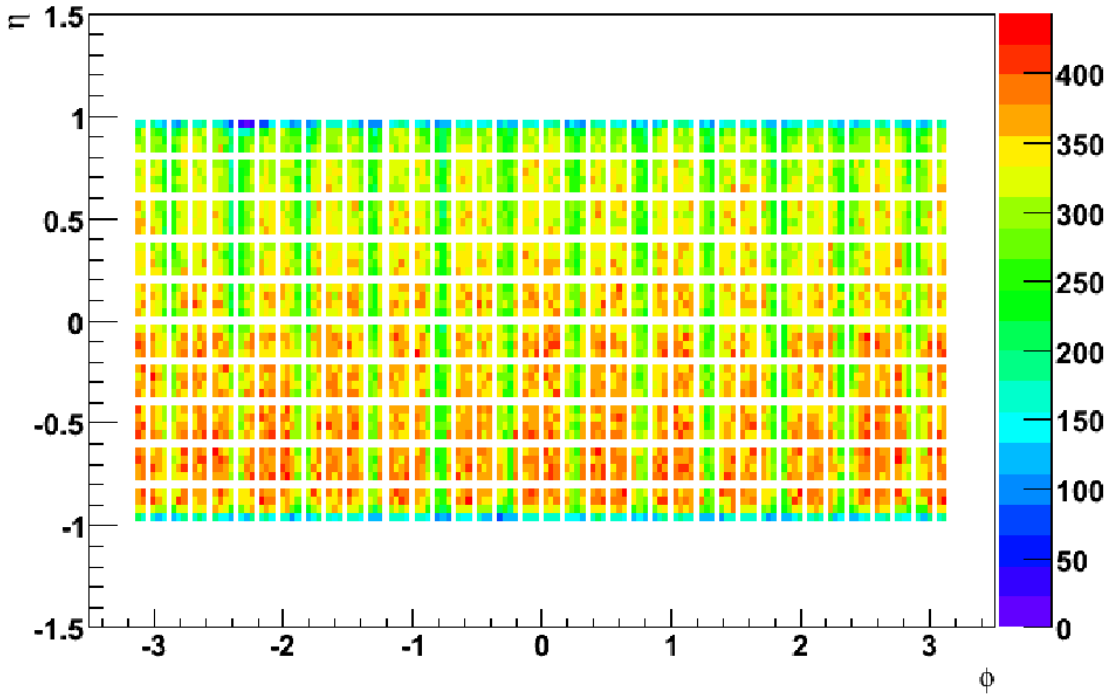

Figure 6.29: A distribution of matched towers for electrons with $E > 100$ MeV.

their full energy in a single tower. Electrons that hit close to the tower edge deposit energy in more than one tower, therefore, it was necessary to cluster towers together to reconstruct the full electron energy.

The clustering was implemented as follows. The tracks were projected to the BEMC and matched to a tower. The matched tower and the 8 surrounding towers were considered to be cluster candidates if they have an energy above 100 MeV each. The mean number of such towers for each electron is shown in Fig. 6.30, and the entries at zero correspond to tracks that did not match towers with energy above 100 MeV ($\approx$ 20% of electrons). Of the remaining electrons, which had a reconstructed energy above 100 MeV, about 52% deposited their entire energy in a single tower, 30% had 2 towers with energy above the threshold, and 13% deposited energy into

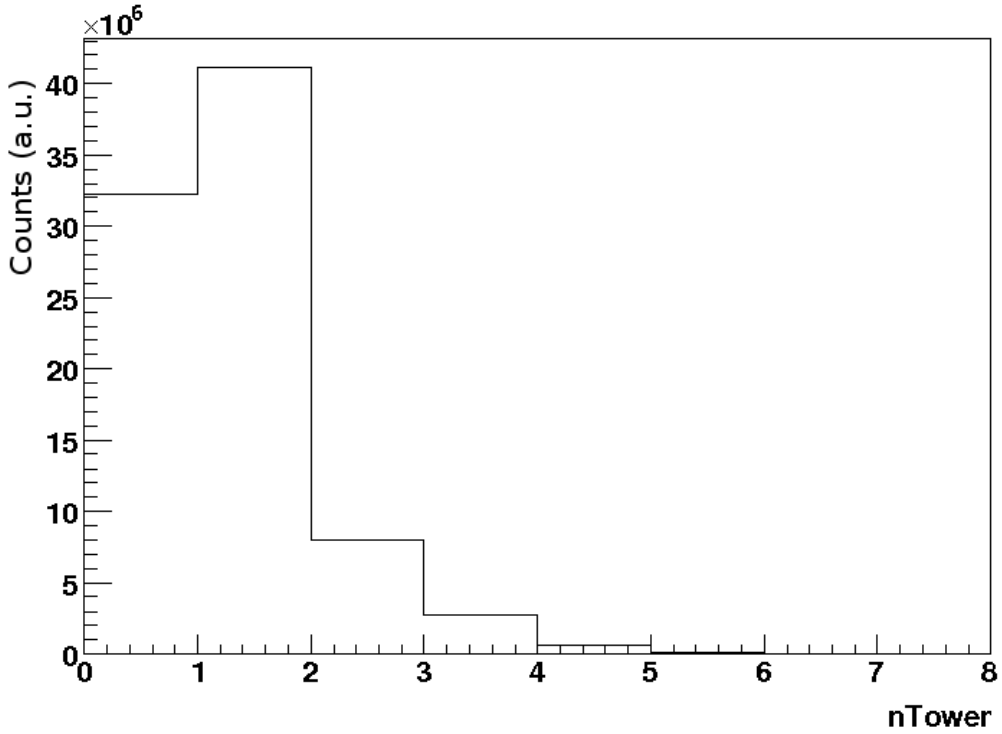

Figure 6.30: The number of towers with energy $E > 100$ MeV in the 3×3 tower array centred about electrons matched to the BEMC.

3 towers. It was very rare that electrons deposit energy into more than 2 towers, and the number of towers to use in energy clustering has been studied. This study required electrons with a high purity, which were selected using the stringent cuts

$$p_T > 1.0 \text{ GeV}/c, \tag{6.14}$$

$$|n\sigma_e| < 2.0, \tag{6.15}$$

$$|n\sigma_p| \geq 3.0, \tag{6.16}$$

$$|n\sigma_\pi| \geq 3.0. \tag{6.17}$$

The following energy distribution of tracks passing the above cuts were studied: (1) the single tower energy of the tower that the track projected to, (2) the sum of the highest three towers in the 3×3 tower cluster, and (3) the sum of all 9 towers in the

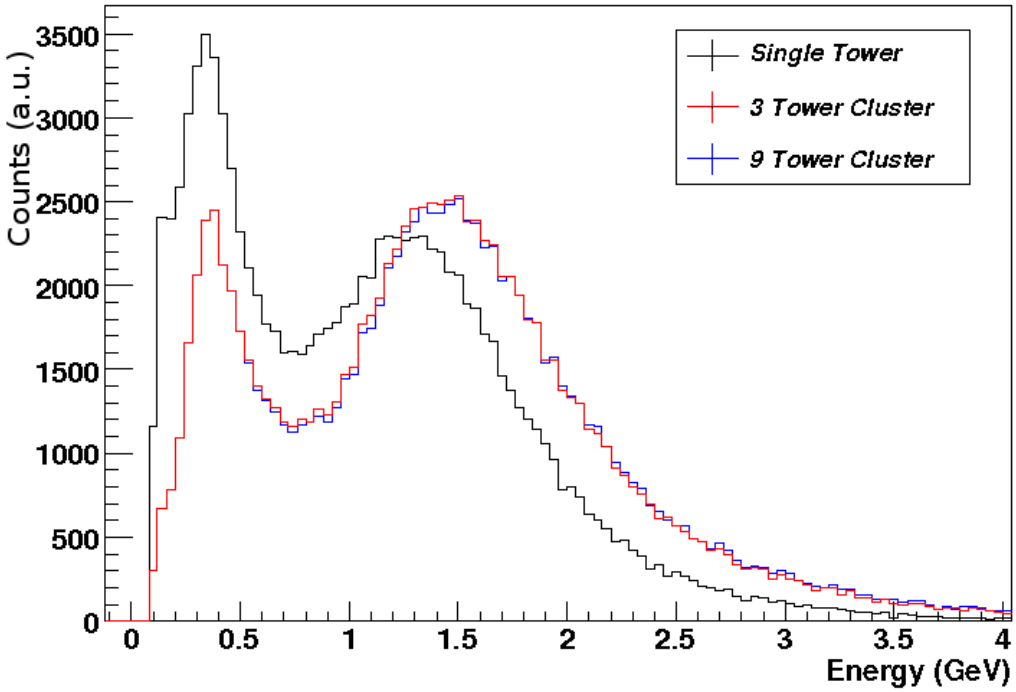

Figure 6.31: The energy distribution of electrons using single tower (black), 3 tower cluster (red) and 9 tower cluster (blue) energies.

3×3 tower cluster. The difference between the single tower and cluster tower energy spectra, shown in Fig. 6.31, was significant. However, there was minimal increase in energy when comparing the 3- and 9-tower cluster energies, therefore, the 3-tower electron cluster energy was was used in the further analysis. The single tower versus 3-tower cluster energy is shown in Fig. 6.32, where the entries along the diagonal correspond to the electrons which deposited their energy in one tower only. Of the electrons that deposited energy in more than one tower, the ratio of the single tower to 3-tower cluster energy, e_{ratio}, has been calculated, see Fig. 6.33. Figure 6.34 shows the distance between electrons and the centre of the tower they were matched to, for various values of e_{ratio}. The distribution falls off at the distance $D = 0.035$ in η–ϕ coordinates, corresponding to the half-diagonal length of a tower. Tracks with a value

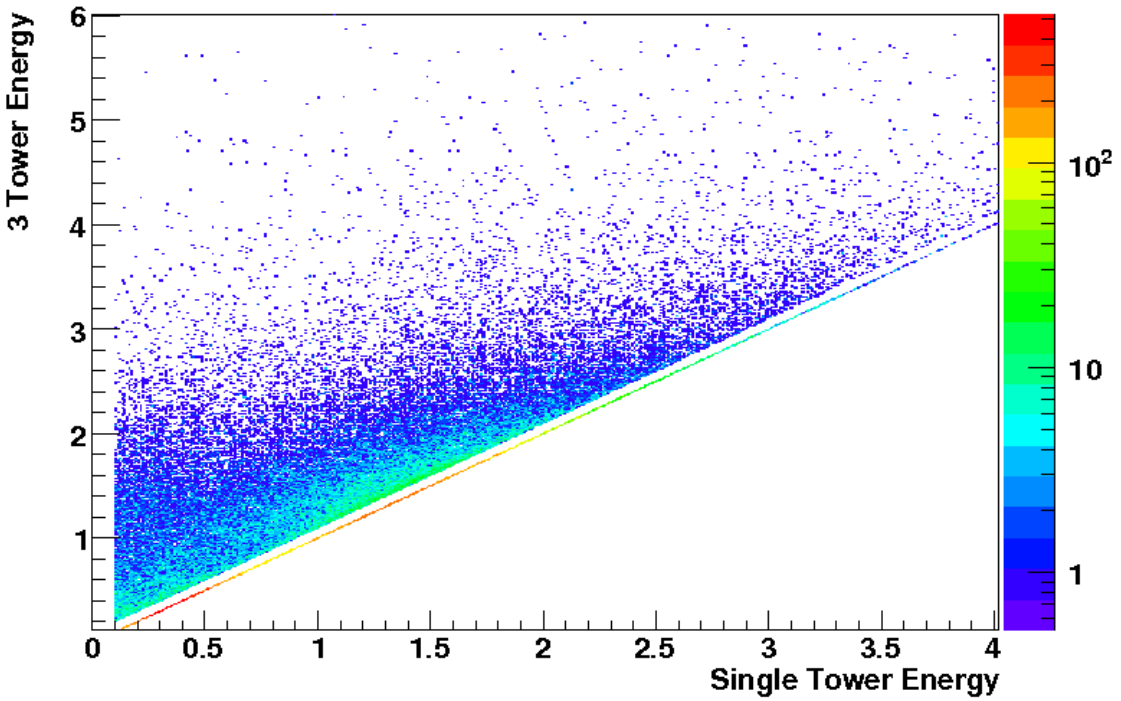

Figure 6.32: The energy distribution of electrons using single tower versus 3 tower cluster energy.

of $e_{\text{ratio}} = 1$ (red) have a mean position at $D \approx 0.016$, close to the centre of the tower. Selecting the electrons that hit closer to the edge of a tower moves the mean of the distribution closer to $D = 0.025$ (the half width of a tower), and increases e_{ratio}. This shows the success of energy clustering for electrons that did not hit near the centre of a tower.

Since the mass of electrons is significantly smaller than the minimum momentum of electron candidates, the energy deposited in the BEMC should be equal to the momentum reconstructed by the TPC. Since the measured E and $1/p$ distributions are both Gaussian (where the distribution widths represent the detector resolution), the

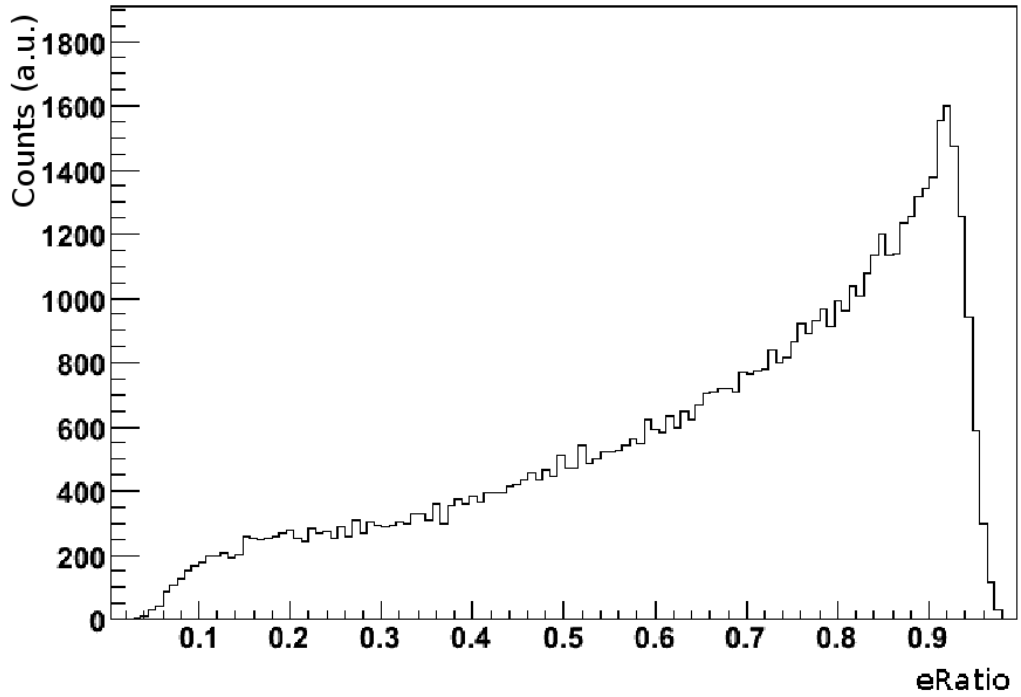

Figure 6.33: The ratio of single tower to 3 tower cluster energy, e_{Ratio}, for electrons with $e_{Ratio} < 1$.

ratio of E/p was used as an additional selection method for electron-hadron discrimination, allowing for a statistical approach in applying efficiency and error calculations. Figure 6.35 (left) shows the E/p ratio for particles identified as electrons by the TPC, that have also deposited an energy above 100 MeV in the BEMC. The hadronic contribution, where tracks were required to have $\mathrm{d}E/\mathrm{d}x < 2.5$ keV/cm, much less than that of electrons, is also shown. The two distributions have been scaled to match in the range $0.25 < E/p < 0.4$, and the hadron-subtracted E/p distribution is shown on the right panel of Fig. 6.35. A Gaussian has been fitted to the distribution, and although there is a slight shift away from unity of the electron peak in the E/p spectrum due to calibration effects and possible normalization uncertainty, there is a clear Gaussian nature to the distribution. The tail towards higher values of E/p is due to

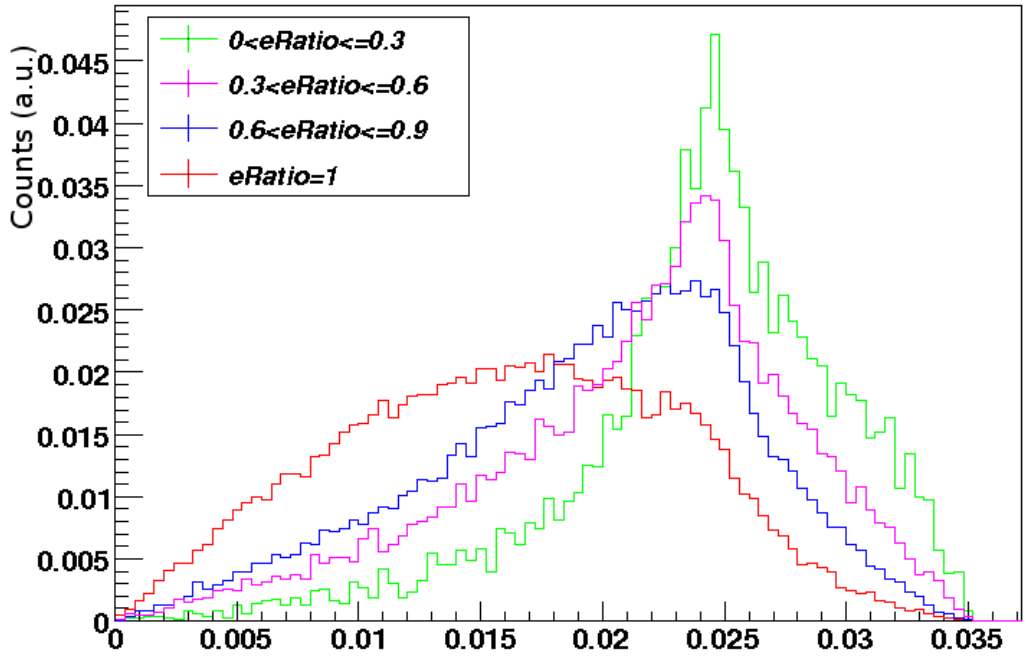

Figure 6.34: The distances between track and tower centre for various ratios of single tower to 3 tower cluster energy.

electrons undergoing bremsstrahlung in the material of the detector.

To remove the low-E/p hadronic contribution to the electrons identified in the TPC, electrons were initially required to have an energy to momentum ratio of $E/p > 0.6$. The optimisetion of the J/Ψ significance, described in the previous section, was repeated, now including the cut on E/p. The final cuts used for electron identification with the TPC and BEMC are listed in Table 6.6, and utilising the BEMC information allowed to improve the significance of the signal while loosening the dE/dx cuts. Results are presented in Chapter 7.

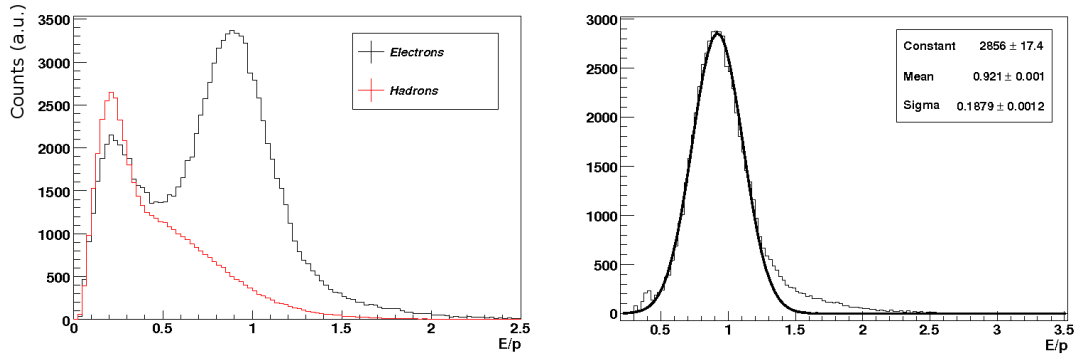

Figure 6.35: Left: E/p for electrons satisfying TPC requirements (black). In red, hadrons are selected by requiring $\mathrm{d}E/\mathrm{d}x < 2.5$ keV/cm. Right: E/p for electrons after hadron subtraction. A Gaussian has been fitted to the peak.

Table 6.6: TPC and BEMC electron identification cuts.

TPC		
p_T	$>$	1.0 GeV/c
$\lvert n\sigma_e \rvert$	$<$	2.1
$\lvert n\sigma_p \rvert$	$\geq$	2.2
$\lvert n\sigma_\pi \rvert$	$\geq$	2.5
BEMC		
E	$\geq$	0.1 GeV
E/p	$\geq$	0.5

6.4 Efficiency and Acceptance Corrections

Due to the finite precision and acceptance of the STAR detector, not all the J/Ψs created in a collision were correctly reconstructed. The loss of J/Ψs is caused by several different sources:

(1) *Acceptance losses.* The TPC is not able to reconstruct a J/Ψ if, for example, one of the daughter electrons has a pseudorapidity $|\eta| > 1$. The fraction of the total

phase space that the TPC and BEMC cover was corrected for with an acceptance correction factor $\varepsilon_{\rm acc}$.

(2) *J/Ψ reconstruction efficiency.* The TPC has finite track reconstruction efficiency, and some tracks within the acceptance of the detector may not get reconstructed. For example, two tracks very close together can be mistaken for one. These merged tracks can significantly distort the reconstructed $\mathrm{d}E/\mathrm{d}x$ of the detected particle(s), reducing the effectiveness of the STAR particle identification methods. There may also be losses when tracks cross the TPC sector boundaries and the track segments are not properly joined (split tracks). The reconstruction efficiency, $\varepsilon_{\rm rec}$, was calculated from the fraction of J/Ψs created in the $d+$Au collisions, whose electron daughters were both reconstructed in the TPC and pass the quality cuts mentioned before, i.e., as the number of reconstructed J/Ψs divided by the total number of created J/Ψs.

(3) *Electron identification efficiency.* The TPC cuts developed to identify electrons rejected those with $\mathrm{d}E/\mathrm{d}x$ values close to that of hadrons. There are also electrons identified by the TPC that did not have reconstructed BEMC hits. The efficiency of the electron selection criteria, $\varepsilon_{e\rm ID}$, was determined by calculating the expected electron yield and comparing it to the identified electron yield. Since electron pairs were used to reconstruct J/Ψs, the corresponding correction factor was included in quadrature in the final J/Ψ efficiency correction factor.

Individual corrections from (1) and (2) were calculated as a convoluted correction factor $\varepsilon_{\rm rec} \times \varepsilon_{\rm acc}$ as follows. Since it is unknown how many J/Ψs were produced in the collision, efficiency corrections relied on simulating the detector response to events. This was done using a Monte Carlo-based simulation, which generated J/Ψs, propagated them through the GEANT model of STAR, and embedded them into real events. The simulated J/Ψs and their electron daughters were identified by specific GEANT IDs. Once the embedded events were passed through the track reconstruction procedure, the reconstructed electrons from simulated J/Ψ decays that passed

the cuts listed in Table 6.4 (excluding cuts on $\mathrm{d}E/\mathrm{d}x$ and E/p) were identified and used to reconstruct the original parent J/Ψ. The number of reconstructed J/Ψs passing the quality cuts was compared to the total number of embedded J/Ψs as a function of transverse momentum and rapidity, and the correction factor $\varepsilon_{\mathrm{rec}} \times \varepsilon_{\mathrm{acc}}$ was obtained. The TPC efficiency was $\approx 20\%$, and depended on both J/Ψ transverse momentum and rapidity, as shown on the left and right panels of Fig. 6.36, respectively. Comparing the simulated momentum to the reconstructed momentum also provided information on the resolution of the TPC. This is shown in Fig. 6.37, where the difference between the simulated and reconstructed electron momenta is divided by the simulated momentum.

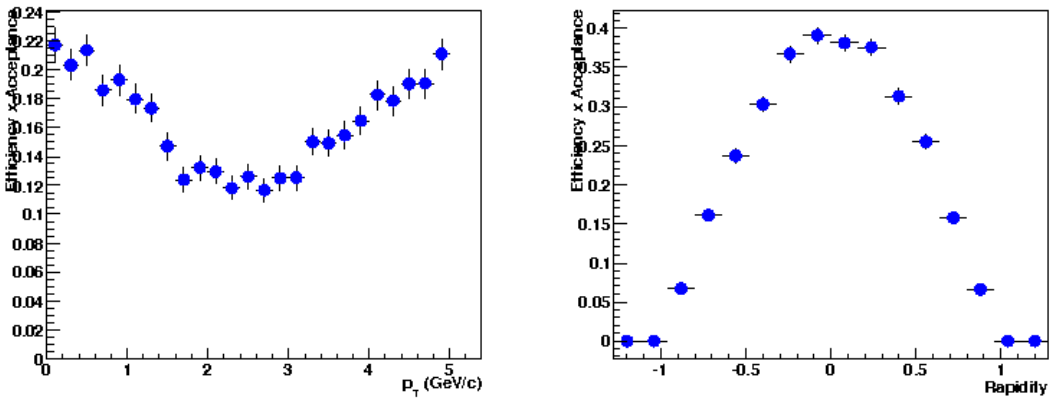

Figure 6.36: Efficiency correction factor $\varepsilon_{Rec} \times a$, left: as a function of ${p_T}^{\mathrm{J}/\Psi}$ integrated over rapidity $y^{\mathrm{J}/\Psi}$; right: s a function of $y^{\mathrm{J}/\Psi}$ integrated over ${p_T}^{\mathrm{J}/\Psi}$.

Electron identification efficiency correction was determined by comparing the total number of electrons produced in the collisions that passed the quality cuts in Table 6.4 to the number of identified electrons passing the same quality cuts and, in addition, electron identification cuts listed in Table 6.6. The total number of electrons reconstructed in the TPC was calculated by performing a multiple Gaussian fit to $n\sigma_e$ distributions in different momentum bins, see the left panel of Fig. 6.38. The

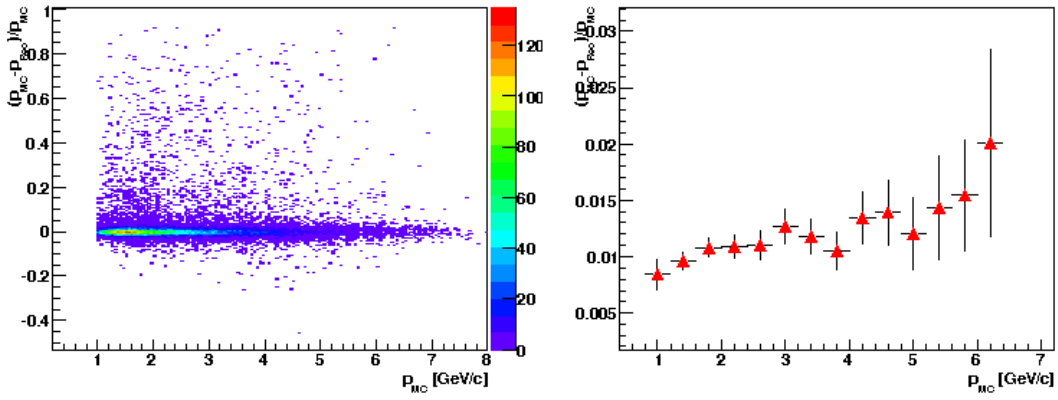

Figure 6.37: The momentum resolution of the TPC for electrons passing the TPC quality cuts.

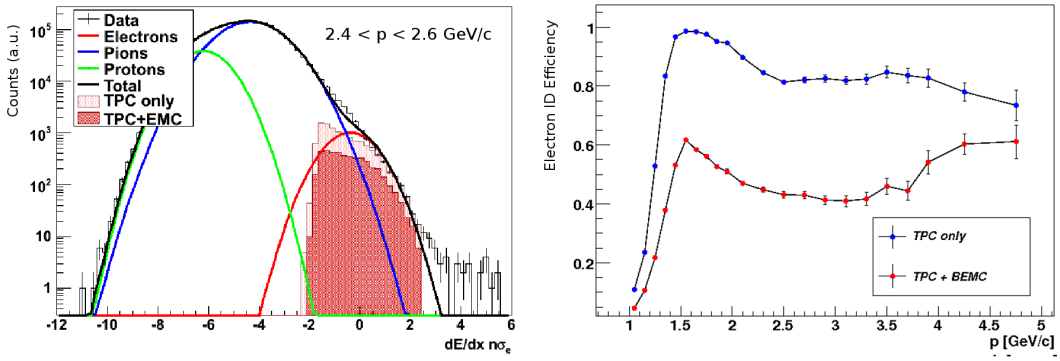

Figure 6.38: Left: An example of a $n\sigma_e$ distribution for all particles passing TPC quality cuts (black). Multiple Gaussians are fitted to determine particle yields. The shaded region are accepted electrons; light red: TPC only, dark red: TPC+BEMC. Right: The efficiency of the electron identification cuts for all momenta, using the TPC only (blue), and using TPC and BEMC eID (red).

integral of the Gaussian fitted to the electron peak (red curve) was compared to the number of electrons passing the electron identification cuts, to determine the electron identification efficiency $\varepsilon_{e\text{ID}}$; light red indicates electrons passing TPC eID cuts only,

dark red indicates electrons passing TPC+BEMC eID cuts.

The efficiency of the TPC and BEMC eID cuts has been calculated as a function of the daughter electron momentum (right panel of Fig. 6.38). While this efficiency is significantly lower than the efficiency obtained using only TPC eID ($\approx 80\%$), the high level of purity ($\approx 95\%$) of the electrons is reflected in the increased signal to background ratio of the J/Ψ signal, show in Fig. 7.2.

The total J/Ψ efficiency and acceptance correction factor is a product of all of the individual efficiency correction factors,

$$\varepsilon^{\mathrm{J}/\Psi} = \varepsilon_{rec}({p_T}^{\mathrm{J}/\Psi}, y^{\mathrm{J}/\Psi}) \times \varepsilon_{\mathrm{acc}} \times \varepsilon_{e\mathrm{ID}}(p_1) \times \varepsilon_{e\mathrm{ID}}(p_2), \tag{6.18}$$

and is presented in Chapter 7. This factor was applied to the uncorrected J/Ψ yield to obtain a corrected yield [Eq. (1.31)].

Chapter 7

Results

In this chapter we present the results obtained on J/Ψ production in $d+$Au collisions at $\sqrt{s_{NN}} = 200$ GeV in the STAR detector using the procedure described in Chapter 6. The phase-space in this analysis covers the full azimuthal angle with $-1 \leq y^{\mathrm{J}/\Psi} \leq 1$ and ${p_T}^{\mathrm{J}/\Psi} \leq 5$ GeV/c, where electron daughters are required to have $|\eta^e| < 1$ and $|pt^e > 1$ GeV/c. A total of 34×10^6 minimum-bias events within $|V_Z| < 40$ cm have been used to determine the J/Ψ yield.

First we will discuss the dielectron mass spectrum and obtain an uncorrected J/Ψ signal. After applying efficiency corrections, the corrected yield for 0%–20% central collisions will be presented and compared to J/Ψ yields in p+p collisions to determine the nuclear modification factor in $d+$Au collisions.

7.1 e^+e^- Invariant Mass Spectrum

The electron identification cuts determined in Chapter 6 are listed in Table 6.6. The dielectron invariant mass spectrum was obtained calculating the invariant mass of electron pairs, and is shown in Fig. 7.1, left: with the TPC electron cuts only; right: with the TPC and BEMC cuts. Shown in black are the opposite-sign pairs, and in red is the like-sign background described in Section 6.3.1. The two are compared to

illustrate the improved reduction in background when using the BEMC in electron identification. A clear peak around the J/Ψ mass can be seen in both mass spectra, and the errors are statistical only.

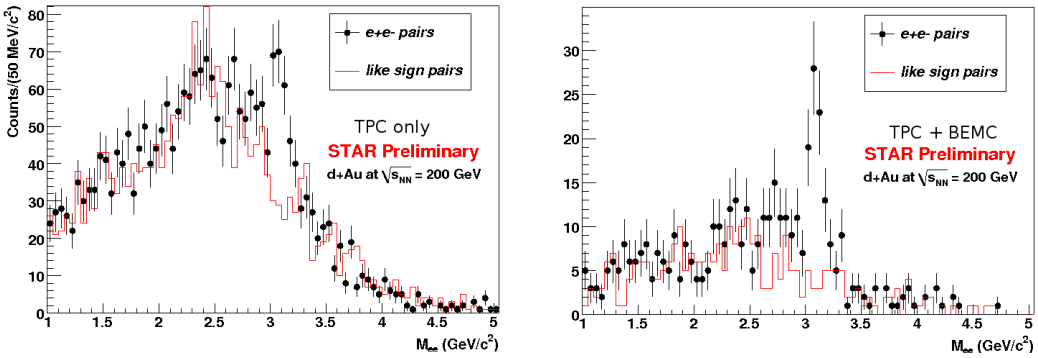

Figure 7.1: The dielectron invariant mass spectrum obtained using TPC cuts only (left), and using TPC and BEMC cuts (right) for electron identification. Opposite- and like-sign pair distributions are shown in black and red, respectively.

7.2 Uncorrected J/Ψ Signal

The background has been subtracted from the invariant mass spectrum (shown in Fig. 7.1), and the uncorrected J/Ψ signal after background subtraction is shown in Fig. 7.2, left: using TPC electron identification cuts only; right: using TPC and BEMC electron identification cuts. While there is a larger yield when only using the TPC, the signal obtained using TPC and BEMC cuts is more clear and well defined due to the reduced background.

The uncorrected yield, $N_{J/\Psi}$, signal to background ratio, S/B, and significance, Sig, for the invariant mass spectra are summarized in Table 7.1, where the number of J/Ψ's has been counted in the mass window $2.9 \leq m \leq 3.3$ GeV/c^2.

Table 7.1: J/Ψ signal information for 0%–100% central collisions.

TPC Only		
$N_{J/\Psi}$	=	156 ± 25
S/B	=	1.7
Sig	=	6.3
TPC and BEMC		
$N_{J/\Psi}$	=	81 ± 12
S/B	=	3.9
Sig	=	6.9

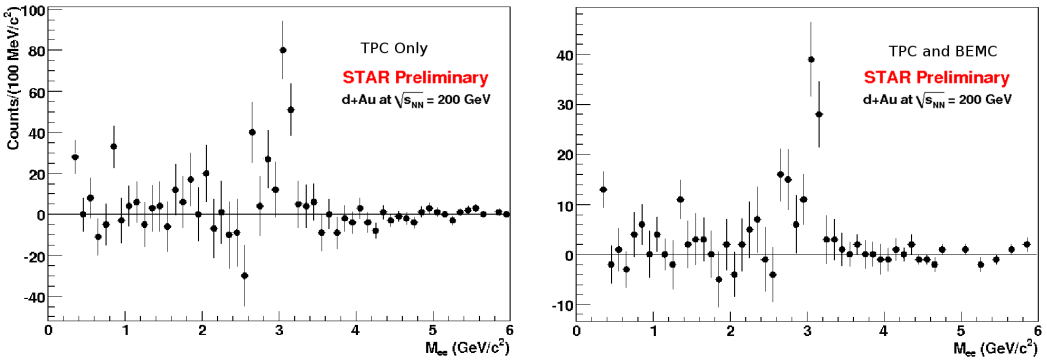

Figure 7.2: The uncorrected J/Ψ mass spectrum obtained using using TPC cuts only (left), and using TPC and BEMC cuts (right) for electron identification, after background subtraction.

There is a low-mass tail observed in the J/Ψ peak in Fig. 7.2 which is mostly excluded with the J/Ψ mass window of $2.9 \leq m \leq 3.3\text{GeV}/c^2$. We expect some electrons to undergo bremsstrahlung when passing through the detector material, and the subsequent loss of energy results in a lower reconstructed invariant mass. However, due to low statistics it is hard to distinguish between fluctuations and actual bremsstrahlung. To predict the J/Ψ lineshape, J/Ψs were simulated using PYTHIA [81], and embedded into actual events to determine the detector effects on the reconstructed mass of the J/Ψ. The line shape from embedding has been fitted

to the data, as shown in Fig. 7.3. To understand the J/Ψ lineshape, the J/Ψ signal obtained using both the TPC and BEMC has been used, because the reduced background improves the uncertainty in the signal shape. The data and simulation agree above 3 GeV/c^2, but there is a slight discrepancy for lower masses.

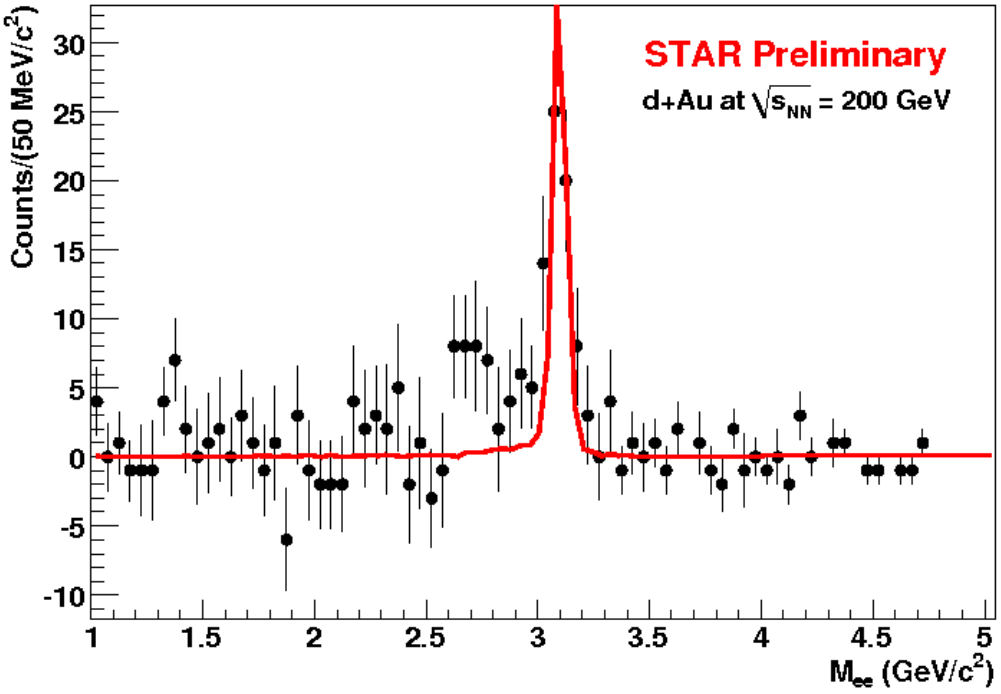

Figure 7.3: The uncorrected J/Ψ mass spectrum after backgroud subtraction (black), and the line shape from simulations (red).

To model the line shape, we fit a Crystal Ball function [82] to the mass distribution, shown in Fig. 7.4. The Crystal Ball function is defined by a Gaussian with a power-law tail,

$$f(x;\alpha;n;\bar{x};\sigma) \quad = \quad N \cdot \begin{cases} \exp\left(\frac{-(x-\bar{x})^2}{2\sigma^2}\right) & \text{for} \frac{x-\bar{x}}{\sigma} > -\alpha, \\ A \cdot \left(B - \frac{x-\bar{x}}{\sigma}\right)^{-n} & \text{for} \frac{x-\bar{x}}{\sigma} \leq -\alpha, \end{cases} \tag{7.1}$$

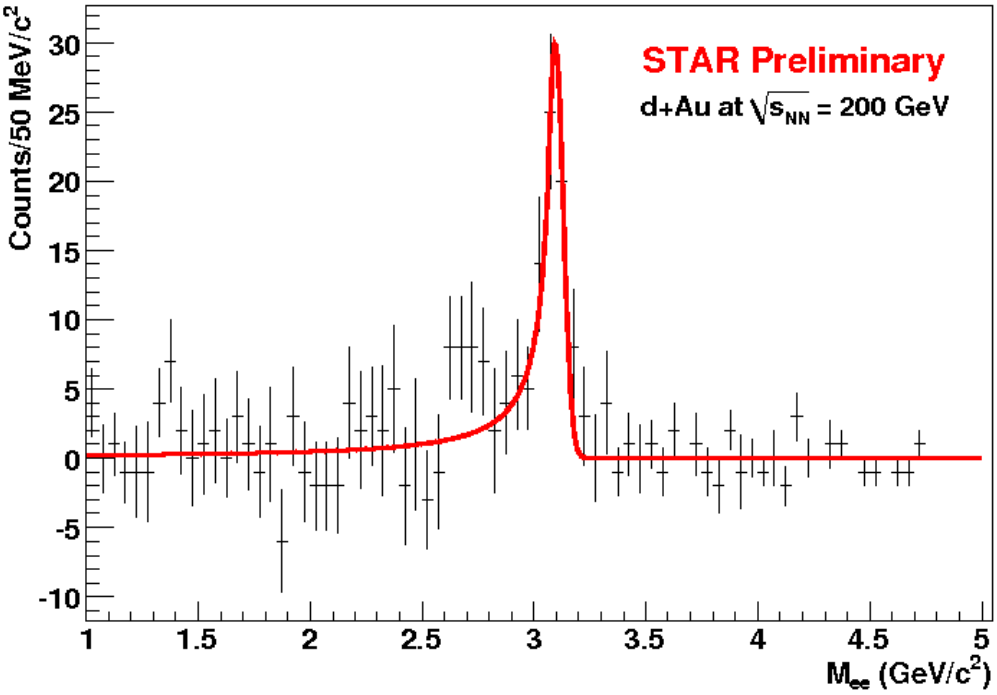

Figure 7.4: The uncorrected J/Ψ mass spectrum after backgroud subtraction (black), and a Crystal Ball function fitted to the data (red).

where

$$A = \left(\frac{n}{|\alpha|}\right)^n \cdot \exp\left(-\frac{|\alpha|^2}{2}\right), \tag{7.2}$$

$$B = \frac{n}{|\alpha|} - |\alpha|\,, \tag{7.3}$$

and where N, $\bar{x}$ and σ, are the height, mean and width of the underlying Gaussian, and α and n describe the low-end tail. The fitted mean of $\bar{x} = 3.096 \pm 0.009$ GeV/c^2 is consistent with the PDG [34] value for the J/Ψ mass, $m_{\mathrm{J}/\Psi} = 3.096916 \pm 0.000011$ GeV/c^2, and there is a significant contribution from the low-mass tail. The J/Ψ yield predicted by the Crystal Ball function is $\approx$ 30% larger than the yield obtained from the embedding lineshape shown in Fig. 7.3.

The J/Ψ yield is calculated from the integral of the embedding lineshape fitted to the data. The difference between the yield from the embedding lineshape and the Crystal Ball function are included in the systematic errors, presented in Section 7.5.

A clear J/Ψ signal is observed using the TPC and BEMC, even before background subtraction. The large significance and signal to background ratio reflect the high level of hadron discrimination obtained with the cuts developed in this analysis. This analysis focuses on 0%–20% central $d+$Au collisions.

0%–20% Central Collisions

Central collisions have been selected by requiring a minimum multiplicity in the East FTPC multiplicity of ≈ 11, as indicated by the dotted 0%–20% line in Fig. 6.16. The reconstructed dielectron invariant mass spectrum for 20% most central $d+$Au collisions is shown in Fig. 7.5. There is a clear peak observed around the J/Ψ mass, while statistics have decreased by a factor or ≈ 2 compared to 0%–100% central collisions.

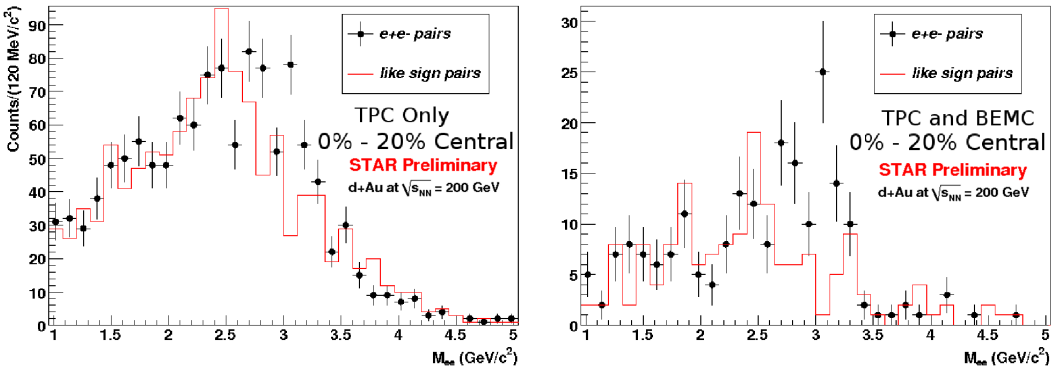

Figure 7.5: In black: The dielectron invariant mass spectrum for 0%–20% central collisions. In red, the like-sign background.

The background, shown in red in Fig. 7.5, has been subtracted from the invariant mass spectrum to obtain a J/Ψ signal, shown in Fig. 7.6. The uncorrected yield, significance, and signal to background ratio, obtained by counting the number of J/Ψs in the mass window $2.8 < m < 3.2$ GeV/c^2, are listed in Table 7.2.

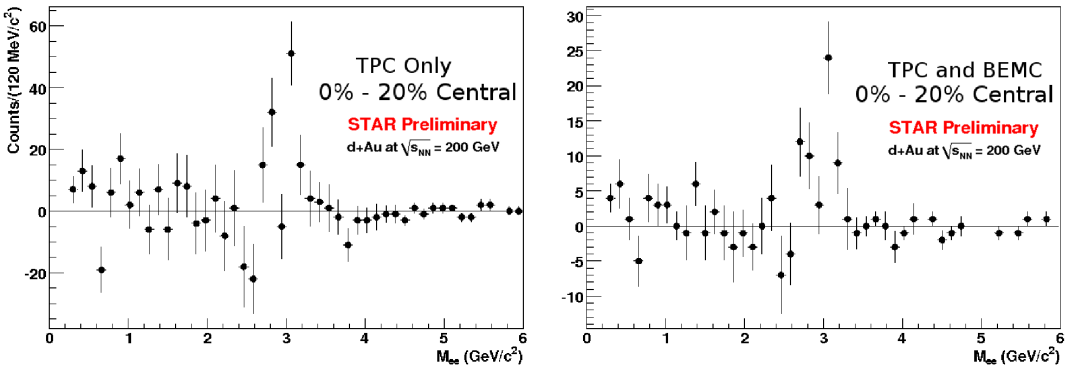

Figure 7.6: The uncorrected J/Ψ mass spectrum for 0%–20% central collisions after background subtraction.

Table 7.2: J/Ψ signal information for 0%–20% central collisions.

TPC Only		
$N_{J/\Psi}$	=	65 ± 15
S/B	=	1.7
Sig	=	4.4
TPC and BEMC		
$N_{J/\Psi}$	=	31 ± 7
S/B	=	4.2
Sig	=	4.7

The yields are obtained from fitting the embedding lineshape to the data, and both signals exhibit a large significance and signal-to-background ratio.

While statistics were limited, a clear J/Ψ signal in the dielectron invariant mass spectrum was observed for 0%–20% central collisions. The uncorrected J/Ψ p_T spectrum after background subtraction for 0%–20% central collisions is shown in Fig. 7.7, with TPC cuts only (left), and with TPC and BEMC cuts (right). The high level of hadron discrimination in the J/Ψ signal is reflected in the large significance and signal to background ratio. Next, a corrected J/Ψ yield was obtained by correcting the J/Ψ p_T spectrum for tracking and particle identification efficiencies.

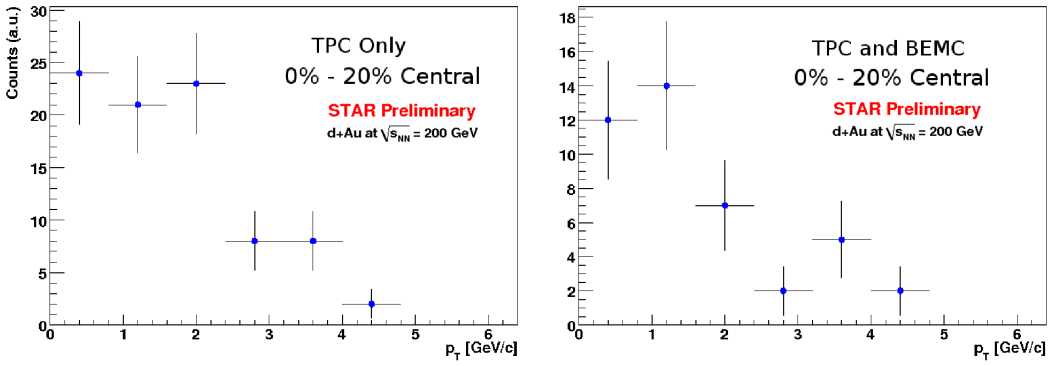

Figure 7.7: The uncorrected J/Ψ p_T spectrum for 0%–20% central collisions (after background subtraction), left: TPC *e*ID cuts only; right: TPC and BEMC cuts.

7.3 Corrected J/Ψ Yield

The TPC J/Ψ reconstruction efficiency and acceptance, shown in Fig. 6.36, has been combined with the electron identification efficiency (Fig. 6.38, right), using Eq. (6.18). The total J/Ψ efficiency and acceptance correction is shown in Fig. 7.8, for TPC electron identification cuts only (blue), and for TPC and BEMC *e*ID cuts (red). The efficiency versus J/Ψ p_T ranges from 3% to 8% when using TPC and BEMC cuts, and increases to 13%–27% when only using TPC cuts. This change in efficiency is due to the difference in electron identification efficiency shown in Fig. 6.38 (right).

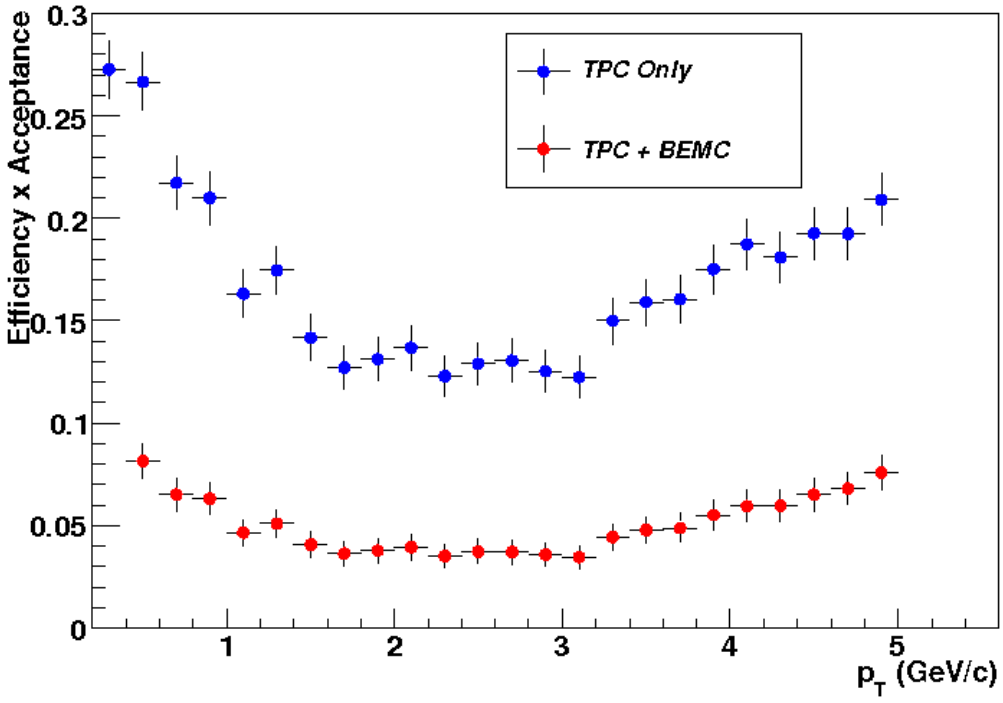

Figure 7.8: The total J/Ψ efficiency correction, blue: TPC electron identification cuts only; red: TPC and BEMC eID.

The J/Ψ p_T spectrum, shown in Fig. 7.7, has been corrected using the efficiency corrections, shown in Fig. 7.8, in momentum bins of 1 GeV/c width, due to limited statistics. The corrected J/Ψ p_T spectrum for 0%–20% central collisions is shown in Fig. 7.9, for TPC electron identification cuts only (blue), and TPC and BEMC eID cuts (red). Shown in black is the published PHENIX J/Ψ invariant yield for 0%–100% central collisions for J/Ψs with rapidity $|y^{\mathrm{J}/\Psi}| < 0.35$ [57] (only a p_T-integrated yield is available for 0%–20% central, this is discussed in the Section 7.4), where the dotted line is a power-law function fitted to the PHENIX data,

$$f(p_T) = A \cdot \left(1 + \left(\frac{p_T}{B}\right)^2\right)^{-6}, \tag{7.4}$$

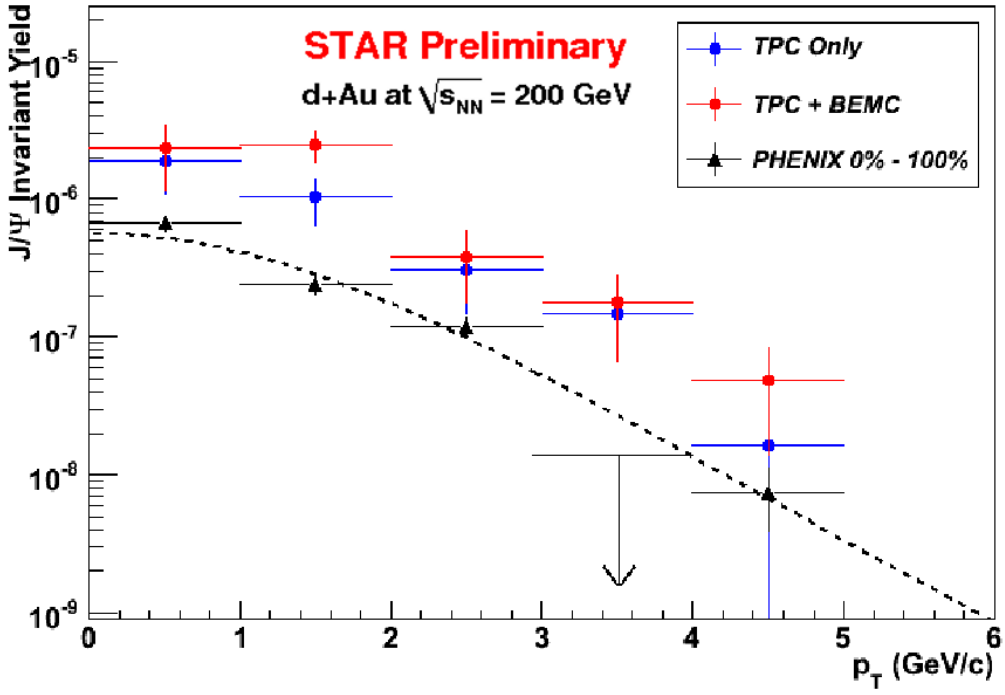

Figure 7.9: The corrected 0%–20% central J/Ψ p_T spectrum, blue: TPC electron identification cuts only; red: TPC and BEMC eID. Black: PHENIX J/Ψ invariant yield results for 0% - 100% central $d+$Au collisions. The dotted line is a power-law fit to the PHENIX data. Only statistical errors are shown.

where $A = 5.65 \times 10^{-7}$ (GeV/c)$^{-2}$ and $B = 4.30$ GeV/c. Although the yield per event in 0%–20% central collisions was expected to be approximately twice as large than that in 0% - 100% central collisions, due to the larger J/Ψ production cross section at higher energies, the invariant yields obtained using STAR data are larger than the expected values based on PHENIX results. There is a large discrepancy between yields obtained using TPC eID cuts only, and those using TPC and BEMC eID cuts, and this is most prominent for $1 < {p_T}^{\mathrm{J}/\Psi} < 2$ GeV/c. This is reflected in the p_T-integrated invariant yield, calculated from Eq. (1.32), listed in Table 7.3 (only statistical errors are shown), and these two values do not agree. The reason for

this uncertainty can be explained as follows. There is a strong correlation between the electron daughter momentum and parent J/Ψ p_T. We notice that due to the steep fall-off of the electron identification efficiencies at low electron momentum (see Fig. 6.38, right), small changes in these values have a large impact on the corrected yield for ${p_T}^{\mathrm{J}/\Psi} \approx 1 - 1.5$ GeV/c. To constrain the uncertainty in applying efficiency corrections for low momentum electrons, a cut of $p_e > 1.5$ GeV/c was placed on the daughter electrons.

Table 7.3: Integrated J/Ψ yield for 0%–20% central collisions (statistical errors only).

TPC Only
$B \cdot \mathrm{d}N/\mathrm{d}y = 2.0 \pm 0.4 \times 10^{-5}$
TPC and BEMC
$B \cdot \mathrm{d}N/\mathrm{d}y = 4.2 \pm 0.8 \times 10^{-5}$

The J/Ψ efficiency has been re-calculated with the requirement that electrons have a momentum greater than 1.5 GeV/c, as shown in Fig. 7.10 with TPC eID cuts only (blue), and TPC add BEMC eID cuts (red). Increasing the cut on the daughter electron momentum decreases the J/Ψ reconstruction efficiency at low p_T. Using this efficiency, the yield for J/Ψs with daughter momentum $p_e > 1.5$ GeV/c has been corrected, as shown in Fig. 7.11, and once again the 0%–20% central STAR measurements are compared to 0%–100% central PHENIX measurements. As a result, the STAR yields should be roughly twice the PHENIX yields. The p_T-integrated invariant yields when requiring $p_e > 1.5$ GeV/c are shown in Table 7.4 (only statistical errors are shown).

While there is little variation in the yield obtained using the TPC only, the invariant yield obtained using the TPC and BEMC has decreased substantially. These two values are in agreement within errors. The increased sensitivity of the yield obtained using both TPC and BEMC eID cuts arises from the electron identification efficiency calculation. The uncertainty in the fitting, combined with the reduced

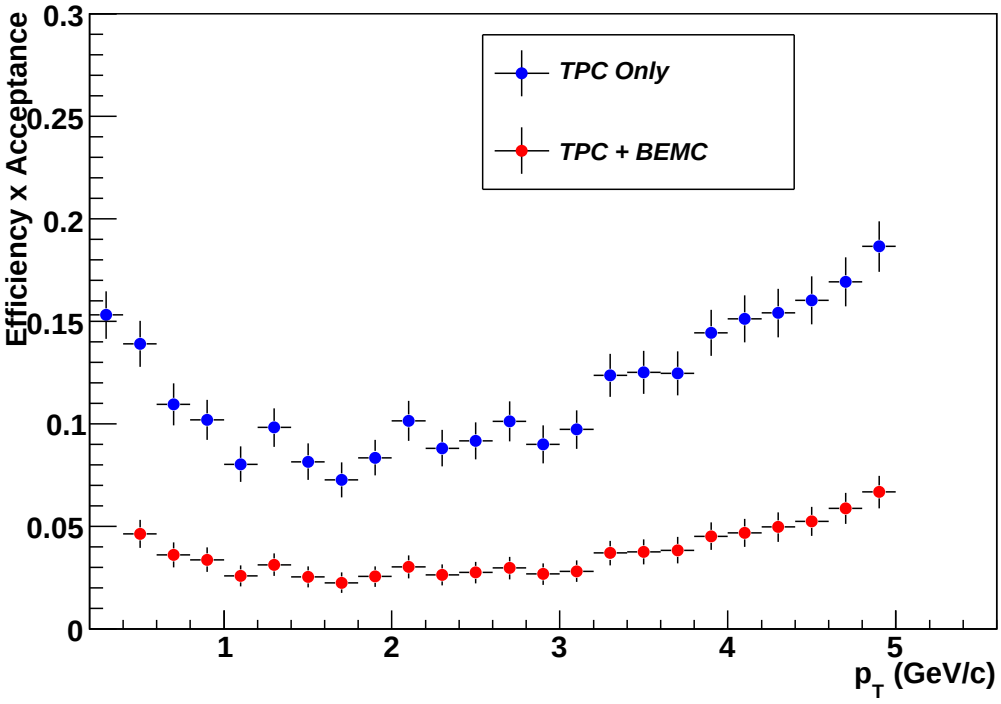

Figure 7.10: The total J/Ψ efficiency correction with daughter electron $p_e > 1.5$ GeV/c, blue: TPC electron identification cuts only; red: TPC and BEMC eID.

Table 7.4: Integrated J/Ψ yield for 0%–20% central collisions, with $p_e > 1.5$ GeV/c (statistical errors only).

TPC Only
$B \cdot \mathrm{d}N/\mathrm{d}y = 2.0 \pm 0.6 \times 10^{-5}$
TPC and BEMC
$B \cdot \mathrm{d}N/\mathrm{d}y = 3.2 \pm 0.8 \times 10^{-5}$

statistics obtained when requiring electrons matched to the energy deposited in the BEMC, introduces a large systematic uncertainty in the invariant yield, as was illustrated previously. Extensive variation on the TPC requirements have verified the stability of the invariant yield obtained using only TPC eID cuts. Until there is a

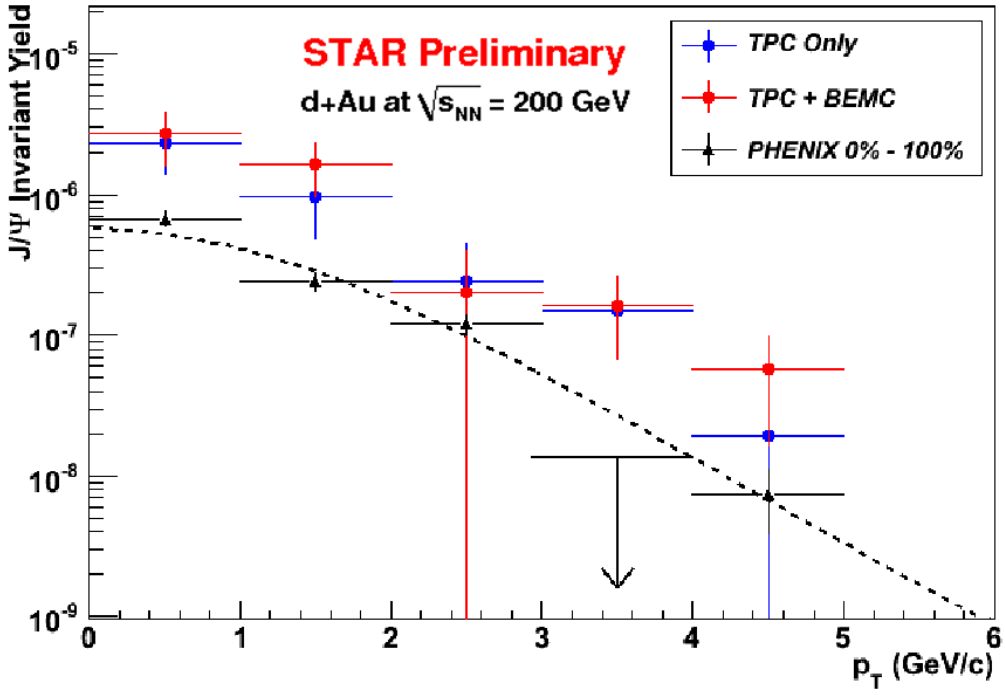

Figure 7.11: The corrected 0%–20% central J/Ψ p_T spectrum with daughter electron $p_e > 1.5$ GeV/c, blue: TPC electron identification cuts only; red: TPC and BEMC eID. Black: PHENIX J/Ψ invariant yield results for 0% - 100% central $d+$Au collisions. The dotted line is a power-law fit to the PHENIX data. Only statistical errors are shown.

better handle on the efficiency calculation when requiring BEMC information, results obtained using only the TPC will be presented. Since the results obtained using only the TPC remain unchanged when requiring $p_e > 1.5$ GeV/c, this cut was removed to increase statistics.

The J/Ψ p_T spectrum obtained using only the TPC, for 0%–20% central collisions, is shown in Fig. 7.12. The yield in each p_T bin has been obtained by fitting the lineshape from embedding to the data. A power-law function has been fitted to the data, and the centroids of each p_T bin have been calculated from a weighted mean.

The data and the power law function are in good agreement. The invariant yield of $\mathrm{B} \cdot \mathrm{d}N/\mathrm{d}Y = 2.0 \pm 0.4 \times 10^{-5}$ was obtained in 0%–20% central $d+\mathrm{Au}$ collisions. In order to determine the in-medium effects of the collision system on J/Ψ production, the invariant yield is compared to J/Ψ yields in p+p collisions in the following section.

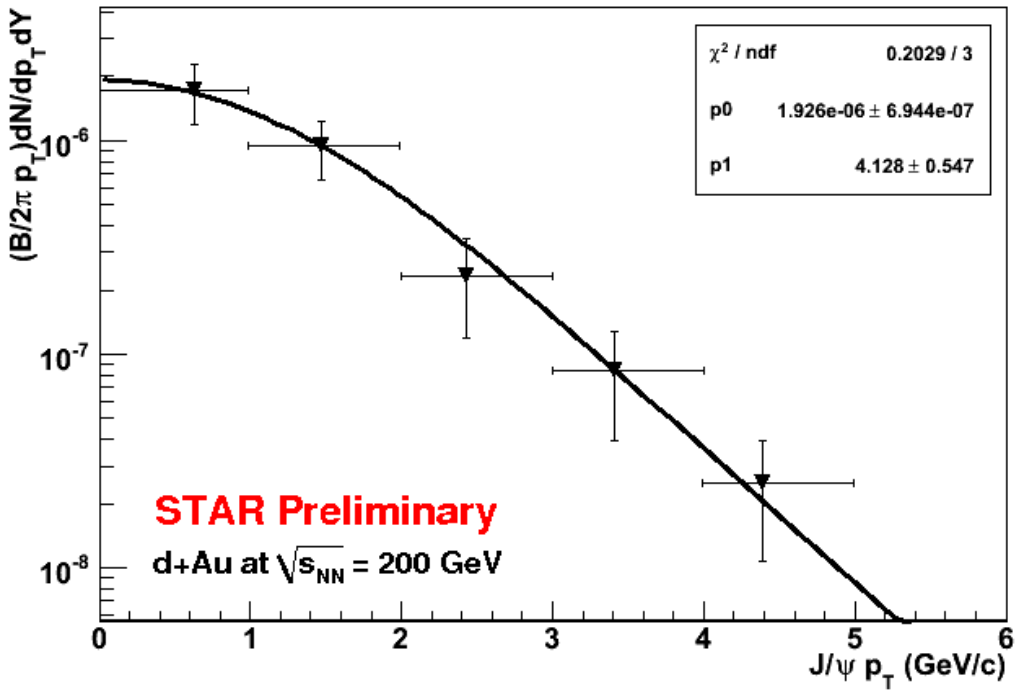

Figure 7.12: The corrected 0%–20% central J/Ψ p_T spectrum obtained using the TPC only. Only statistical errors are shown.

7.4 $R_{d+\mathrm{Au}}^{\mathrm{J}/\Psi}$

The invariant yield obtained with only the TPC electron identification cuts, shown in Fig. 7.12, has been divided by the J/Ψ yield in p+p collisions recorded at STAR [83], and scaled by the number of binary collisions, to determine the nuclear modification factor. For 0%–20% central $d+\mathrm{Au}$ collisions, the average number of binary collisions

obtained from the Glauber calculations is $\langle N_{\rm coll} \rangle = 14.6$. The nuclear modification factor $R_{dA}^{\rm J/\Psi}$ for $-1 < y^{\rm J/\Psi} < 1$ is shown in Fig. 7.13 (red), together with the published PHENIX data for $-0.35 < y^{\rm J/\Psi} < 0.35$ [57] (blue). The red box on the right indicates the normalization uncertainty, and the light red shaded box on the STAR data point indicates the systematic uncertainty in the measurement. This is discussed in Section 7.5.

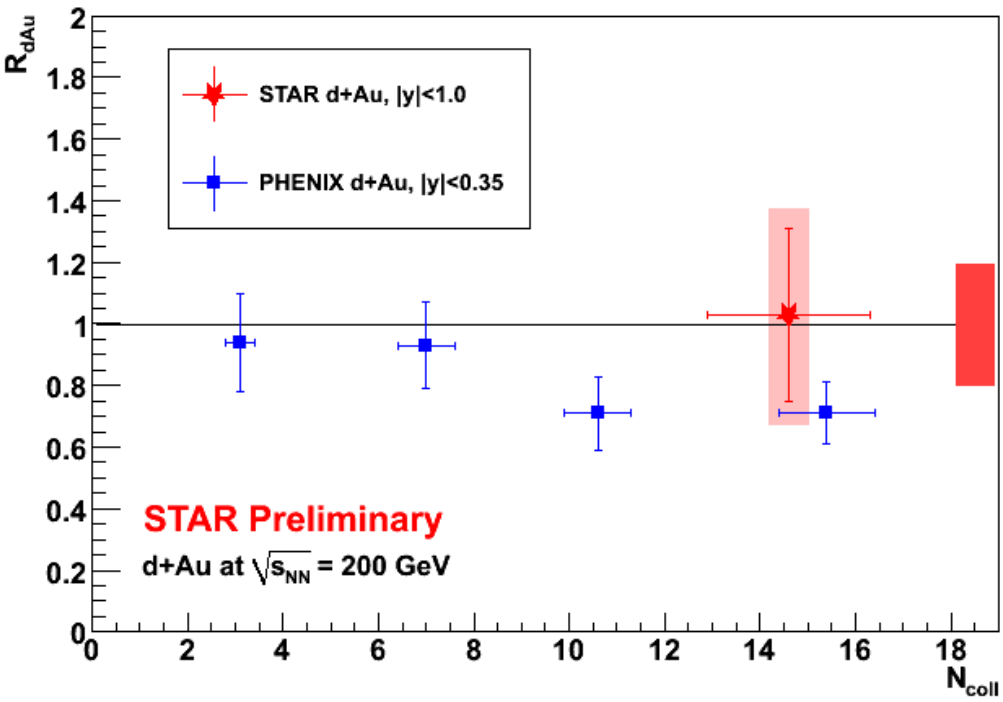

Figure 7.13: The nuclear modification factor $R_{d+{\rm Au}}^{\rm J/\Psi}$ for STAR (red) and PHENIX (blue) versus the number of binary collisions N_{coll}.

The $R_{d+{\rm Au}}^{\rm J/\Psi}$ value calculated from STAR data is

$$R_{dA}^{\rm J/\Psi} = 1.03 \pm 0.28({\rm stat.}) \pm 0.36({\rm syst.}) \tag{7.5}$$

While the uncertainties on the nuclear modification factor are significant, this value is

consistent with the PHENIX data. It is important to note that the PHENIX data has a rapidity coverage of $|y^{\mathrm{J}/\Psi}| < 0.5$, while STAR covers $|y^{\mathrm{J}/\Psi}| < 1.0$. This corresponds to a larger Bjorken x range covered by STAR, and hence a different modification of the nPDFs. As a result, these two measures may not have the same sensitivity to shadowing effects.

The reported value for $R_{dA}^{\mathrm{J}/\Psi}$ is consistent with unity, indicating no significant suppression or enhancement of J/Ψ production due to cold nuclear matter effects. The current work being done on calculating the trigger efficiency will also make data available for other centrality classes.

7.5 Systematic Uncertainties

The dominant systematic uncertainties in this analysis are listed below:

(1) *Tracking efficiency.* The uncertainty in the tracking efficiency was determined from the accuracy of the TPC response simulation and the of the TPC hits reconstruction, described in detail in [39]. The number of reconstructed hits was varied by ± 1, and this variation changed the tracking efficiency by $\pm 5\%$. Since the J/Ψs were reconstructed via their daughter electrons, the tracking efficiency must be applied quadratically. By assuming a full correlation between the daughter tracking efficiencies, the uncertainty in the J/Ψ tracking efficiency was calculated as $\sigma_{\mathrm{tracking}} = 2 \times 5\% = 10\%$.

Since the J/Ψ p+p cross section was obtained using almost identical tracking in the TPC, the uncertainty due to the tracking efficiencies mostly cancelled when calculating the nuclear modification factor $R_{d+\mathrm{Au}}^{\mathrm{J}/\Psi}$. Slight changes in the tracking algorithm and software libraries mean that the uncertainties may not have cancelled completely, but they were negligible compared to other statistical and systematic uncertainties.

(2) *Electron identification efficiency.* The electron identification efficiency, shown in Fig. 6.38, relied on the accuracy of the multiple Gaussian fit to the $\mathrm{d}E/\mathrm{d}x$ $n\sigma_e$

distribution. Uncertainty was introduced to the fitting because of the overlap of the hadronic and electron $\mathrm{d}E/\mathrm{d}x$. Since the final results have used only the TPC for electron identification, the uncertainty in the efficiency correction has been determined for TPC eID cuts only. This has been done by varying the parameters of the Gaussians fitted to the electron $n\sigma_e$ distribution by $\approx 5\%$. The single track reconstruction efficiency, which was obtained by comparing the number of reconstructed electrons to the integral of the Gaussian, showed an overall change of $\pm 6\%$ when the fitting parameters were varied. This resulted in an overall uncertainty in the J/Ψ yield of $\sigma_{e\mathrm{ID}} = 9\%$.

(3) *Background subtraction.* The background has been calculated from the arithmetic mean of the like-sign pairs, $B = (N_{++} + N_{--})$, as explained in Section 6.3.1. The uncertainty in the background calculation has been determined by observing the change in the yield obtained using different background subtraction methods, (a) the like-sign background calculated from the geometric mean of the like-sign pairs, $B = 2 \times \sqrt{N_{++} \times N_{--}}$, and (b) the background determined from a 3$^{\mathrm{rd}}$ order polynomial fit to the data outside of the J/Ψ mass window. An uncertainty in the yield of $\sigma_{\mathrm{BG}} = 7\%$ was obtained.

(4) *Yield calculation.* The comparison of the embedding lineshape and the lineshape from the Crystal Ball function showed a discrepancy in the uncorrected yield. While the embedding lineshape showed almost no low-mass tail in the J/Ψ peak, the Crystal Ball function indicated a significant low-mass contribution to the yield. The difference between the yields obtained from both lineshapes is taken as an uncertainty. This has led to a systematic uncertainty in the J/Ψ yield of $\sigma_{\mathrm{yield}} = 33\%$.

The uncertainties listed above are uncorrelated, and the total systematic uncertainty is

$$\sigma_{\mathrm{J/\Psi}} = \sqrt{\sigma_{e\mathrm{ID}}^2 + \sigma_{\mathrm{BG}}^2 + \sigma_{\mathrm{yield}}^2} \tag{7.6}$$

$$= 35\%. \tag{7.7}$$

The resulting absolute systematic uncertainty is given as $\sigma_{\mathrm{J}/\Psi} \cdot R^{\mathrm{J}/\Psi}_{d+\mathrm{Au}} = 0.36$.

(5) *Normalization uncertainty.* The nuclear modification factor was calculated by normalizing the invariant yield in $d+$ Au collisions to the yield in p+p collisions scaled by the mean number of binary collisions in 0%–20% central $d+$ Au collisions. The number of binary collisions is $\langle N_{\mathrm{coll}} \rangle = 14.6 \pm 1.7$, and the J/$\Psi$ cross section in p+p collisions was reported as [83]

$$B\frac{\mathrm{d}\sigma}{\mathrm{d}y} = 57 \pm 10\ (\mathrm{stat}) \pm 9\ (\mathrm{syst})\ \mathrm{nb} \tag{7.8}$$

To obtain an invariant yield, this number was divided by the inelastic J/Ψ cross section $\sigma_{\mathrm{inel}} = 42 \pm 3$ mb. The statistical uncertainty in the J/Ψ p+p cross section of $10/57 = 18\%$ contributed to the statistical uncertainty in $R^{\mathrm{J}/\Psi}_{dA}$ (reflected in Fig. 7.13). The systematic uncertainty in the cross section of $9/57 = 16\%$, as well as the uncertainty in the inelastic cross section of $3/42 = 7\%$, and the uncertainty in $\langle N_{\mathrm{coll}} \rangle$ of $1.7/14.6 = 12\%$, were summed quadratically to obtain the overall normalization uncertainty on $R^{\mathrm{J}/\Psi}_{dA}$, which is $\sigma_{\mathrm{norm}} = 21\%$.

Th normalization uncertainty is considered separately to the systematic uncertainty, $\sigma_{\mathrm{J}/\Psi}$. While $\sigma_{\mathrm{J}/\Psi}$ is indicated as the shaded box around the STAR data point, σ_{norm} is indicated by the red bar on the right vertical axis in Fig. 7.13.

Within these uncertainties, the STAR measure for the nuclear modification factor cannot precisely constrain the cold nuclear matter effects on J/Ψ production. However, the data indicates that there is no significant suppression or enhancement. Future analysis of mid-central and peripheral $d+$ Au events will improve our understanding of cold nuclear matter effects on J/Ψ production.

Chapter 8

Conclusion

The production of J/Ψ has been studied via the dielectron decay channel in $d+$Au collisions at $\sqrt{s_{NN}} = 200$ GeV in the STAR detector at RHIC. This analysis has measured the J/Ψ yield in the kinematic region $|y^{\mathrm{J}/\Psi}| < 1$ and ${p_T}^{\mathrm{J}/\Psi} < 5$ GeV/c, with daughter electrons required to have $|\eta^e| < 1$ and ${p_T}^e > 1$ GeV/c. The yields obtained from 0%–20% central collisions have been compared to the J/Ψ yield obtained from p+p collisions at STAR, and the nuclear modification factor of J/Ψ in $d+$Au collisions has been obtained in this centrality range. This is the first J/Ψ measurement in d+Au collisions obtained using the STAR detector, and we find that the nuclear modification factor for 0%–20% central collisions is $R_{dA}^{\mathrm{J}/\Psi} = 1.03 \pm 0.28(\mathrm{stat.}) \pm 0.36(\mathrm{syst.})$.

The nuclear modification factor of J/Ψ in $d+$Au collisions was found to be consistent with unity. This indicates that there is no significant suppression or enhancement of the J/Ψ yield due to the presence of nuclear matter as compared to p+p collisions. Within errors, the results are consistent with PHENIX data.

It is important to note that this is a work in progress. The ongoing analysis of the centrality dependence of J/Ψ production in $d+$Au collisions will provide a measure of the nuclear modification factor for different values of N_{coll}, which will improve the understanding of cold nuclear matter effects in heavy ion collisions.

Bibliography

[1] G. Dissertori, I. Knowles, and M. Schmelling, Quantum Chromodynamics - High Energy Experiments and Theory, Oxford Universidy Press, 2003.

[2] J. F. Donoghue, E. Golowich, B. R. Holstein, Dynamics of the Standard Model, Cambridge University Press (1994)

[3] D. H. Perkins, Introduction to High Energy Physics, Cam. Uni. Press 2nd Ed (1982)

[4] S. Bethke, J.Phys. G26, R27 (2000)

[5] D. J. Gross, Twenty Five Years of Asymptotic Freedom, Nucl.Phys.Proc.Suppl. 74 426 (1999)

[6] G. Sterman et. al., Handbook of perturbative QCD, Rev. Mod. Phys. 67, 157 (1995)

[7] P. Petreczkya, QCD Thermodynamics on lattice, Nucl. Phys. B140, 78 (2004)

[8] J. B. Kogout, The lattice gauge theory approach to quantum chromodynamics, Rev. Mod. Phys. 55, 775 (1983)

[9] C. Alt, et. al. (NA49 Collaboration), Pion and kaon production in central Pb+Pb collisions at 20A and 30A GeV: Evidence for the onset of deconfinement, Phys. Rev. C 77, 024903 (2008)

[10] T. Matsui and H. Satz, Phys Lett. B 178, 416 (1986)

[11] J. C. Collins, M. Perry, Phys. Rev. Lett, 34, 1353 (1975)

[12] H. Bohr, H. B. Nielson, Hadron production from a boiling quark soup A thermodynamical quark model predicting particle ratios in hadronic collisions, Nucl. Phys. B128, 275 (1977)

[13] L. McLerran, The physics of the quark-gluon plasma, Rev. Mod. Phys. 58, 1021 (1986)

[14] W. A. Zacj, The Fluid Nature of Quark-Gluon Plasma, arXiv:0802.3552v1 [nucl-ex] (2008)

[15] E. Kolb and M.S. Turner, The Early Universe, Addison-Wesley, RedwoodCity (1990)

[16] Z. Fodor and S.D. Katz, JHEP0404, 050 (2004)

[17] R.V. Gavai and S. Gupta, Phys. Rev. D71, 114014 (2005)

[18] C. Schmidt, arXiv:0210037v1 [nucl-ex]

[19] R. Casalbuoni, QCD critical point: a historical perspective, arXiv:hep-ph/0610179v1 (2006)

[20] Z. Fodor and S.D. Katz, Critical point of QCD at finite T and mu, lattice results for physical quark masses, arXiv:hep-lat/0402006v1 (2004)

[21] R. V. Gavai and S. Gupta, On the critical end point of QCD, Phys. Rev. D 71, 114014 (2005)

[22] B. Mohanty, QCD Phase Diagram: Phase Transition, Critical Point and Fluctuations, arXiv:0907.4476v3 [nucl-ex] (2009)

[23] W. Florkowski, W. Broniowski and M. Michalec, Thermal analysis of particle ratios and p_T spectra at RHIC, arXiv:nucl-th/0106009v2 (2001)

[24] J. Cleymans, Chemical equilibrium from SIS to RHIC, J. Phys. G: Nucl. Part. Phys. 28, 1575 (2002)

[25] S. Hands, The Phase Diagram of QCD, arXiv:physics/0105022v1 [physics.ed-ph] (2001)

[26] J. Adams, et. al. (PHENIX Collaboration), Multistrange Baryon Production in Au-Au Collisions at $\sqrt{s_{NN}} = 130$ GeV, Phys. Rev. Lett. 92, 182301 (2004)

[27] J. Adams et al. (STAR Collaboration), Phys. Rev. Lett. 92, 182301 (2004)

[28] A. R. Timmins (STAR Collaboration), Strange Particle Production at RHIC, arXiv:0810.0017v1 [nucl-ex] (2008)

[29] S. Soff, Strangeness Enhancement in Heavy Ion Collisions - Evidence for Quark-Gluon-Matter ?, Phys. Lett. B471, 89 (1999)

[30] D. d'Enterria, arXiv:0902.2011v2 [nucl-ex]

[31] M. Gyulassy, X. Wang, Nucl. Phys. B420, 583 (1994)

[32] C. Alder et al. (STAR Collaboration) Phys. Rev. Lett. 90, 082302 (2003)

[33] K. Adcox et al. (PHENIX Collaboration) Phys. Rev. Lett. 88, 022301 (2002)

[34] C. Amsler et al. (Particle Data Group), Phys. Lett. B667, 1 (2008)

[35] L. Yan, P. Zhuang and N. Xu, J/psi Production in Quark-Gluon Plasma. Lawrence Berkeley National Laboratory. LBNL Paper LBNL-62050 (2006) Retrieved from: http://www.escholarship.org/uc/item/3v41f1w3

[36] J. D. Bjorken, Highly relativistic nucleus-nucleus collisions: The central rapidity region, Phys. Rev. D 27, 140 (1983)

[37] F. Wang (STAR Collaboration), Distributions of charged hadrons associated with high pT particles, J. Phys.: Conference Series 27, 32 (2005)

[38] S. A. Bass, M. Gyulassy, H. Stöcker and W. Greiner, Signatures of quark-gluon plasma formation in high energy heavy-ion collisions: a critical review, J. Phys. G: Nucl. Part. Phys. 25, R1 (1999)

[39] M. de la Barca Sánchez, PhD thesis (STAR Collaboration), Yale University (2001) http://drupal.star.bnl.gov/STAR/files/startheses/2001/calderon_manuel.pdf

[40] M. L. Miller, PhD thesis (STAR Collaboration), Yale University, 2004 http://drupal.star.bnl.gov/STAR/files/startheses/2003/miller_michael.pdf

[41] D. Kharzeev, M. Nardi, Hadron production in nuclear collisions at RHIC and high-density QCD, Physics Letters B 507, 121 (2001)

[42] B. Back, et. al. (PHOBOS Collaboration), Centrality dependence of charged particle multiplicity at midrapidity in Au+Au collisions at sNN=130GeV, Phys. Rev. C 65, 031901 (2002)

[43] R. J. Glauber, in Lectures in Theoretical Physics, edited by W. E. Brittin and L. G. Dunham (Interscience Publisher's Inc., New York, 1959), Vol. 1, p. 315.

[44] R. D. Woods, D. S. Saxon, Diffuse Surface Optical Model for Nucleon-Nuclei Scattering, Phys. Rev. 95, 577 (1954)

[45] P. Filip, Elliptic Flow in Central Collisions of Deformed Nuclei, Phys. Atom. Nucl. 71, 1609, arXiv:0712.0088v1 [nucl-th] (2008)

[46] R. L. Ray and M. S. Daugherity, Applicability of Monte Carlo Glauber models to relativistic heavy-ion collision data, J. Phys. G: Nucl. Part. Phys. 35, 12510 (2008)

[47] A. Timmins, PhD thesis (STAR Collaboration), University of Birmingham, 2008. http://drupal.star.bnl.gov/STAR/files/AntsThesis.pdf

[48] M. C. Abreu et al. (NA38 Collaboration), Phys. Lett. B449, 128 (1999)

[49] M. C. Abreu et al. (NA50 Collaboration), Phys. Lett. B410, 327 (1997)

[50] R. Arnaldi et al. (NA60 Collaboration), Phys. Rev. Lett. 99, 132302 (2007)

[51] B. Alessandro et al. (NA50 Collaboration), Eur. Phys. J. C33, 31 (2004).

[52] N. Armesto, A. Capella, E.G. Ferreiro, J/ suppression at SPS and RHIC in the comovers approach, Phys. Rev. C59, 395, arXiv:nucl-th/0104004v1 (1999)

[53] L. Grandchamp, R. Rapp, Charmonium Suppression and Regeneration from SPS to RHIC, Nucl.Phys. A709 415, arXiv:hep-ph/0205305v1 (2002)

[54] A. Capella, et. al., Charmonium dissociation and recombination at RHIC and LHC, Eur. Phys. J. C58, 437, arXiv:0712.4331v1 [hep-ph] (2008)

[55] E. G. Ferreiro, Charmonium Dissociation and Recombination: Cold Effects, arXiv:0805.2753v1 [hep-ph] (2008)

[56] D. Prorok, L. Turko and D. Blaschke, Charmonium suppression at RHIC and SPS: a hadronic baseline, arXiv:0901.0166v2 [hep-ph] (2009)

[57] A. Adare, et al. (PHENIX Collaboration), Phys. Rev. C77, 024912 (2008)

[58] A. Adare et. al. (PHENIX Collaboration), Phys. Rev. Lett. 98, 232301 (2007)

[59] B. Alessandro et al. (NA50 Collaboration), Eur. Phys. J. C39, 335 (2005) arXiv:hep-ex/0412036

[60] A. Adare et. al. (PHENIX Collaboration), Phys. Rev. Lett. 101, 122301 (2008)

[61] F. Arleo, V. Tram, arXiv:hep-ph/0612043v1

[62] R. Vogt, (2004), Phys.Rev. C71, 054902 (2005)

[63] Z. Kang and J. Qiu, J. Phys. G34, S60 (2007)

[64] J.J. Aubert et al., Nucl. Phys. B 293, 740 (1987);

[65] V. Tram, F. Arleo, Eur. Phys. J. C61, 847 (2009)

[66] S. Forte, Structure Functions and Parton Distributions, Nucl. Phys. A 755, 100c (2005)

[67] K.J. Eskola, H. Puakkunen, C.A. Salgado, J. High Energy Phys. 0807, 102 (2008)

[68] F. Prino, et. al. (NA50 Collaboration), Charged particle multiplicity in Pb-Pb collisions from the NA50 experiment, J. Phys.: Conference Series 5, 86 (2005)

[69] P. Braun-Munzinger, D. Magestro, K. Redlich, and J. Stachel, Phys. Lett. B518, 41 (2002)

[70] J. Adams et al. (STAR Collaboration), Nucl. Phys. A757, 102 (2005)

[71] A. Baran, W. Broniowski, and W. Florkowski, Acta Phys. Pol. B35, 779 (2004)

[72] J. Cleymans, H. Oeschler, K. Redlich, S. Wheaton, Phys. Rev. C73, 034905 (2006)

[73] K. Redlich, Z. Phys. C 27, 633 (1985)

[74] W.B. Christie (STAR Collaboration) Overview and Status of the STAR Detector at RHIC (1999)

[75] M. Arneodo, Phys. Rep. 240, 301 (1994).

[76] G. Van Buren, et. al., Correcting for Distortions due to Ionization in the STAR TPC, arXiv:physics/0512157v1 (2005)

[77] A. Lebedev, Nuclear Instruments and Methods in Physics Research Sec. A, 478, 163 (2002)

[78] R. Reed, et. al., CHEP (2009)

[79] C.R. Rao, Sankhya A26, 329 (1964).

[80] J. Abelea et. al., Nuclear Instruments and Methods in Physics Research Sec. A, 499, 692 (2003)

[81] http://drupal.star.bnl.gov/STAR/comp/simu/event-generators/pythia

[82] J. E. Gaiser, Ph.D. Thesis, SLAC-R-255 (1982).

[83] M. Cosentino (STAR Collaboration), J/Ψ production in pp collisions at $\sqrt{s_{NN}}$ = 200 GeV in the STAR experiment, arXiv:0806.0347 [nucl-ex] (2008)